Interfacial Engineering in All Solid-Sate Lithium Ion Batteries

Carolina Vinado

A dissertation
submitted in partial fulfillment of the
requirements for the degree of

Doctor of Philosophy

University of Washington

2019

Reading Committee:

Jihui Yang, Chair
Lucien Brush
Guozhong Cao

Program Authorized to Offer Degree:

Materials Science and Engineering

University of Washington

Abstract

Interfacial Engineering in All Solid-State Lithium Ion Batteries

Carolina Vinado

Chair of the Supervisory Committee
Jihui Yang
Materials Science and Engineering

All Solid-state Batteries (ASSBs), enabled by solid electrolytes (SEs) possessing lithium ion conductivities greater than those of the liquid electrolytes at room temperature, have the potential of achieving higher energy and power densities than the conventional liquid electrolyte-based battery systems by the integration of lithium metal anode. In addition, SEs are non-flammable which improves the safety and abuse tolerances of ASSBs. ASSBs, however, face challenges that include interfacial resistance towards the cathode and lithium metal anode, compatibility with high voltage cathode, chemical and mechanical stability against lithium dendrite growth, among others. This thesis focuses on the understanding, design, and optimization of the interface between the cathode and the SE in two ASSB systems.

Thio-LISICON $Li_{10}GeP_2S_{12}$ equivalent $Li_{10}SnP_2S_{12}$ (LSPS) is comparable in ionic conductivity yet at a lower cost as an electrolyte for ASSBs. ASSBs with LSPS SE, lithium-indium alloy anode, and $LiCoO_2$ (LCO) cathode were successfully fabricated and their electrochemical performance at 60 °C was examined. Atomic layer deposition (ALD) of Li_3NbO_4 on LCO was applied to improve the interfacial stability. The Li_3NbO_4 coating significantly improves the cycle stability of the ASSB, which retains about 85% of the initial capacity after 70 cycles at a current density of 0.13 mA/cm^2, while the ASSB with uncoated LCO retains ~ 60% of the initial capacity after 70 cycles.

Electrochemical impedance spectroscopy (EIS) tests indicate a rapid growth of charge transfer resistance upon cycling for the cell with the uncoated LCO, primarily due to the surface instability and build-up of a space charge layer between LSPS and LCO. However, the ASSBs with Li_3NbO_4 coated LCO show a more stable interface with a negligible impedance increase upon cycling, attributable to the 'buffering' and 'passivating' roles of the Li_3NbO_4 coating. The interfacial microstructure was analyzed to elucidate the underlying reasons for the impedance increase and

the pivotal role of the Li_3NbO_4 coating. Our study indicates that surface coating significantly improves the cycle stability of the ASSBs with LSPS as the electrolyte mostly due to an improvement of the charge transfer mechanism. The coating reduced the interphase thickness and interfacial resistance R_{sei} to about a third of the uncoated one after 10 cycles.

Using this knowledge in ASSBs, the previously unstudied Li_2MCl_4 (M=V, Cr, Fe, Mn, Co) were tested as an option for thick electrode/power batteries due to their high ionic conductivity (1.2×10^{-5} S/cm for Li_2FeCl_4 (LFC) vs. 5.0×10^{-5} S/cm for $LiFePO_4$ at 25°C[1]), similar theoretical capacity (165 mAh/g for 1.2 Li^+ out of Li_2FeCl_4 vs. 170 mAh/g for 1 Li^+ from $LiFePO_4$[2]), and higher working voltage (3.7 V for LFC vs. 3.4 V for $LiFePO_4$[1]), and higher working voltage (3.7 V for LFC vs. 3.4 V for $LiFePO_4$). These cathode materials were successfully synthesized by solid state reactions, as well as ball milling, using LiCl and MCl_2 as the precursors. The crystal structure was determined by x-ray diffraction and confirmed with Rietveld refinements. Dissolution experiments were performed to find a suitable liquid electrolyte for these cathode materials, but the use of solid electrolytes seems necessary. Polymer electrolytes are similarly shown to have adverse reactions with the cathode material, making the use of ceramic solid electrolytes necessary.

When using LSPS SE, LFC exhibited a reversible discharge capacity of 200-250 mAh/g, corresponding to 1.25-1.75 Li^+ ions per formula unit, but it seems to correspond to a conversion reaction. Further experiments were performed to determine the reaction mechanisms. A judicious SE selection became imperative to establish the electrochemical properties of LFC and the rest of the Li_2MCl_4 family of materials.

To that end, a SE in the halide family of electrolytes was synthesized and studied. The ionic conductivity of the recently discovered halide solid electrolyte Li_3YCl_6 (LYC) was studied as a function of its crystal structure. When the sample was quenched from 450 °C it exhibits a hexagonal phase, as opposed to the orthorhombic phase it presents when quenched from 350 °C. The high temperature hexagonal phase has an ionic conductivity of 0.05 mS/cm, while that for the lower temperature orthorhombic phase is twice as high at 0.10 mS/cm. Conversely, ball milling the sample, as reported by Asano et al. gives a room temperature ionic conductivity of 0.46 mS/cm, which is highly encouraging for the scalability of this cheap, soft, relatively safe SE.

LFC is finally explored as a cathode material for ASSBs using LYC SE. This previously unstudied cathode material was cycled at a C/10 rate, or 0.195 mA/cm^2 at 25 °C, obtaining a discharge capacity of about 118 mAh/g, and it reached 80% discharge capacity at the 180th cycle. LFC is able to deliver 112 mAh/g, 106 mAh/g, 81 mAh/g, 40 mAh/g of the initial specific discharge capacity when tested at a rate of C/5, C/3, 1C, and 2C, respectively. EIS studies showed that the biggest contributor to impedance was the solid electrolyte layer, followed by the interface between the cathode and the solid electrolyte. The interphase was confirmed through computational studies to be mainly composed of LiCl, $FeCl_2$ and YCl_3, which are either ionically (LiCl), or electronically conductive ($FeCl_2$), and therefore, not detrimental to the impedance of the cell.

TABLE OF CONTENTS

LIST OF FIGURES

LIST OF TABLES

ACKNOWLEDGEMENTS

I’d like to thank Dr. Yang for his directions, suggestions, and patience. His insights and viewpoints brought enormous value to this project. I’d like to acknowledge all those in my lab who have contributed in various ways to the progress of these projects, most notably Ms. Li and Dr. Jiong Yang, as well as Dr. Wang. Further recognition should go to the scientists at PNNL that contributed to this investigation, Dr. He, Mr. Xu, and Dr. Chongmin Wang. Mr. Bo, at Shanghai University, for his assistance with computational inquiries. I’d also like to thank all of those in the GM R&D department who contributed with ideas, technical expertise and training to this project, among them Dr. Salvador, Dr. Xiao, Dr. Cai, Dr. Li, Dr. Thompson, and Mr. Irish.

DEDICATION

This work is dedicated to all those who offered nothing but unyielding support, love, and encouragement. Their unparalleled strength and confidence are the foundation of this enterprise:

My parents, Daniel Vinado and Mireya Escalante, always a phone call away.

My siblings, Gabriel and Laura, the best rally troops.

My partner and emf, Gentiana Coman.

My coaches and teammates at DLF, their ability to motivate and bring out the best in people is uncanny.

To Asimov: the definition of happiness, anxiety, and unconditional love.

Chapter 1. Introduction

1.1 MOTIVATION

With the increasing demands for energy and energy storage device/systems, there is a tremendous effort towards powering devices and machines with electricity from renewable sources. This effort is now largely due to society's understanding of the scientific community's consensus on the environmental downsides of using fossil fuels and biomass for energy; most notably climate changes and pollution, as well as the dependence on foreign oil. Renewable sources, such as solar radiation, wind, waves, geothermal, and nuclear, are limited in time and location, requiring storage. However, the major advances we've seen in the field of sustainable energy harvesting have not been seen in the energy storage field.[4,5] The increased harvesting from renewable resources, as shown in Figure 1-1 will require a corresponding increase in storage, which is visibly well behind, as well as ease of use for various applications thereafter.

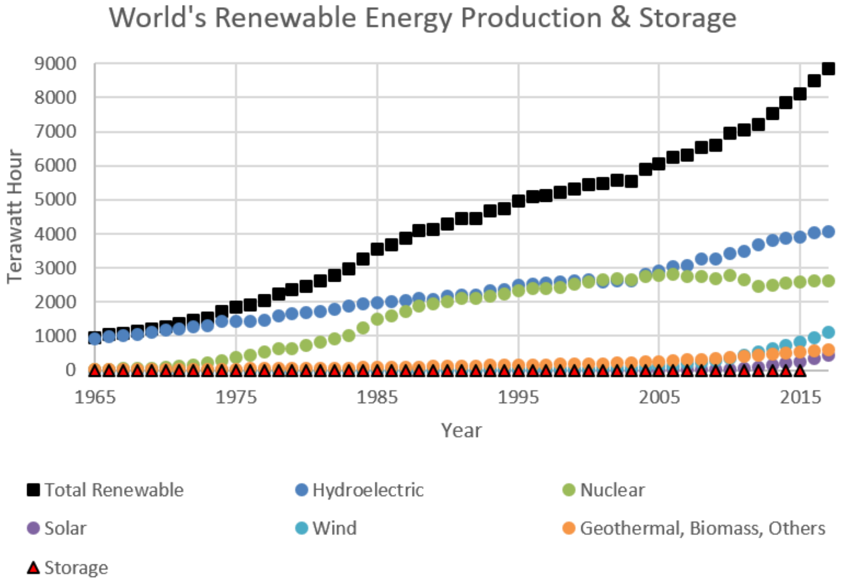

Figure 1-1. Total renewable energy production by year, along with a breakdown by source.[6]

While it is easy to think of sustainable energy harvesting and storage as problems foreign to our everyday lives, batteries are integral to society, largely in part due to the convenience of their portability. Most devices that use batteries do so because direct access to an electricity source is not suitable and other conventional energy storage devices are not as portable.[4,5] Batteries are common place, whether they are in the phones that keep us communicated and entertained in our day to day, to the battery our cars use to start, or for propulsion in hybrid or electric vehicles, to the many gadgets that are now wireless such as TV remotes, toothbrushes, power drills, lawn mowers, among others.

Approximately 25% of all personal vehicles in the world are registered in the USA, 60% of which are cars, and of the 20 million barrels of oil the US consumes a day, 45% is used for personal transportation.[7] When seen from this perspective, it is easy to grasp the monumental impact that even partially shifting to hybrid or electric vehicles will have on our economy, and our environmental footprint. In order to make a meaningful shift, however, the current battery technology for energy and power needs to take several large steps. The purpose of our research is to contribute to the advance of the energy storage field, particularly, for these power applications.

1.2 LITHIUM BATTERIES

Lithium ion batteries (LIBs) are widely commercialized to power portable devices. Due to their high energy density, it is the most attractive option for hybrid electric vehicles (HEV), electric vehicles (EV), and other power portable applications.[8] Given the variations in usage, and sometimes lack of standard use, we are going to briefly give some useful definitions.

1.2.1 *Working Principle of Batteries*

A battery is a group of electrochemical cells that convert and store electrical energy into chemical energy. During the charging of a battery, they are considered to be electrolytic cells since electric energy is converted into chemical energy; whereas for discharge, they are referred to as galvanic given that they are converting chemical energy into electric energy. Primary batteries are those in which the chemical processes are not reversible. Once discharged, they can't be charged again for re-use. Opposite to these are the secondary batteries, in which the reactions can be driven in reverse, allowing for multiple charge/discharge cycles.

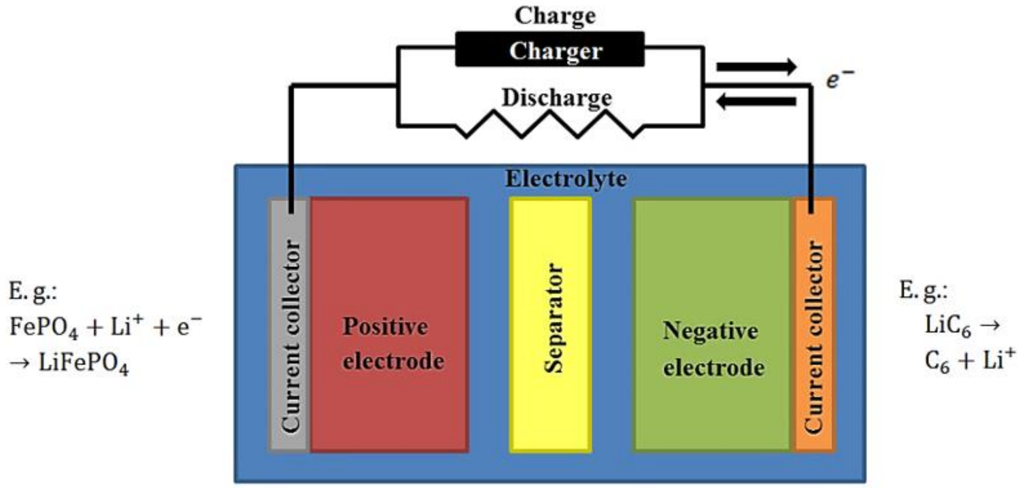

Figure 1-2. Diagram of an electrochemical cell with half reaction examples and all the chemically inactive components.

The basic structure of an electrochemical cell is shown in Figure 1-2. Two electrodes, one negative, one positive, are separated by an ionically conductive and electrically insulating electrolyte. The negative electrode is designated as being the one in which an oxidation or anodic reaction occurs during discharge, and reversed during charge, meaning a reduction or cathodic reaction takes place.[9]

In the battery research community, an active material refers to the electrochemically active material inside a cell; for example, the metal oxide in the cathodic electrode and the graphite or silicon in the anodic electrode are active materials. All other components in a battery cell, such as the binder, casing, separator, are called inactive materials.

1.2.2 *Charge and Discharge*

In the battery research community, the discharge process is taken as the nominal standard process; hence, the positive electrode during discharge (the one undergoing a cathodic or reduction reaction) is consistently referred to as the cathode, even though it undergoes an anodic reaction during charge. Each electrode undergoes a half-cell reaction, which can be added to give the overall reaction of the cell, also shown in Figure 1-2. These half reactions on the electrodes produce a flow of electrons in the external circuit, balanced by the migration of ions through the electrolyte and into the other electrode.[10] In a full electrochemical cell, containing an anode and a cathode, reactions occur on both electrodes. Half cells are commonly used for research to isolate the electrochemical properties of the electrode. In a half cell only one electrode undergoes electrochemical reactions, while the other one is used as a reference electrode, allowing the study of the basic properties of each electrode individually.[9]

1.2.3 *Free Energy*

When converting chemical energy to electrical energy, the maximum energy that can be delivered depends on the change in free energy ΔG of the electrochemical couple. The change in free energy, ΔG, is proportional to Faraday’s constant, the number of electrons involved, and the standard potential.

1.2.4 *Potential*

The two electrodes have different electric potentials, and when placed into the same cell, there exists a potential difference, also called electromotive force, open circuit voltage (OCV), or emf, and it is measured in volts (V). The OCV is not to be confused with the nominal, or operational, voltage. The operational voltage is the one at which the cell operates during discharge, and it is lower than the nominal voltage due to the current induced polarization, which is the algebraic sum of the overvoltage and ohmic voltage drop.[11] This overvoltage and ohmic voltage drop are caused by internal ionic or electrical resistance, electrical double layers at the particle's interface, rate of reaction, mass transfer and diffusion rate, among others. The influence of the current density on various overpotential causes are summarized in Figure 1-3. Therefore, if the charge reaction is the same as the discharge reaction, the charge and discharge voltages should, in theory, be the same. Often times however, this polarization will shift the charge voltage up, while reducing the discharge voltage, effectively lowering the operational voltage.[12] The current in a battery is closely related to the rate of electrochemical reactions. Low currents are limited by activation losses, while high currents are limited by the mass transfer.

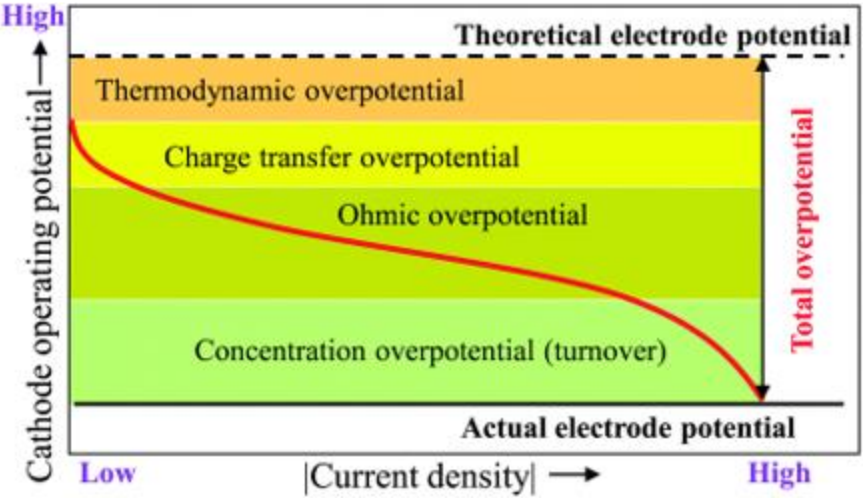

Figure 1-3. Influence of current density on various overpotentials.[13]

1.2.5 *Capacity*

Capacity, in general, is the term used to convey how much electricity could be released from a charged battery in a certain amount of time. Technically, the unit to measure the amount of electricity is the Coulomb (C); however, in practice a product of the intensity and duration of said current is used, and usually expressed in ampere-hour (Ah), or mAh for smaller batteries.[11] Several terms are used to describe the expected capacity value under particular conditions:

Theoretical capacity is the amount of charge expected from a fully charged cathode after it is completely discharged, and it is, therefore, independent of the discharge rate or other conditions and solely a function of the amount of active material available. It is called theoretical due to the practical difficulties of extracting all the charge from any given active material.

Effective, real, or practical, capacity is the amount of electricity released by a fully charged battery during full discharge under given conditions such as discharge current rate, voltage window, temperature, etc.

Theoretical gravimetric capacity is the ratio of the electricity theoretically available in the active material, to the mass of said active material; it is normally expressed in the units of mAh/g. Given that it doesn’t consider the mass of the inactive material, the real gravimetric capacity is sometimes well below the theoretical value of the cell used.

We must pay special attention as to what capacity is being reported when reading scientific papers, as these terms are used interchangeably, often to hide poor practical gravimetric capacity, or could be an indication of extremely low active material content in the electrode.

The discharge current of a battery, also called the C-rate, refers to the current necessary to fully charge or discharge a battery in a certain amount of time, generally given in hours. For example, a rate of C/5 corresponds to the current required to fully discharge (or charge) a battery in five hours.[10] Discharging and charging at extremely low current, while unpractical for most applications, allows the extraction of near theoretical capacities, while reducing polarization and overpotential issues.

A battery is considered to be out of service, or at the end of its lifetime, when its capacity irreversibly drops to below 80% of the nominal value, regardless of the reason. Common aging processes include consumption of lithium creating a solid electrolyte interface (SEI) or passivating layer, modification or loss of the active material's crystalline structure, degradation of the electrolyte, delamination of the active material from the current collector, secondary reactions, among many others.

1.3 APPLICATIONS: ENERGY, POWER, STORAGE

Generally speaking, most batteries fall into storage, energy, or power applications. When talking about batteries intended for energy applications, their parameters are given in energy terms. Consequently, energy density is the amount of energy in watts-hour (Wh) stored per unit weight (when referring to gravimetric energy density, Wh/kg), or per unit volume (when referring to volumetric energy density, Wh/m^3). These terms can also be used with respect to power batteries; gravimetric power density is given in units of W/kg, and volumetric power density in W/m^3.[10]

Using the hydraulic analogy, sketched in Figure 1-4, the main design concern of a power battery would be to dump as much water as fast as possible, so it is designed to impede water flow as little as possible, contrary to energy batteries whose main priority is to have a slow drip over extended times, so the capacity and volume is the main deign factor. Storage batteries would be the cheap and large tank of water from which water could be dumped into and out of repeatedly with little maintenance required.

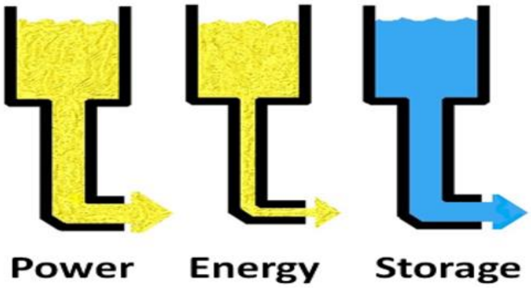

Figure 1-4. Hydraulic analogy for the needs of batteries by application.

The electrochemical kinetics of an electrode is limited by the diffusion of lithium ions in the bulk. For this reason, electrodes tend to be thicker on energy density-oriented electrodes, as opposed to the thinner power density-oriented electrodes. Power applications, therefore, necessitate high electrical and ionic conductivities, among other things.

Energy batteries are meant to deliver small currents over extended periods of time, such as a cell phone battery would; the electrodes are dense and reducing volume tends to be a priority. Conversely, a power battery is expected to relinquish a large amount of current in very little time, in the way a battery-operated power drill would. Electrodes for power applications tend to be less dense and have a low concentration of active material with large amounts of surface area (in both senses: small particle size, and large electrode surface area), to allow the charged species to move quickly through the battery. Storage batteries are meant to store a large amount of current until needed, and often their driving characteristic is low self-discharge rate and cost. Starter batteries, for example, are the ones used in machinery with a combustion engine to provide the engine with power until the alternator sufficiently covers the demands.[10] They have low to medium energy densities, medium to high power densities, and must be of low cost as well as withstand shallow cycles. On the other end of the spectrum, traction or on-board batteries are used for power, as well as to deliver certain range. On-board batteries in all electric vehicles are sized to ensure certain range can be achieved in one charge and the electrode materials of choice must withstand deep discharge cycles; normally, supplying large amounts of current during acceleration is not their main design constraint.[10]

1.3.1 *Advantages of Solid-State Batteries*

Most commercially available LIBs use flammable liquid electrolytes, which risks fire or explosions in the event of a failure.[4] From a safety point of view, replacing the flammable liquid electrolyte with a solid one would be desirable. Solid state batteries are batteries in which the liquid electrolyte is replaced with a thin layer of high lithium ionic conductivity solid material. Solid state batteries have several advantages over traditional batteries with liquid electrolytes; these advantages can be summarized as: resilience to abuse.

Most liquid electrolytes are flammable and quickly and/or fully charging and discharging the battery can generate heat, resulting in untapped capacities and slower rates, in order to maintain the battery within the flammability limits of the electrolyte. Liquid electrolytes also degrade with increasing temperature, reducing the life of the battery if it were to overheat often or continuously.[4] In order to keep the liquid electrolyte from igniting or degrading, a plethora of safety systems that ultimately add to the weight and cost have to be built into the battery packs, as well as narrowly controlled charge/discharge rates, limiting power applications.

Liquid electrolytes have narrow, low voltage, working windows, beyond which a passivating layer that reduces the ionic conductivity and capacity of the cell is required.[4] This loss of capacity is proportional to the surface area of the cathode material. A compromise is therefore needed between power capability, and voltage (and consequently, capacity).

Most of the Li-ion electrode materials have soluble species. Manganese containing layered or spinel cathodes have the problem of Mn dissolving into the electrolyte when deeply discharged.[14] These solvated ions travel to the anode and plate it, eventually damaging the battery.

Another example would be sulfur electrodes; preventing their tendency to dissolve into the electrolyte is subject of extensive recent research.[15]

Solid state batteries require significantly less packaging, since electrolyte leakage is not of concern, and as previously mentioned, they don’t require as intense thermal management as liquid electrolytes do. Solid electrolytes also help prevent the formation of "dendrites" on electrodes that rely on alloying mechanisms to store energy. Another advantage over the liquid counterpart would be that lithium wouldn’t be consumed on the formation of the solid electrolyte (SE) interphase layer, resulting in a loss of capacity.

Other difficulties of Li-ion batteries, particularly for electric vehicles, are the low energy and power density of most intercalation/insertion mechanisms, low charge and discharge rates and service life, and high cost.

1.4 FABRICATION AND TESTING OF SOLID-STATE BATTERIES

Half cells are typically tested in coin cells, such as the one shown in Figure 1-5. Once assembled, they have a set thickness making it challenging to assemble solid state cells with the proper amount of pressure or thickness; excessive pressure might crack or break the pellet when it is too thick, while insufficient thickness might result in loss of electrical contact if the pellet is too thin. This is not an issue for cells with liquid electrolyte, for the electrolyte fills the space, ensuring contact. Another challenge is that the crimping of the coin cells requires applying sharp large pressures, which often cracks pellets beyond that certain thickness.

Figure 1-5. Diagram of a typical coin cell.

A previous design consisted of Swagelok cells. It consisted of a stainless steel (SS) rod ½" in diameter was cut into 1.5" long pieces; threaded holes were opened in one end to insert SS screws to permit the alligator clamps with which the Land system were fit to connect. The rods, or plungers, were fit on the other end with nylon ferrules and inserted into a perfluoroalkoxy (PFA) union. A spring and a titanium spacer, one millimeter in thickness and 0.4" in diameter, are inserted into the union followed by the above electrode pellet, and the indium (or lithium) foil pressed into another titanium spacer, as also depicted in Figure 1-6. Finally, another SS rod section also fit with ferrules is inserted, creating an airtight seal. The design, while appropriate for polymeric solid electrolytes, didn't offer enough pressure to make the ASSBs with ceramic electrolytes work without prohibitively high overpotentials.

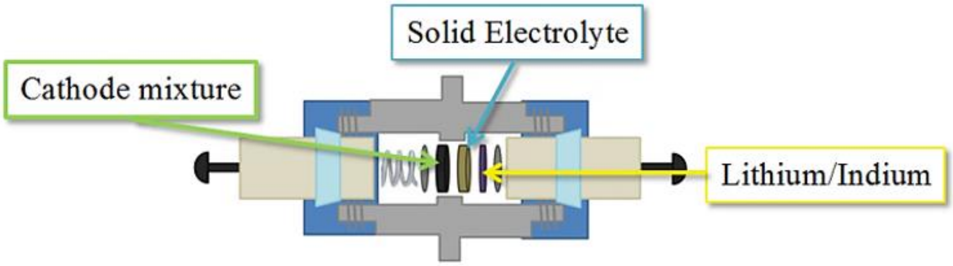

Figure 1-6. Diagram of an assembled Swagelok.

In order to ensure continued contact during cycling, ASSBs require specially designed cells. They consisted of two pieces made of a circular base with a 10 mm of diameter rod in the middle, as shown in Figure 1-7. They were milled from a single SS tube, in order to bypass possible resistance created by the junction of the base to the rod. A polyether ether ketone (PEEK) die, also 10 mm in diameter was used as a sleeve to contain the pellet. Two long screws were used to apply pressure across the pellet. The screws were kept from shorting the battery through the use of two PEEK sleeves around one of the SS bases. In order to test the batteries outside of the glovebox, mason jars were used to seal the samples. The lid was perforated, and binding posts were put through in order to be able to electrochemically test the cells. The perforations were sealed with epoxy to ensure the jars were airtight.

Figure 1-7. Photograph of an assembled cell for ASSB texting. The jar with the binding posts prevents moisture exposure, while the SS parts inside are to provide the ASSB with pressure.

Chapter 2. All Solid-State Batteries with $Li_{10}SnP_2S_{12}$ Electrolyte and $LiCoO_2$ cathodes

2.1 INTRODUCTION

2.1.1 *Thio-LISICON $Li_{10}GeP_2S_{12}$ Equivalent $Li_{10}SnP_2S_{12}$*

An eligible solid electrolyte (SE) should at minimum have an ionic conductivity comparable to that of current liquid electrolytes, e.g., 10^{-3}-10^{-2} S/cm.[4] Figure 2-1 summarizes the current ionic conductivity of some SEs, with a few organic electrolyte values for reference. The relatively recent finding of $Li_{10}GeP_2S_{12}$ (LGPS, upper right corner in Figure 2-1), with an outstanding ionic conductivity of 12 mS/cm, comparable to that of liquid electrolytes, has made the use of sulfide-based SEs an appealing option for ASSBs.[8,16] The high cost of Ge due to the scarcity of its deposits, however, largely limits the commercial use of LGPS. Creating isostructural analogues with little cost to the ionic conductivity and chemical stability, by substituting the Ge with Si, Al, or Sn, has been suggested.[17-19]

The Sn analogue $Li_{10}SnP_2S_{12}$ (LSPS) is the most promising of the group at one third the cost of the germanium parent structure.[19] Another such advantage is the fact that it is already commercially available; sold by NEI corporation as NANOMYTE® powder (SSE-10). Its synthesis process often involves ball milling of the precursors, pelletization of the powders, sealing them in a vacuumed ampoule and high temperature sintering. [18,20] The materials react into the orthorhombic phase at 613K, turn into the desired tetragonal phase at 653K and undergo a high crystal growth phase at 723K.[20] Due to the tendency of Sn^{IV} to have 6-fold coordination (SnS_6

octahedrons), rather than the desired SnS_4 tetrahedral coordination, excess Li_2S in the order of 10-20% is often required to guarantee full oxidation of the Sn and the P.[20]

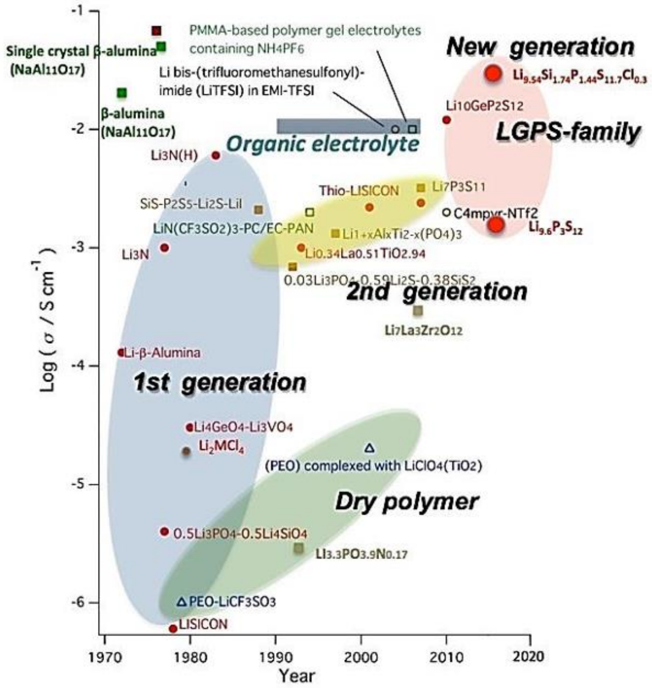

Figure 2-1. Summary of electrolyte conductivity over time.[21]

As seen in Figure 2-2, an increase of the cation size by substituting Ge in the parent structure with Sn or other larger isovalent elements has little effect in the diffusivity of Li^+, albeit Sn has a marginally lower diffusivity than Ge; furthermore, aliovalent cation substitutions also offer little change in the diffusivity of Li^+.[17] Conversely, a change in the anion to a smaller one in size, such as oxygen, is proportional to the lattice parameter and conductivity and inversely proportional to the activation energy, as seen in Table 2-1.[17] This is expected since the larger radius, paired with the lower electronegativity of S vs. O, for example, leads to larger tunnel and larger mobility of Li^+. While the decrease in anion size has a large impact on several parameters, an increase in anion size doesn't have as big of an impact. Therefore, substituting the Ge cation for another cations, or S for Se should have little impact in several properties, making the LSPS composition the best compromise in properties and cost.

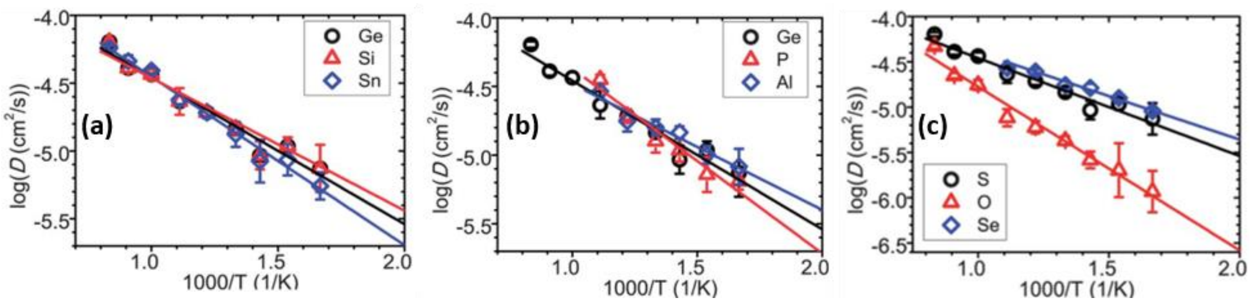

Figure 2-2. Calculated effect of (a) isovalent (Si^{4+} and Sn^{4+}), (b) aliovalent (P^{5+} and Al^{3+}) cation substitution, and (c) anion substitution on the diffusivity of Li^+ (D) in the parent LGPS structure as a function of temperature.[17]

Table 2-1. Calculated trends in the activation energy, lattice parameters, and conductivity with anion substitution in LGPS.[17]

	Volume (Å^3)	**Activation Energy (eV)**	**Conductivity (mS/cm)**
O	534	0.35	0.03
S	979	0.25	13
Se	1164	0.2	24

Furthermore, experimental studies of the ionic conductivity as a function of temperature, presented in Figure 2-3, done by Kuhn et al. determined the activation energy for ionic conductivity of Li^+ in LSPS to be of 0.25 eV with an ionic conductivity of 6 mS/cm at room temperature, consistent with the computational results previously obtained by Ong et al. and comparable to that of LGPS.[17,20] Finally, thermogravimetric analysis (TGA) testing shows LSPS is thermally stable up to about 700 °C, and no phase transition is seen up to that temperature in differential scanning calorimetry (DSC) measurements, making it stable in our desired temperature range of testing.[18] All this, along with the lack of cell level electrochemical data makes LSPS an obvious choice for ASSBs studies.

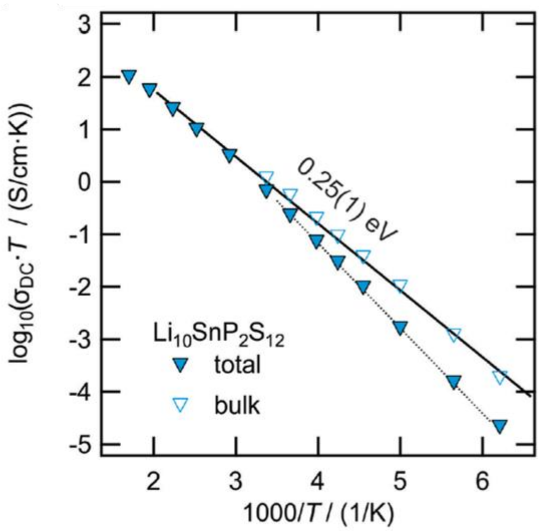

Figure 2-3. Total and bulk conductivity extracted from EIS data.[20]

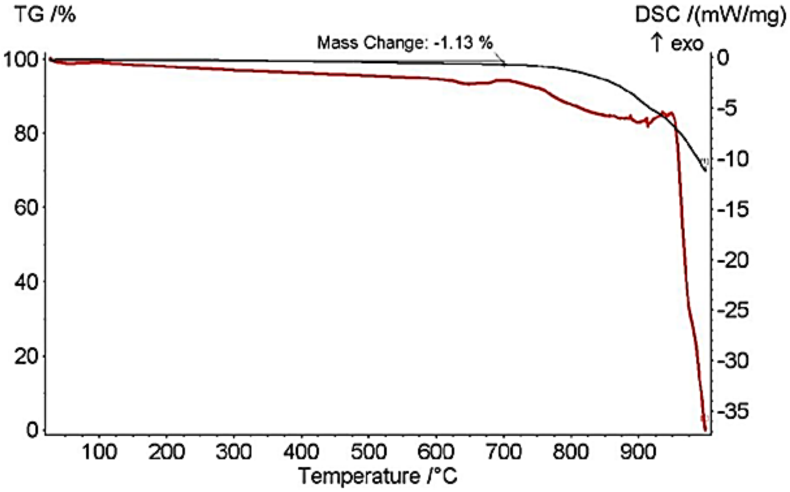

Figure 2-4. TGA (black) and DSC (red) measurements on LSPS.[18]

2.1.2 *Interfacial Impedance in ASSBs*

Currently, the main hurdle for developing successful ASSBs for EVs, however, is in minimizing the interfacial impedances between the SE and the electrodes, especially for SE/cathode interfaces, rather than improving the conductivity of SEs. Given that the interfacial impedances primarily dominate the rate capability and cycling stability of the ASSBs, the power density will remain low, regardless of the conductivity of the solid electrolyte, if it is not addressed.[8,22-24] Various mechanisms have been suggested for the cause of the rate limiting interfacial impedance, most notable of which are detrimental chemical side reactions, and formation of a space charge layer (SCL).[25]

SEs must be chemically and electrochemically stable against the electrode materials, and able to form a stable and conductive interface.[22,26-29] Based on the theoretical calculations, sulfide-based SEs show narrow electrochemical windows, such as ~ 1.8-2.3 V vs. Li^+/Li for LGPS, as seen in Figure 2-5.[30] Below said potentials, the sulfide based solid electrolytes will begin to lithiate and reduce; conversely, beyond the potential, they will readily oxidize. Zhu et al. determined the chemical stability of SEs and LCO with respect to the chemical potential of O and S, also seen in Figure 2-5. They determined that there is a significant gap between the oxide-based cathodes and sulfur based SE which grew dramatically with delithiation; this gap would oxidize LGPS and reduce LCO into phases such as highly ionically insulating cobalt sulfides.[30] Experimental results have shown that the elements will indeed react and interdiffuse as much as 50 nm into each other, producing a thick interphase layer.[30,31] This interphase not only contributes to an increase in impedance, but also a direct loss of cathode material.

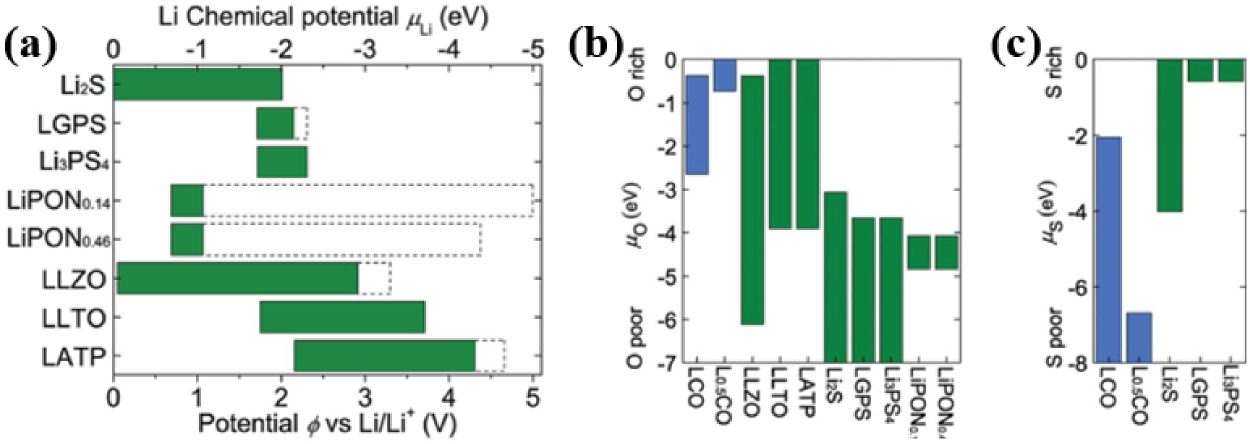

Figure 2-5. Stability window of SEs, LCO, and $L_{0.5}CO$ with respect to the chemical stability of Li (a), O (b), and S (c).[30]

In addition, due to this difference in Li^+ chemical potential a SCL is formed.[31] Oxide ions, being more electronegative than sulfide ions, attract lithium ions much more than S ions; this causes a net migration of lithium from the sulfide based SE into oxide-based cathode materials until equilibrium is reached, as illustrated in Figure 2-6.[29] This depletion is accentuated upon delithiation of the cathode, as previously mentioned. Given that the main charge carriers in sulfur-based SEs are Li^+ and not V_{Li}', this depletion layer is highly resistive.[25] Due to the electronic conduction of LCO, this SCL will be greatly developed;[29] similarly, the addition of carbon additives to the cathode mixture will greatly contribute to the development of such SCL.[32]

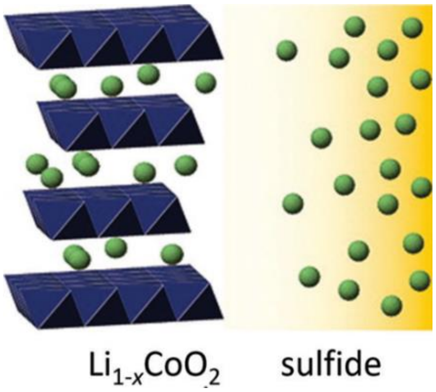

Figure 2-6. Schematic representation of the SCL.[24]

To facilitate successful ASSBs, interfacial modifications on either electrodes or the SE are necessary to mitigate the chemical diffusion and SCL, thus reducing the interfacial impedance and extending the electrochemical window beyond 4.2 V (vs. Li^+/Li).[22,26-29,33-36] Ideally, this buffer layer will have a relatively high lithium chemical potential, as well as electronically shield the SE from the oxide cathodes while allowing the free movement of Li^+. An ionically conductive oxide buffer layer would satisfy all those requirements; the chemical potential between oxides is similar, and as an electronic insulator, a much smaller SCL will develop on the SE, as illustrated in Figure 2-7.[29] A variety of lithiated oxide materials have been used for this purpose,[24,30,37] and it can be seen in Figure 2-8 that most of these materials will bridge the gap between the stability window of the SE and the LCO.

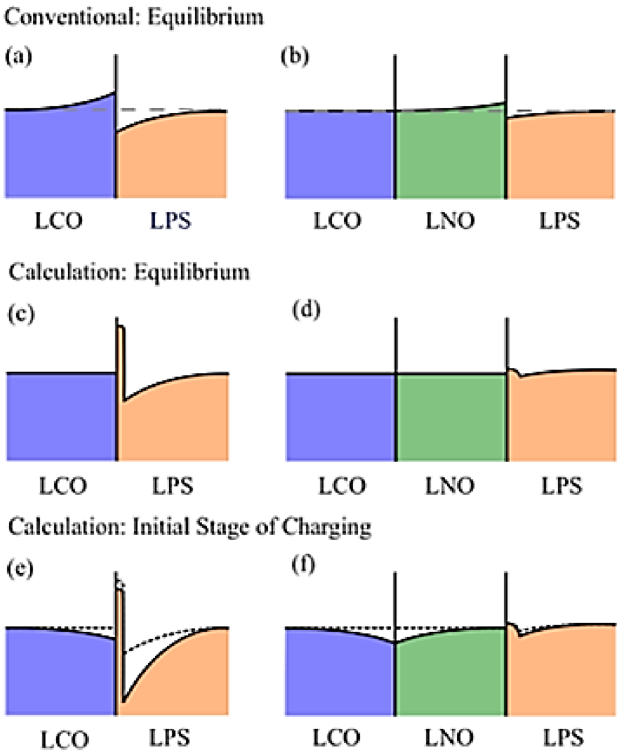

Figure 2-7. Schematic illustrations of the concentration of Li^+ at interfaces with respect to lithium chemical potential (dotted line).[31]

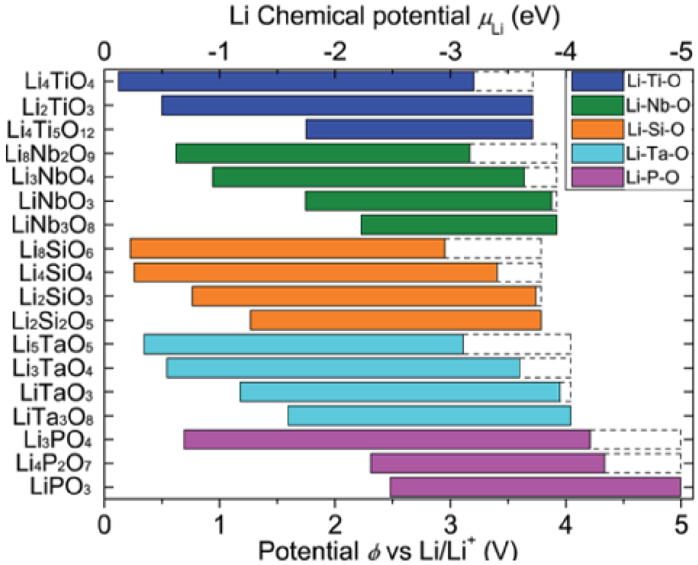

Figure 2-8. Electrochemical window of various coating materials.[30]

The coating material should not only be a good ionic conductor, but also thin and uniform. Typically, wet chemical methods such as sol-gel or spray coating, are used for surface coating; these methods, however, leave non-uniform and thick coatings, visually summarized in Figure 2-9.[32] The drawback from these coating techniques is that to guarantee full coverage a thick coating must be applied, and the thickness of the layer becomes the rate limiting process.[38] Alternatively, atomic layer deposition (ALD) boasts excellent conformity, atomic scale thickness control, and uniformity over large areas, emerging as a promising process for battery electrode coating.[26,39] The sequential and self-limiting nature of ALD allows for ultra-thin and pinhole free coatings to be applied. These sub-nanometer coating layers have the added benefit of lessened mechanical stresses due to the crystal mismatch and reduced constraints as far as the electron and lithium ion conductivities of the coating material.[32]

Figure 2-9. Coating morphology by spray coating, sol-gel and ALD processing.[32]

2.1.3 *$LiCoO_2$ to Study the Interfacial Characteristics of $Li_{10}SnP_2S_{12}$*

To evaluate the potential of LSPS as an SE and study its interfacial behavior with cathode materials, as well as to validate our ASSB processing and set up, ASSBs with LSPS SE, Li/In anode, pristine and ALD Li_3NbO_4-coated $LiCoO_2$ cathodes were fabricated. A niobium oxide compound was chosen due to its low interfacial resistance when compared to other oxide-based coatings;[31] similarly, a compound with a high lithium content was used due to their lower reduction potential.[30] The electrochemical performance and interfacial characteristics of the ASSBs using pristine and coated $LiCoO_2$ were systematically explored by galvanostatic cycling, AC electrochemical impedance spectroscopy (EIS), scanning electron microscope (SEM), transmission electron microscope (TEM), etc. The study shows that the ALD coating drastically improves the electrochemical performance of ASSBs with LSPS SE, in large part due to the improved interfacial compatibility and decreased charge transfer impedance.

2.2 METHODOLOGY

2.2.1 *Cathode Materials*

Commercial $LiCoO_2$ (LCO, 99.8%, Sigma Aldrich, USA) was used as a baseline to verify the solid-state battery processing.

ALD of ultrathin lithium niobium oxide coatings were deposited using a Savannah 100 Atomic Layer Deposition system (Cambridge Nanotech Inc., USA), with lithium tert-butoxide (LiOtBu, $(CH_3)_3COLi$, Sigma Aldrich, USA) and niobium ethoxide [$C_{10}H_{25}NbO_5$, Sigma Aldrich] as the precursors. Distilled water was used as the oxidant and argon (99.99%) as the carrier gas. The pulse, exposure, and purge times for all the precursors are 0.1 s, 10 s, and 20 s respectively in each sub-cycle. A simple visual representation of the sub cycles, which were repeated 5 times, can be seen in Figure 2-12. The heating temperature was 160 °C for both Li and Nb precursors, and 80 °C for water. The deposition temperature was around 200 °C for the $LiCoO_2$ powder samples.

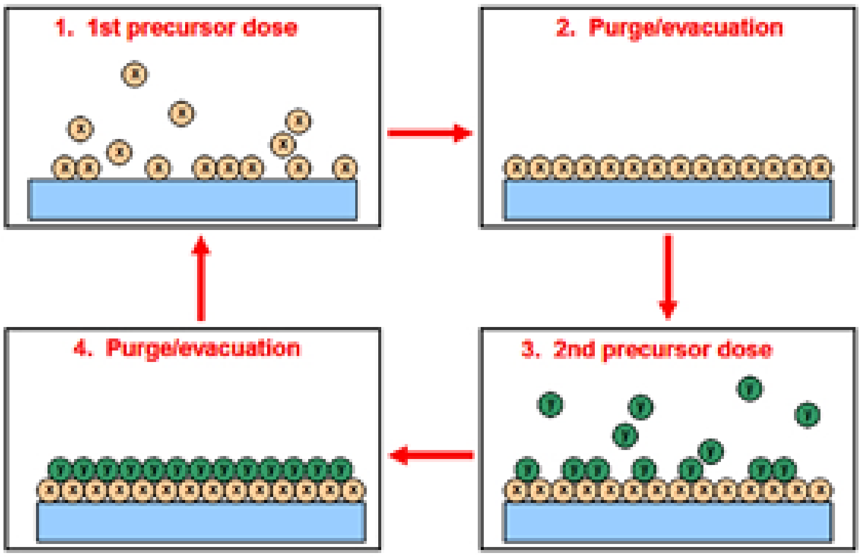

Figure 2-10. Schematic of the cycles of ALD processing.[40]

2.2.2 *Characterization*

The crystal structure of the materials was investigated through powder X-ray diffraction (XRD, Bruker D8 advance, Germany). The LSPS and LFC powders were first placed in a capillary tube and sealed with wax before exiting the glovebox. A field emission SEM equipped with an Oxford energy dispersive X-ray spectrometer (FESEM/EDS, FEI Sirion XL30, USA) was used to image the particle morphology and obtain elemental analysis and mapping. The microstructures and compositions of the cycled electrodes were analyzed by a scanning TEM equipped with a high-angle annular dark-field (HAADF) detector and an EDS at the Pacific Northwest National Laboratory (STEM/HAADF/EDS, FEI Titan 80-300kV, USA).

2.2.3 *Electrochemical Testing*

The electrochemical properties LCO/LSPS/Li-In ASSBs were investigated using the home-made all-solid-state cells. Electrode mixtures consisted of pristine LCO or Li_3NbO_4 coated LCO (c-LCO) powders, and LSPS powders (Nanomyte SSE-10, NEI Corporation, USA) in a weight ratio of 70:30. They were prepared by hand grinding in a mortar for 30 min. Two-electrode all solid-state cells were fabricated using ~ 12.7 mg of electrode mixture as the cathode, 80 mg LSPS as the separator, and Li-In foil as the anode. The working electrode and LSPS were placed in a stainless-steel die with a diameter of 10 mm and pressed together under 500 MPa for 20 min. The cathode/LSPS pellet was then dissembled from the die and placed into a die. 60 mg of In foil (0.62 V vs. Li^+/Li,[41] 99.99%, CMR-Direct, USA) and 10 mg of Li foil (99.9%, MTI Corporation, USA) were placed on the top of the SE and a pressure of 20 MPa was then applied. A schematic of the architecture of the cell can be seen in Figure 2-11.

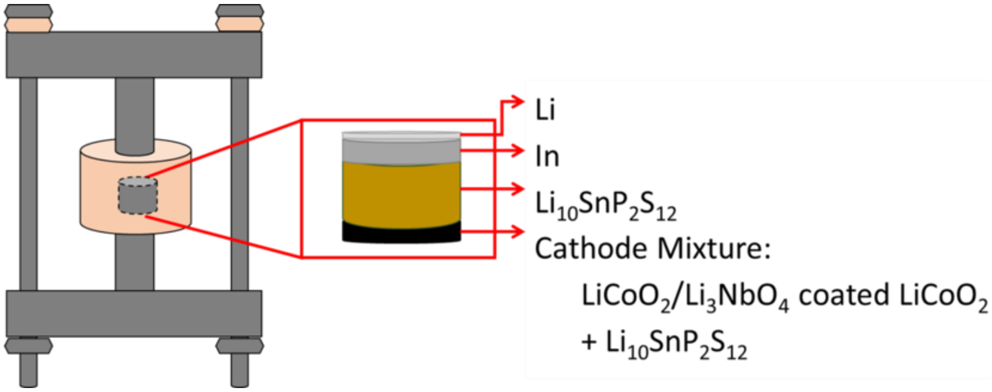

Figure 2-11. Schematic of the architecture of the cells tested in this chapter.

All cell preparation processes were carried in a glovebox (Lab Star, Mbraun, Germany, H_2O < 0.5 ppm, O_2 < 0.5 ppm). The ASS cells with 20 MPa pressure were then ready to be tested. A photograph of a disassembled pellet cut in half can be seen in Figure 2-12. The layers are discreet, with the dark one being the electrode, and the grey one the electrolyte/separator. The full circumference of the indium foil is visible at the bottom.

Figure 2-12. Cross section of an ASSB pellet on a 2032 coin cell casing for size reference.

The cells were galvanostatically charged/discharged on a Neware cycler in the voltage range of 2.0 to 3.7 V vs. Li-In at 60 °C. AC EIS measurements were performed in a potentiostat (Versastat4, Ametek Scientific Instruments, USA). EIS of a cold-pressed SE pellet was performed at room temperature in a symmetrical cell using carbon foil as the electrodes in the frequency range of 1 - 10^6 Hz and with an amplitude of 5 mV. Similarly, EIS tests of the cells in the frequency range of 0.01-10^6 Hz and an amplitude of 10 mV were performed at various cycling stages. Cyclic voltammetry (CV) was carried out on LSPS pellets sandwiched between a stainless-steel plate and Li or In foil as electrodes at a scanning rate of 10 mV s^{-1} from 0 to 5 V.

2.3 CHARACTERIZATION OF THE SOLID ELECTROLYTE AND CATHODE MATERIALS

Figure 2-13a shows the crystal structure of LSPS, taken from the online database Materials Project.[42] LSPS shows a tetragonal structure with a space group $P4_2/nmc$; number 137. The lattice parameters are a = 8.854 Å and c = 12.851 Å. The three-dimensional percolating structure ensures high Li^+ conductivity. To verify the crystal structure of the as-received LSPS, X-ray powder diffraction was carried out, as shown in Figure 2-13b. Based on the above crystal structure, the standard XRD pattern of LSPS was also simulated using the Materials Studio's software, as also shown in Figure 2-13b. Our simulated XRD matches well with the result presented in Materials Project and other results given by Bron, Kuhn, and Tarhouchi et al.[18,20,43] As shown, the experimental XRD can be well indexed to the simulated XRD, indicating good phase purity of the LSPS powders. In addition, the sharp and well-defined diffraction peaks indicate good crystallinity of the SE.

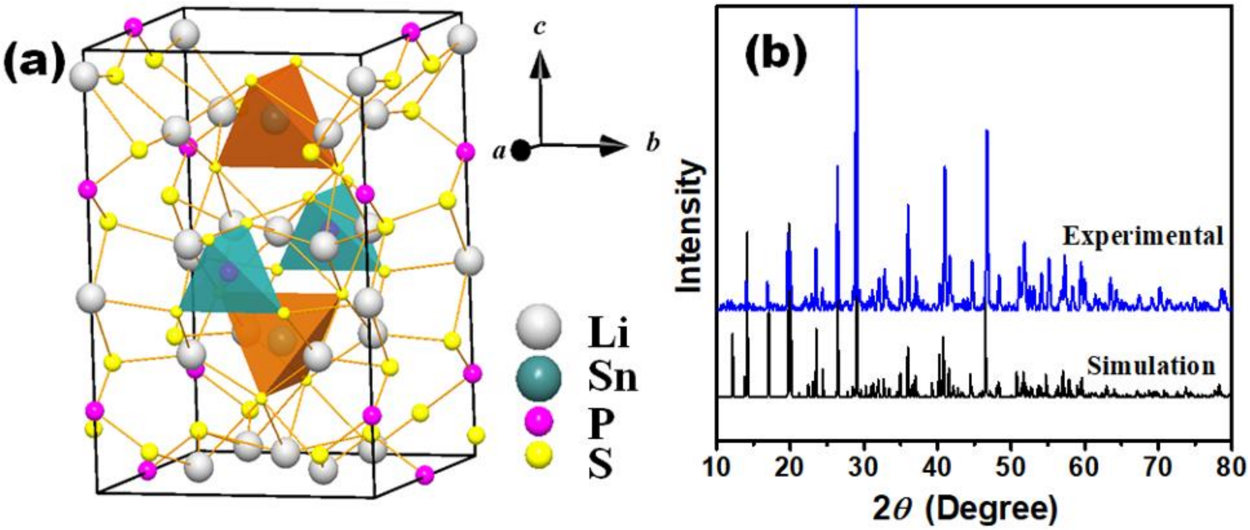

Figure 2-13. (a) Crystal structure of LSPS. [SnS_4] (Orange) and [PS_4] (Aqua) tetrahedra are shown. (b) Experimental and simulated powder X-ray diffraction (XRD) of LSPS.

Figure 2-14a shows the Nyquist plot for an LSPS pellet cold pressed at 500 MPa. Unlike the previous work reported by Bron et al., we observed grain resistance at room temperature. This could be due to the fact that they sintered their sample prior to testing, which reduces the grain resistance. The Nyquist plot can be well fitted by the equivalent circuit shown in the inset of Figure 2-14a. R_s, corresponding to the high-frequency intercept with the real axis, is the bulk resistance; the inductance segment L is mainly due to the cabling and leads of the set up ;[44] the R/CPE combination, showing as the semicircle at the mid-low frequency range, corresponds to the grain boundary contribution to the resistance and the corresponding capacitance of the LSPS pellet.[19] Based on the bulk resistance and geometry of the pellet, the total ionic conductivity of ~ 6 mS cm^{-1} at room temperature can be obtained for our cold-pressed LSPS sample, comparable to literature values.[18-20,45,46]

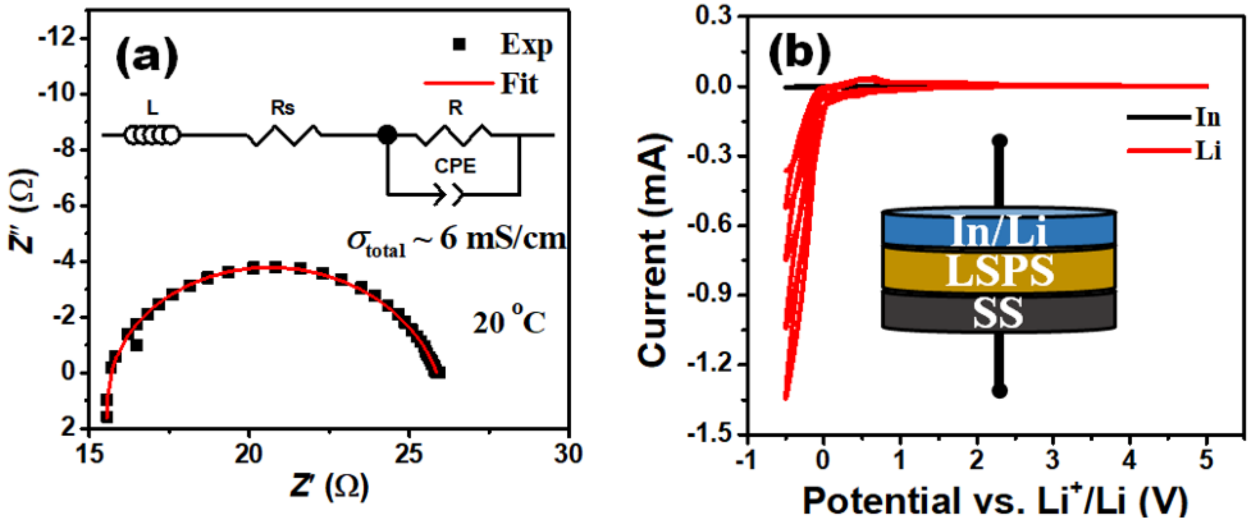

Figure 2-14. (a) Nyquist plot of the experimental (black square) and fit (red line) of a LSPS pellet in a C/LSPS/C cell at room temperature. (b) Cyclic voltammograms of the SS/LSPS/Li and SS/LSPS/In for the electrochemical stability window evaluation of the SE vs. Li & In between -0.5 and 5 V vs. Li$^+$/Li at room temperature.

To select an appropriate anode material, cyclic voltammetry was done on a cold pressed LSPS pellet. Figure 2-14b and Figure 2-15 show the cyclic voltammograms of LSPS to evaluate the electrochemical stability window in Li/LSPS/SS and In/LSPS/SS asymmetric cells. The red line in Figure 2-14ib s the CV curve for the Li/LSPS/SS setup. A slight cathodic peak, due to the deposition of metallic lithium ($Li^+ + e^- \rightarrow Li$), and a large anodic peak associated with the stripping of metallic lithium ($Li \rightarrow Li^+ + e^-$), are observed at around 0 V, similar to those of related systems.[20,45,46] On subsequent cycles, the peak currents gradually decrease (see detail: Figure 2-15).

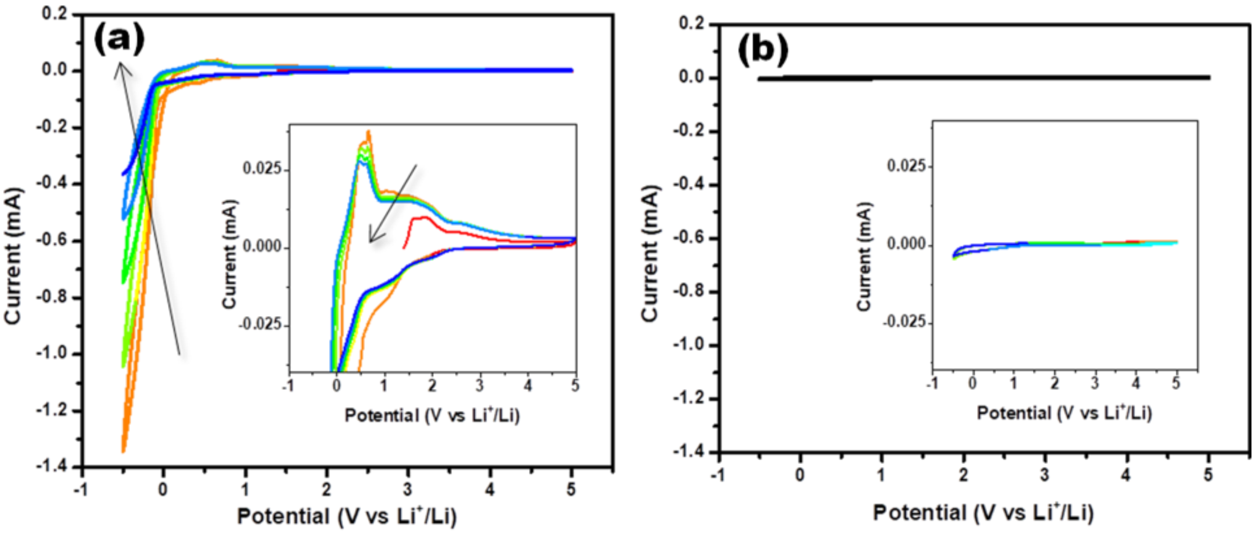

Figure 2-15. Cyclic voltammograms of the SS/LSPS/Li and SS/LSPS/In for testing the stability window of the SE between -0.5 and 5 V vs. Li$^+$/Li at room temperature. Insets show zoomed-in views of the sweeps.

It is well known that sulfide SEs are unstable against Li metal, which can cause a reduction of the SE upon contact with Li metal.[20] This is verified by the significant loss of current signal on the following cycles, further ascribed to the largely increased resistance from the interfacial reaction products. Impedance studies done by Tarhouchi et al. further confirm this, as they were able to show that impedance of a Li/LSPS/Li cell increases with time, as seen in Figure 2-16.[45]

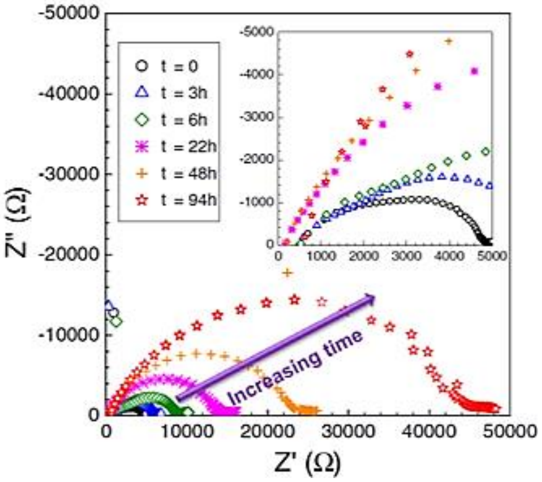

Figure 2-16. Room temperature impedance as a function of time of a Li/LSPS/Li cell.[45]

Similar studies, such as the one performed by Kuhn et al., showed similar trends, specifically the reduction peak observed at 1.4 V, corresponding to the reduction of thiophosphate, and the reduction peak at 0.8, corresponding to the reduction of thiostannate, seen in Figure 2-17c. Cycling at progressively slower potentials formed a passivating layer stable for at least 10 cycles (Figure 2-17 a & b).

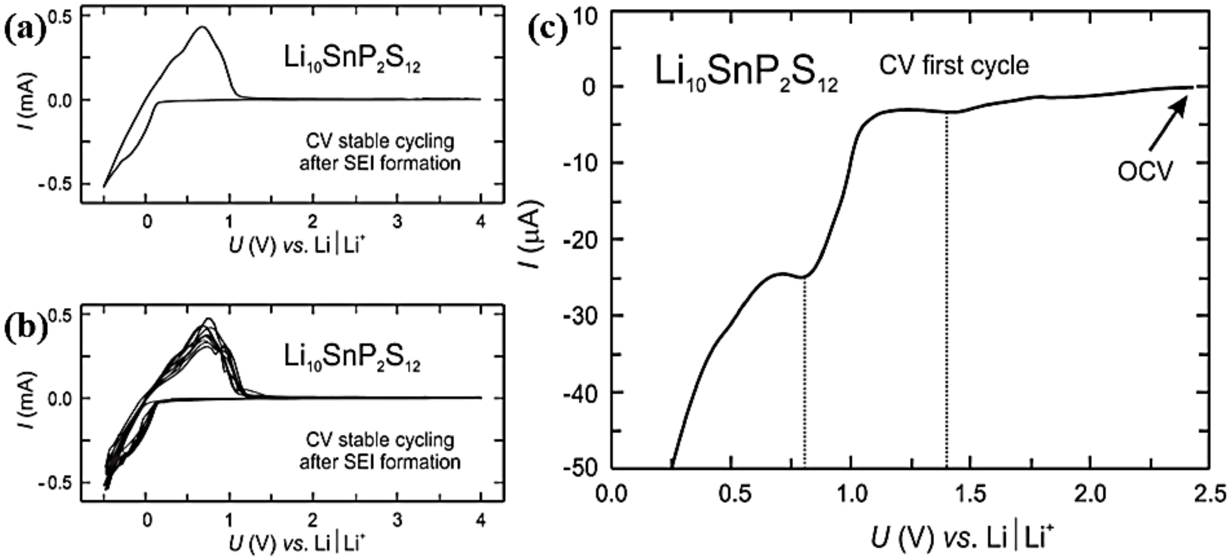

Figure 2-17. First (a) and 10 cycles (b) of the CV of a Li/liquid electrolyte/LSPS/Au cell, and (c) detail of (a).[20]

For the In/LSPS/SS setup, however, no noticeable changes in the cathodic and anodic peaks can be observed during the voltage sweep (Figure 2-15b, and black line in Figure 2-14b), implying no redox occurring in In/LSPS interface. Thus, Li-In alloys with a high oxidation potential of ~ 0.62 V vs. Li^+/Li and good ductility were chosen for our experiments to ensure good contact with LSPS and bypass any confounding factors arising from parasitic reactions during our electrochemical tests.

Figure 2-18a shows a SEM image of the LSPS SE as received. The particles are irregularly shaped oblongs with sizes of 1-10 μm and significant aggregations. EDS (Figure 2-19) shows a fairly uniform elemental distribution, consistent with the single phase XRD pattern. Similarly, Figure 2-18b and c show the SEM images of the pristine and Li_3NbO_4-coated LCO respectively, both of which have a chunk or irregular-shape morphology and a wide size distribution of 1-20 µm. EDS mapping of the coated sample shows a fairly even elemental distribution (Figure 2-20), consistent with its single phase XRD (Figure 2-21). The coating layer is invisible in SEM/EDS or XRD, primarily due to the thin and low volume percentage of the coating (only 5 ALD cycles and ~ 0.5 nm thick).

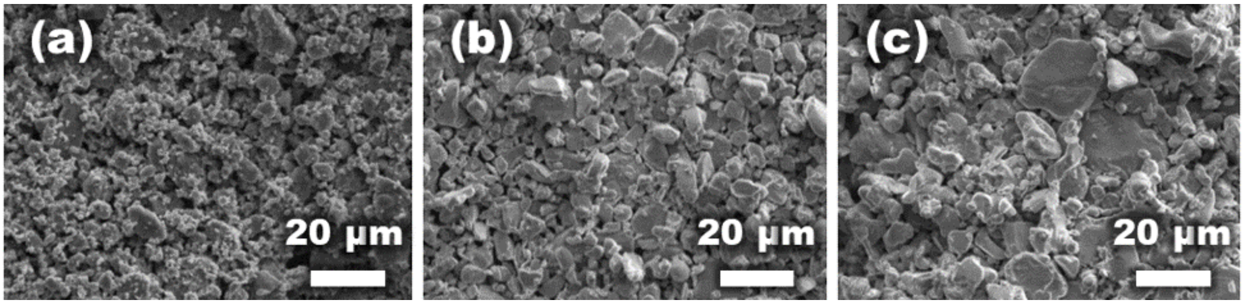

Figure 2-18. SEM images of the (a) LSPS, (b) uncoated LCO, and (c) c-LCO powders.

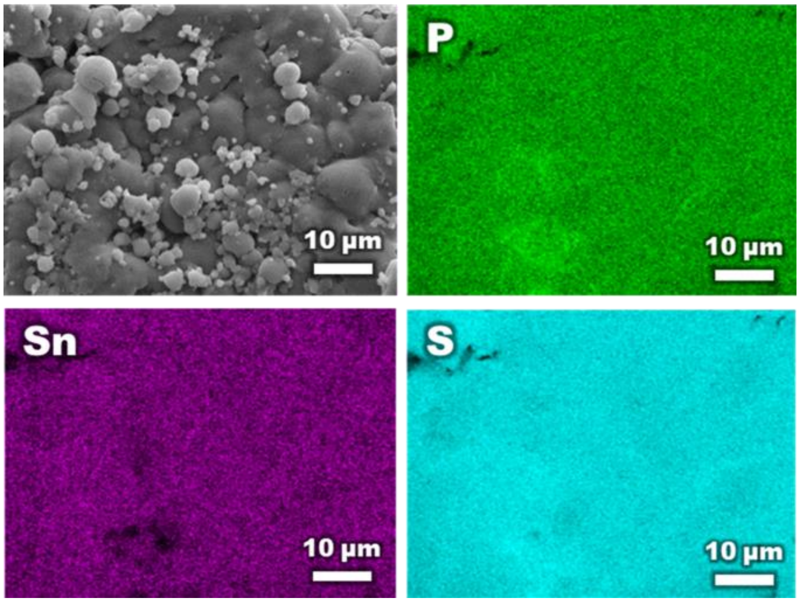

Figure 2-19. SEM image of the LSPS and EDS mappings of P, Sn, and S.

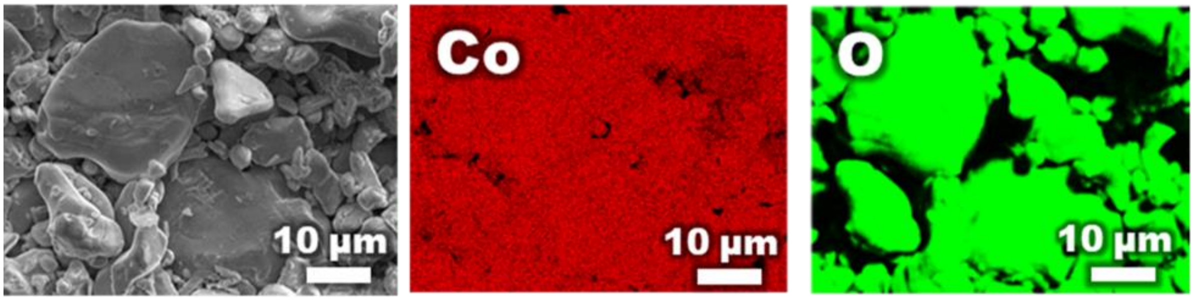

Figure 2-20. SEM image of the c-LCO and EDS mappings of Co, and O.

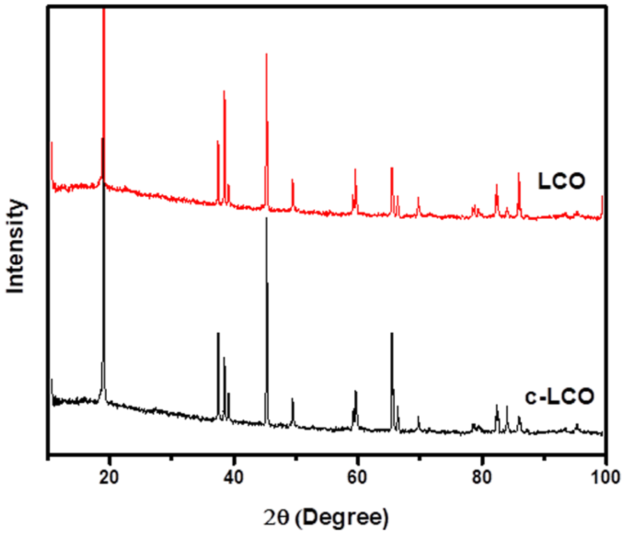

Figure 2-21. Powder X-ray diffraction patterns of LCO (top) and c-LCO (bottom).

2.4 ELECTROCHEMICAL PERFORMANCE OF THE ALL-SOLID-STATE CELLS

In order to study the electrochemical performance of the SE and its compatibility with LCO, ASSBs with pristine and c-LCO were fabricated and tested. Figure 2-22 shows a comparison of the cycling stability between LCO and c-LCO. First, LCO shows a low discharge capacity of ~ 105 mAh/g at C/10 and 60 °C, much lower than the value achieved in liquid cells (~145 mAh/g at an upper cut-off of 4.3 V vs. Li^+/Li).[47] More importantly, the initial Coulombic efficiency is only 82%, also much lower than that of liquid cells (98%).[47] The significant initial capacity loss indicates an interfacial instability between LSPS and LCO that consumes Li in order to form an

SEI. The large voltage polarization of the LCO cell, visible in Figure 2-23, also indicates its large interfacial impedance. The LCO cell activates its discharge capacity to ~110 mAh/g in the 2nd cycle and then experiences a severe capacity decay, only retaining ~ 60% initial capacity after 70 cycles.

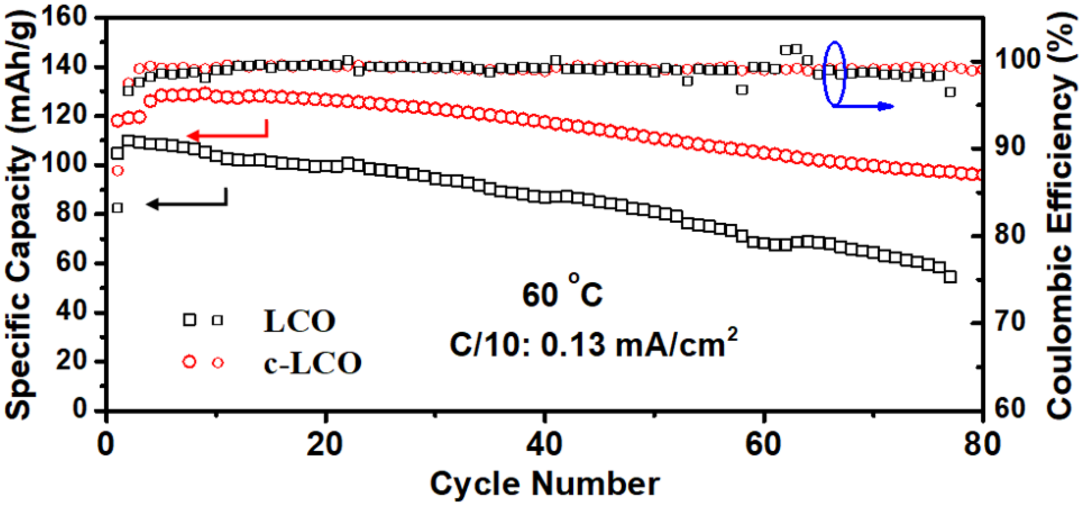

Figure 2-22. Cycling performance of LCO/LSPS/Li-In and c-LCO/LSPS/Li-In between 2.0 and 3.7 V vs. Li-In (2.62-4.32 V vs. Li^+/Li) at C/10 (0.13 mA/cm^2) and 60 °C.

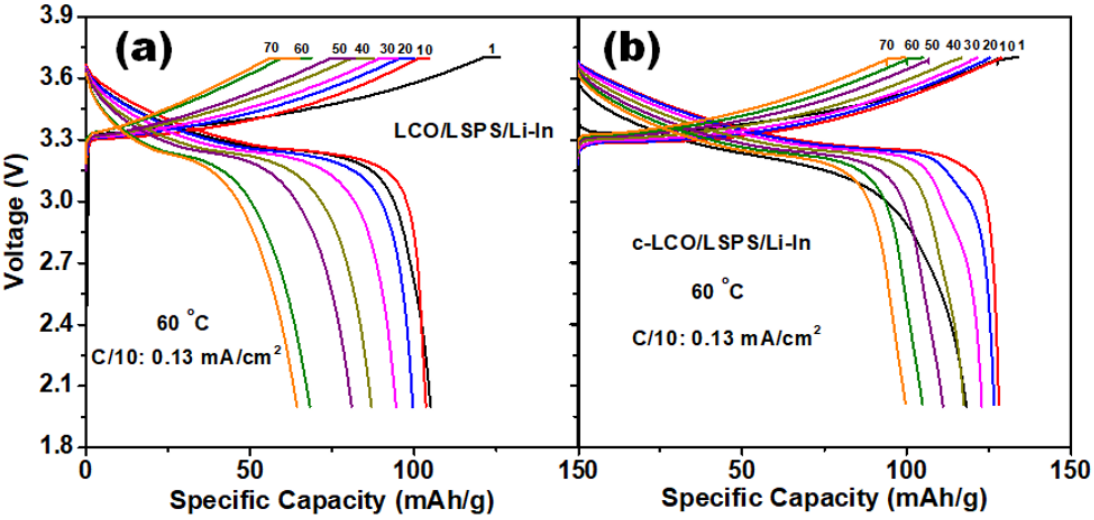

Figure 2-23. Voltage profiles of the (a) LCO/LSPS/Li-In and (b) c-LCO/LSPS/Li-In shown in Figure 2-22.

The large capacity decay of the LCO cell is accompanied by a large voltage decline. For instance, the overpotential increases from 51 mV for the 1st cycle to 26 mV on the 10th cycle and gradually decreases to 49 mV by the 70th cycle, as seen in Figure 2-24, and summarized in Table 2-2. The large voltage decline is a consequence of a radically increasing LSPS/LCO interfacial resistance, contributing to the severe capacity decay, together with the active material loss, as LCO is consumed by the reactions with LSPS which will be discussed later.

Table 2-2. Summary of overpotentials of LCO and c-LCO.

Cycle	LCO (mV)	c-LCO (mV)
1st	51	46
10th	26	11
70th	49	47

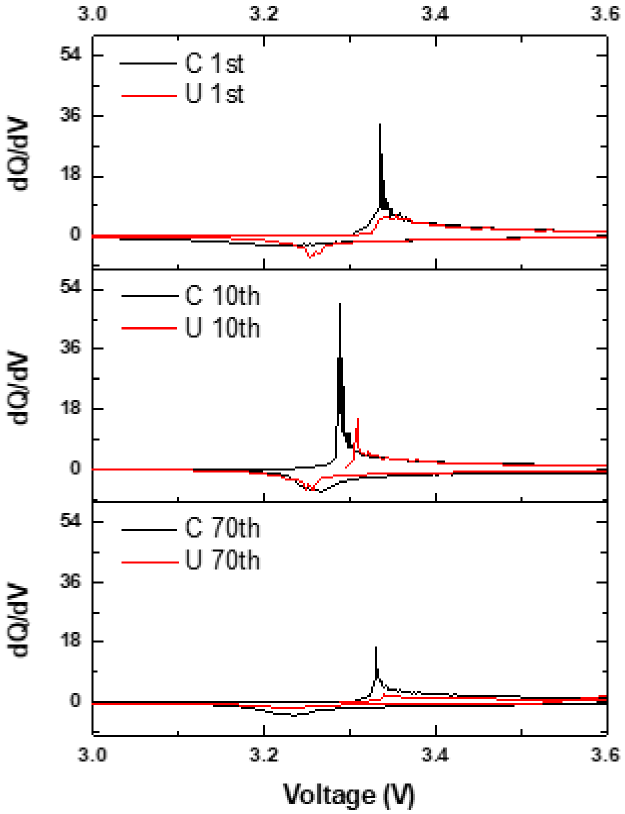

Figure 2-24. Summary of dQ/dV for the 1st, 10th, and 70th cycles.

The c-LCO cell shows not only a higher discharge specific capacity but also better cycling stability. The initial specific discharge capacity and Coulombic efficiency of the c-LCO cell are ~ 118 mAh/g and ~ 87%, respectively, as seen in Figure 2-22. Its capacity gradually activates to ~127 mAh/g by the 5th cycle, consistent with the decreasing overpotential and interfacial impedance of the cell. The activation process presumably originates from the interface activation (improved particle contact, SEI formation, void filling, etc.). Since Li_3NbO_4 is stable against both LCO and LSPS, the coating largely avoids the direct physical contact of LCO and LSPS and thus mitigates their chemical reactions, protecting the interface in the following cycles. In addition, due to the buffering effect of Li_3NbO_4, the SCL and resultant resistance is largely reduced. These two effects contribute to stable LCO/Li_3NbO_4/LSPS interfaces and thus much better cycling stability. The c-LCO cell retains ~ 85% initial capacity after 70 C/10 cycles, significantly outperforming the LCO cell.

The initial capacities of the uncoated and coated LCO, as well as their cycling behavior, is well consistent with those of other LCO ASSBs.[48] The most remarkable cycling properties of the LCO and c-LCO cells were summarized in Table 2-3 for easier comparison.

Table 2-3. Summary or cyclic performance of LCO and c-LCO.

Property at C/10 and 60 °C	LCO	C-LCO
Initial discharge specific capacity	105 mAh/g	118 mAh/g
Initial Coulombic efficiency	82%	87%
Capacity retention after 70 cycles	60%	85%

Figure 2-25 shows the rate capability of the LCO and c-LCO ASSBs. Due to severe interfacial instability and thus resistance, pristine LCO shows poor rate capability and cycling stability. The LCO cell only shows a low initial capacity of ~77 mAh/g and loses almost 75% of its capacity in the first 5 cycles at C/20. The extremely low initial capacity may relate to severe side reactions of LCO/LSPS at the slow charge process (C/20). The cell shows even lower capacities at higher C-rates: ~20 mAh/g at C/10, 10 mAh/g at C/5, and no observable capacity at C/3 or higher. In addition, the LCO cell only retains 15 mAh/g discharge capacity when cycled at C/10 again, implying the failure of the cell. Conversely, the c-LCO cell has a much better rate capability, showing a discharge capacity of ~120 mAh/g at C/20, 115 mAh/g at C/10, 95 mAh/g at C/5, 70 mAh/g at C/3, and 20 mAh/g at 1C, as shown in Figure 2-25. After the high-rate cycles, the c-LCO cell can recover ~ 95% initial capacity at C/10, corroborating it's much better cyclability. A comparison of voltage profiles, shown in Figure 2-25b, clearly indicates higher discharge voltages and lower overpotentials of the c-LCO cell, as compared with the LCO cell. The significantly improved cycling stability and rate capability of the c-LCO cell are primarily originated from the reduced interfacial resistance and improved interfacial stability, which will be discussed in more details below.

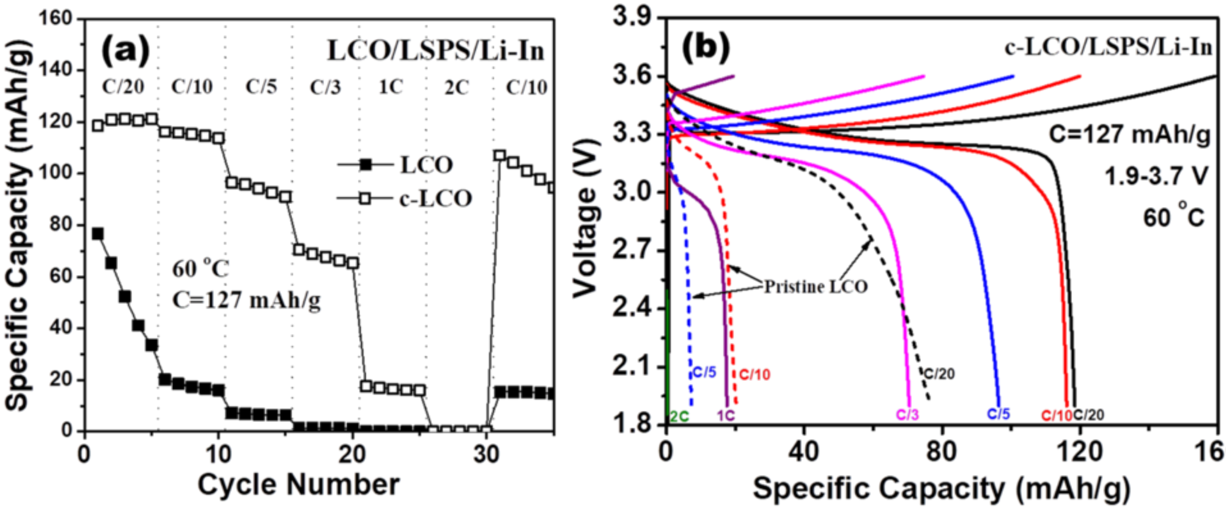

Figure 2-25. (a) Rate capability of LCO/LSPS/Li-In and c-LCO/LSPS/Li-In between 2.0 and 3.7 V vs. Li-In (2.62 - 4.32 V vs. Li^+/Li) at 60 °C. (b) Voltage profiles at different rates of LCO/LSPS/Li-In (dashed lines) and c-LCO/LSPS/Li-In (solid lines).

2.5 ELECTROCHEMICAL IMPEDANCE SPECTROSCOPY STUDY

As demonstrated above, surface coating to physically separate LCO and LSPS is indispensable for employing this highly conductive and technically feasible SE. The improved interfacial stability is evidenced by the enhanced cycling stability and rate capability, which can be further clarified by monitoring the impedance evolution with cycling. Figure 2-26a and b depict the room temperature Nyquist plots of the LCO and c-LCO cells respectively at different cycling stages. The Nyquist plots could be well fitted by the equivalent circuit shown in the inset of Figure 2-26a, which contains the serial combination of internal resistance R_S (high frequency intercept with real axis), interfacial resistance R_{sei} (high frequency semicircle, ~100 kHz), charge transfer resistance R_{ct} (low frequency semicircle, ~500-600 Hz), and Warburg element representing the solid-state ion diffusion (low frequency tail), as well the respective constant phase elements (CPE) associated with R_{sei} and R_{ct}.[33-36] The fitting results of R_S, R_{sei}, and R_{ct} are summarized in Figure 2-27.

The internal resistance of the as-prepared cells, including the resistances from cathode, anode, separator, current collectors, and leads, are ~30 Ω for the LCO cell and ~42 Ω for the c-LCO cell; the higher R_S of the c-LCO cell is mainly due to the electronic insulating coating. The significant R_S drop after the 1st cycle for both cells is primarily attributed to improved contact and the activation of particles after high-temperature cycling. The c-LCO cell keeps its low R_S (11 Ω) after 10 cycles, while the LCO cell shows largely increased R_S (37 Ω), consistent with its interfacial instability.

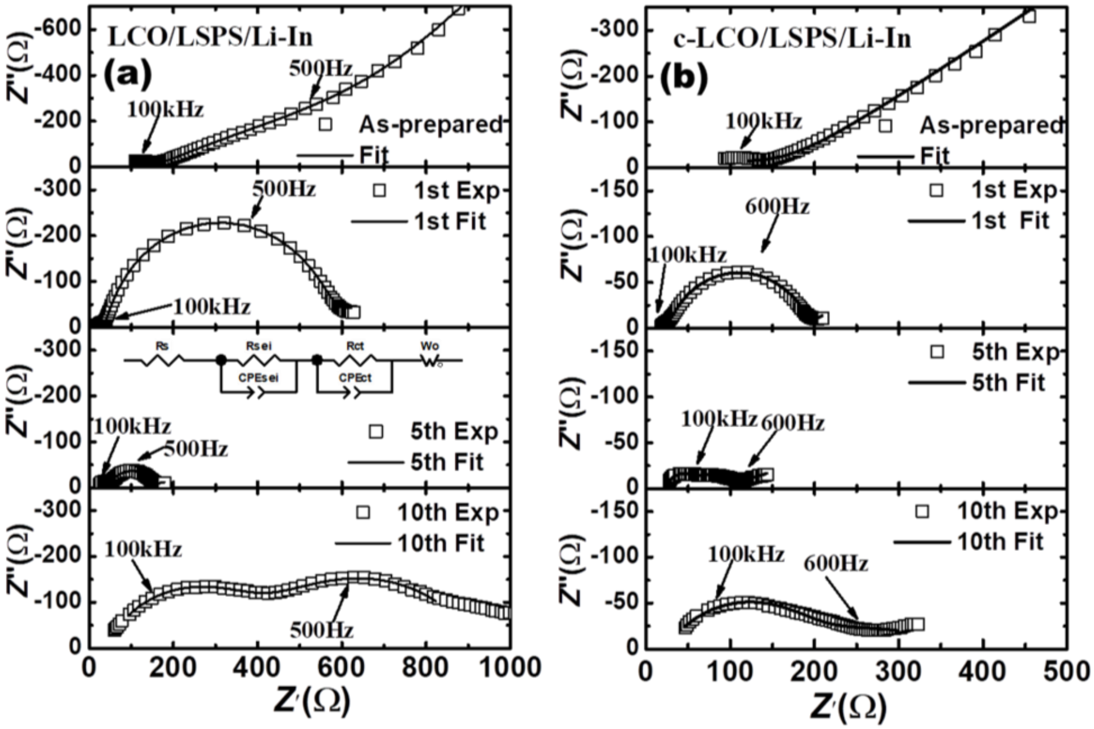

Figure 2-26. Room Temperature Nyquist plots of (a) LCO/LSPS/Li-In and (b) c-LCO/LSPS/Li-In at different cycling stages (as-prepared and after 1st, 5th, and 10th charge).

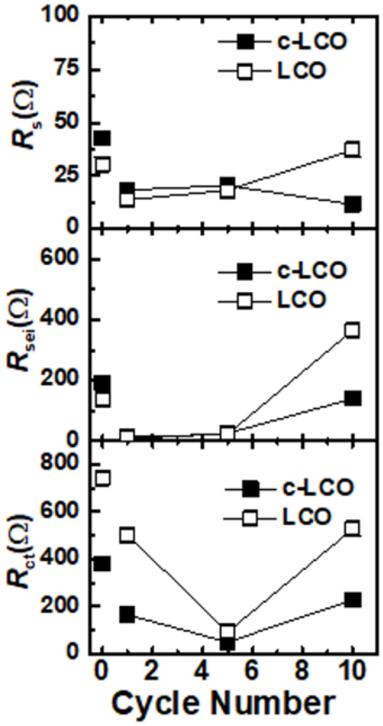

Figure 2-27. Summary of R_s, R_{sei}, and R_{ct} with cycling derived from EIS fitting.

Due to the air and moisture-sensitivity of LSPS, the LSPS particle surface is inevitably contaminated and forms a passivating layer. Although LCO is stable in air, its surface could also absorb trace amounts of H_2O, which further contaminates the LSPS surface when mixing and assembling them together. These facts could account for the large R_{sei} of the as-assembled LCO (~191 Ω) and c-LCO cells (~ 130 Ω). The smaller R_{sei} of the c-LCO cell is primarily originated from the surface protection that mitigates the reactivity and additional SEI film formation in LCO/LSPS interface in the composite cathode. Interestingly, after the initial charge at 60 °C the R_{sei} of both cells almost disappears (~10 Ω). This phenomenon is intriguing, and we speculate that it is mainly ascribed to the surface cleaning process of LSPS, which removes the passivation layer. The specific origin of this phenomenon, however, needs further experimental and theoretical efforts. R_{sei} increases slightly to ~25 Ω after 5 cycles, however, it jumps to large values of ~365 Ω and ~140 Ω for the LCO and c-LCO cells after 10 cycles, respectively. The significant increase in R_{sei} clearly indicates the interfacial instability between LCO and LSPS, which could originate from chemical reactions, mutual elemental diffusions, etc. The interfacial analyses will be presented below to clarify this. The thin Li_3NbO_4 coating does improve the interfacial stability of LCO/LSPS, although it cannot completely get rid of the R_{sei}. Similar effects can be found for ASSBs with other coated materials.[22,26,29,34,36,48,49]

Large charge transfer resistances R_{ct}, ~743 Ω and 379 Ω for the LCO and c-LCO cells, respectively, can be observed which are mainly originated from the resistive surface layers resulting from surface contamination of LSPS and the reactivity of LSPS/LCO. The resistive surface layers not only impede Li^+ transfer but also limit the electron transfer across active particle surfaces. Similar to the R_{sei}, R_{ct} also experiences an activation process during the first several cycles. After the fifth cycle, R_{ct} reduces significantly to 91 and 49 Ω for the LCO and c-LCO cells, respectively. The decrease in R_{ct} should share the same origin as that of R_{sei}, associated with the removal of the passivation layer on the particle surfaces and/or increased contact area. In addition, the lower R_{ct} of the c-LCO cell is mainly ascribed to the surface protection by the coating, which largely prevents the formation of a thick SEI.[22,50,51] The activation process, including the reduction of all three resistances, agrees well with the reduction of overpotential and increased specific capacity in the first few cycles, as shown in Figure 2-22. The capacity and impedance activation process are widely observed in ASSBs[52] and liquid cells with surface sensitive active materials, such as NMC811.[53] After 10 cycles, R_{ct} increases significantly to ~530 Ω and 230 Ω for the LCO and c-LCO cells, respectively. It is obvious that the SEI and charge transfer resistances dominate the cell performances, including the cycling stability and rate capability. After 10 cycles, the LCO cell shows a large total resistance of ~ 930 Ω, much larger than that of the c-LCO cell (~ 378 Ω). The resistance of the LCO cell will keep increasing without forming stable interfaces, and finally terminate the cell due to a strong voltage polarization. Surface coating with Li_3NbO_4 largely improves the interfacial stability, and thus the cycling stability and rate capability, as demonstrated in other studies.[22,27,33,50,51]

2.6 TEM ANALYSIS OF LSPS/LCO AND LSPS/C-LCO INTERFACES

To better understand the LCO/LSPS interfacial behavior and the effects of the surface coating, TEM observations of the composite cathodes were carried out to directly visualize the LCO/LSPS interface. The ASSBs were disassembled after 10 C/10 cycles at 60 °C. Figure 2-28a shows a TEM image of the LCO/LSPS interface. A thick passivating layer with gradually varying contrast can be observed in between them. An EDX line scan across the interface confirms the interface thickness of ~ 18 nm. The variations of Co, Sn, and P elements at the interface show that the mutual diffusion length is ~5 nm on both sides. Particularly, Sn is significantly depleted in the LSPS side, indicating that Sn deeply migrates into LCO.

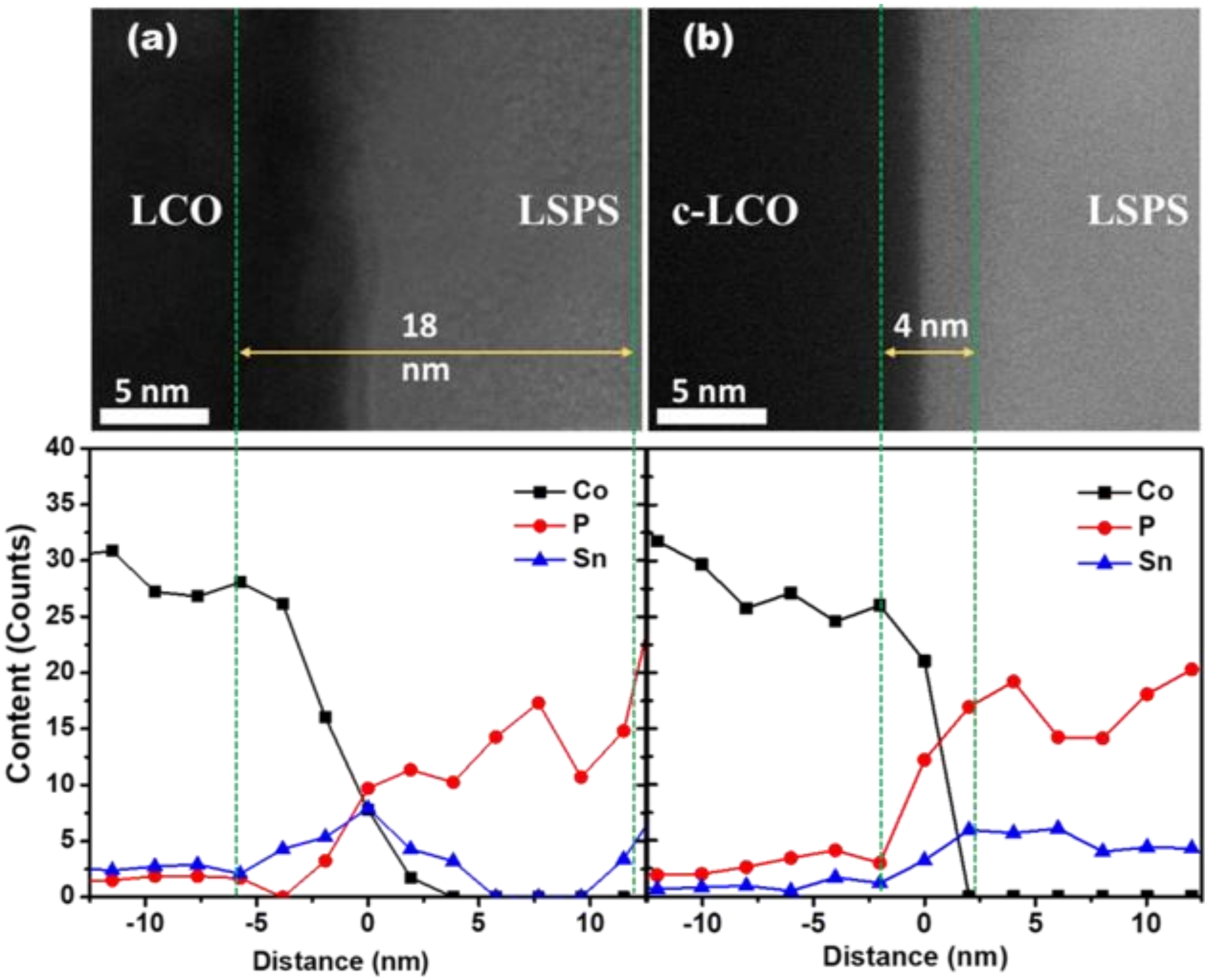

Figure 2-28. TEM images and corresponding EDX line scans of (a) LCO/LSPS and (b) c-LCO/LSPS interfaces after 10 C/10 cycles at 60 °C.

A high resolution TEM image, shown in Figure 2-29, indicates that the interface seems to be composed of crystalline nanoparticles, which are most likely cobalt and/or tin sulfides. Similar results have been found for Li_2S-P_2S_5 SEs interphases.[34,49] The interfacial layer, mostly consisting of sulfides, is highly resistive for both Li^+ and electron transport, primarily resulting in the high resistance and considerable overpotential of the LCO/LSPS/Li-In cell. We also believe that there exists a Li^+ depletion layer, and thus a SCL, partially contributing to the poor electrochemical performance.

Sakuda et al. coated LCO particles with CoS in order to prove that the origin of the impedance was due to structural mismatch between the cathode and electrolyte materials; however, the CoS they formed through thermal decomposition has an electrical conductivity of 1.7 S/cm, highly conductive when compared to CoS synthesized by other methods, which have electrical conductivities in the 1.5 x 10^{-7} S/cm range.[54] Were the compound to be a tin sulfide, the electrical conductivity of SnS is in the order of 10^{-4} S/cm, which is still fairly resistive relative to the other materials in the cell.[55] It is possible that the CoS formed at the interphase is of the insulating conformation, which would be consistent with our findings of high charge transfer impedances.

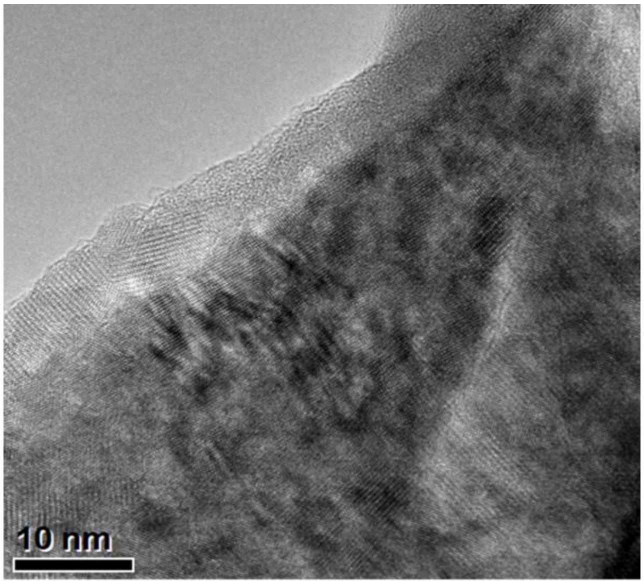

Figure 2-29. TEM image of the LCO/LSPS interphase after 10 C/10 cycles at 60 °C.

Figure 2-28b shows a TEM image of the c-LCO/LSPS interface after 10 C/10 cycles at 60 °C. Due to the ultrathin coating and beam-sensitivity of Li-ion conductors, Li_3NbO_4 is undetectable. A clear and narrow interface, however, can be observed, as compared with that of the LCO/LSPS interface. The EDX line scan of the Co, Sn, and P elements across the interface shows a thin inter-diffusion length of ~ 4 nm. Co diffusion into LSPS was completely blocked, and P and Sn diffuse ~ 4 nm into c-LCO. It is evident that the ultrathin coating layer largely impedes the atomic inter-diffusion and thus decreases the interfacial resistance, especially within the composite cathode in this study. The Li_3NbO_4 coating, as suggested,[56] also presumably alleviates the SCL formation, further reducing the Li^+ transfer resistance. As shown in Figure 2-27, the c-LCO cell still suffers substantial impedance growth after 10 cycles, probably due to the ultrathin coating in this work. Further optimization of the coating thickness is required to improve the interface behavior and cycling performance.

2.7 SUMMARY

All solid-state batteries with $LiCoO_2$ cathodes, $Li_{10}SnP_2S_{12}$ solid electrolyte, and Li-In anode were fabricated to evaluate the electrochemical performance of low-cost $Li_{10}SnP_2S_{12}$ and its interfacial behavior with $LiCoO_2$. Poor cycling stability and rate capability can be observed for the cell with pristine $LiCoO_2$, primarily due to the instability of the LCO/LSPS interface. Considerable atomic inter-diffusion causes a thick interphase layer and significantly increases the interfacial resistance, resulting in large voltage polarizations and poor cyclability. Surface coating of ultrathin Li_3NbO_4 on $LiCoO_2$ by atomic layer deposition drastically improves the cycling and rate performance of the ASSBs over the cell with pristine $LiCoO_2$. The enhanced electrochemical performance is further traced back to the decreased charge transfer and interfacial resistances, originated from the mitigation of atomic inter-diffusion and the formation of resistive interphases. Our study also demonstrated that ALD coating with thin layer oxide-based Li-ion conductors is imperative and effective for the utilization of sulfide-based SEs for ASSBs.

Based on the above results, in order to use the highly conductive and cost-effective LSPS in ASSBs, surface protection of the cathode materials is necessary, at least for the layered cathodes, i.e., LCO, NMC, NCA. The high reactivity of sulfide-based SEs against oxide-based cathodes mainly originates from the significant difference in chemical potential between them. However, sulfide-based electrolytes have their merits: high ionic conductivity and good deformability, as compared with oxide-based SEs. Thus, the high reactivity of sulfide-based SEs is hard to completely solve. Here we successfully demonstrate that an ALD coating with ultrathin layered oxide-based Li-ion conductors is not only effectively at protecting the active-material/SE interface, but doesn’t introduce noticeable interfacial resistance, thus mitigating the cell impedance and its build-up with cycling.

Chapter 3. Electrolyte Selection for Li_2MCl_4 Cathodes

3.1 INTRODUCTION

3.1.1 *The Li_2MCl_4 System as Potential Cathode Material*

The Li_2MCl_4 family of materials had been studied as lithium ion conductors, due to what at the time was the highest lithium ionic conductivity with values around 0.01 mS/cm at room temperature.[57,58] If M is a transition metal, it was speculated that it would be part of a redox couple due to the multivalent nature of the transition metals, opening the possibility of an electrode material with high ionic conduction. These lithium transition metal chlorides have a large amount of Li per mol, suggesting a possibly large capacity.[59] Table 3-1 shows the calculated theoretical specific capacity, assuming the reversible extraction of 1.2 Li^+ per chemical formula as speculated by Kajiyama et al.[59] This specific capacity is better than that of other commercialized cathode materials such as $LiCoO_2$ at 137 mAh/g or $LiFePO_4$ at 150 mAh/g,[60] but significantly lower than NMC 811 at almost 200 mAh/g when extracting 0.5, 0.7, and 0.7 Li^+ per formula unit, respectively. If more than 1.2 moles of lithium can be experimentally extracted, there is potential for even higher specific capacities.

Table 3-1. Theoretical specific capacity for the extraction of 1.2 Li^+ per chemical formula.

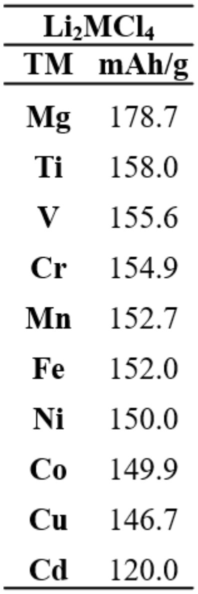

Li_2MCl_4	
TM	**mAh/g**
Mg	178.7
Ti	158.0
V	155.6
Cr	154.9
Mn	152.7
Fe	152.0
Ni	150.0
Co	149.9
Cu	146.7
Cd	120.0

Similarly, Li_2MCl_4 is potentially cheaper than the aforementioned cathode materials. Figure 3-1shows the cost per gram of material, they can be compared to the cost of some commonly used cathode materials, shown at the top of the chart. The values were calculated by averaging the two lowest prices found for precursor materials of similar purity, except for VCl_2, which was only found for 85% purity, and $TiCl_2$, for which only one supplier was found. This cost is just for the material cost. When considering new cathode materials, manufacturing costs should also be considered. Traditional cathode materials are typically synthesized by solid state reactions. These processes generally involve high temperature calcination of around 900 °C for prolonged periods of times, sometimes under an inert atmosphere which is expensive.[61] However, Li_2MCl_4 materials have been synthesized at 400 °C,[58,62,63] a significant reduction in energy, and therefore, cost.

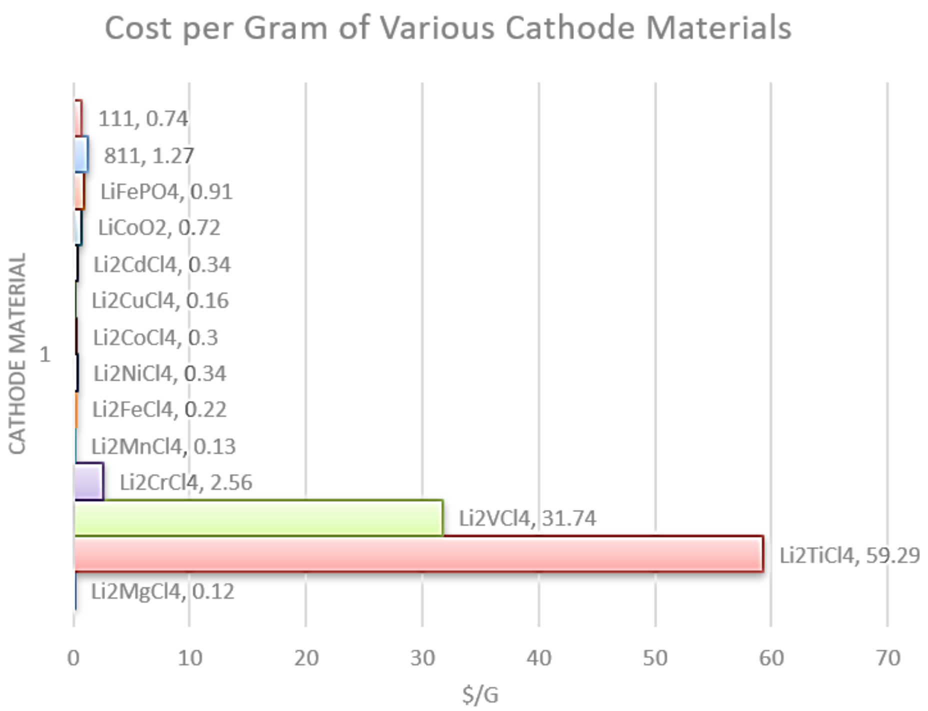

Figure 3-1. Cost per gram comparison of various cathode materials.

Another appealing quality is that the Li_2MCl_4 family of materials contains some low toxicity options. Unlike LCO, 811, or 111, Li_2MCl_4 has some analogues that are safer and less toxic, primarily due to them not having cobalt, such as Li_2MgCl_4, Li_2CuCl_4, Li_2FeCl_4, among others. Some, of course, would presumably have a considerable toxicity, such as the cadmium, chromium, and vanadium containing compounds, and of course, the cobalt containing one. Last, but not least, is the fact that there are compounds in the Li_2MCl_4 family of materials that are made of earth abundant and high production materials. Most notably, the US is one of the largest producers of chlorine, and produces large amounts of iron, magnesium, cadmium and copper.[64] Conversely some of the compositions contain elements that are less abundant or largely imported such as nickel, cobalt and chromium, some of which are required for the currently used battery compositions.[64]

3.1.2 *Structure of the Li_2MCl_4 System*

Several of the compositions of the Li_2MCl_4 family present the inverse spinel structure, space group $Fd\bar{3}m$, specifically the ones where M = Mg, Mn, Fe, Cd, and V.[58,62,65-67] In the inverse spinel structures half of the Li are in tetrahedral positions, surrounded by chlorine ions, and the other half are distributed with the M ions in octahedral positions without 1:1 ordering. Figure 3-2 shows this structure without the lithium atoms; the purple spheres represent M, and the green ones are the chlorine ions. These materials present a phase transition at elevated temperatures (between 300-400 °C) to defect NaCl; however, an increase in temperature below the transition temperature only causes an increase in the disorder of Li^+.[58,62,65-67] This increase in disorder is due to the gradual migration of Li from the 8a tetrahedra to 16c octahedra with no other structural changes: an order-disorder transformation.[67]

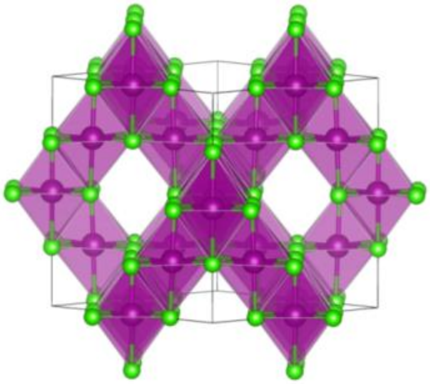

Figure 3-2. Inverse spinel structure of the Mg, Mn, Fe, Cd, and V containing materials. The purple spheres represent the metals in the octahedral positions and the green ones the chloride ions. [MCl_6] octahedra are shown.

Of the characterized compounds of the Li_2MCl_4 family of materials, several them do not present the inverse spinel structure, such as M = Ti, Cr, Co, Ni, Cu, and Zn. The Zn containing material, for example, exhibits an olivine structure with Li in the octahedral positions and Zn in the tetrahedral ones in an hcp arrangement of anions.[57] The structure of Li_2CoCl_4 is derived from the inverse spinel structure, space group *Imma*. In this structure, half of the Li occupy tetrahedral sites, and Co and the other half of the Li occupy octahedral sites with 1:1 ordering of the cations, unlike with the inverse spinel structure, as depicted in Figure 3-3a.[68] Li preferentially aligns along the b axis, while Co aligns over the a axis. [68] This ordering of the octahedral positions, born from the Jahn-Teller effect, distorts the symmetry from cubic to orthorhombic.[57]

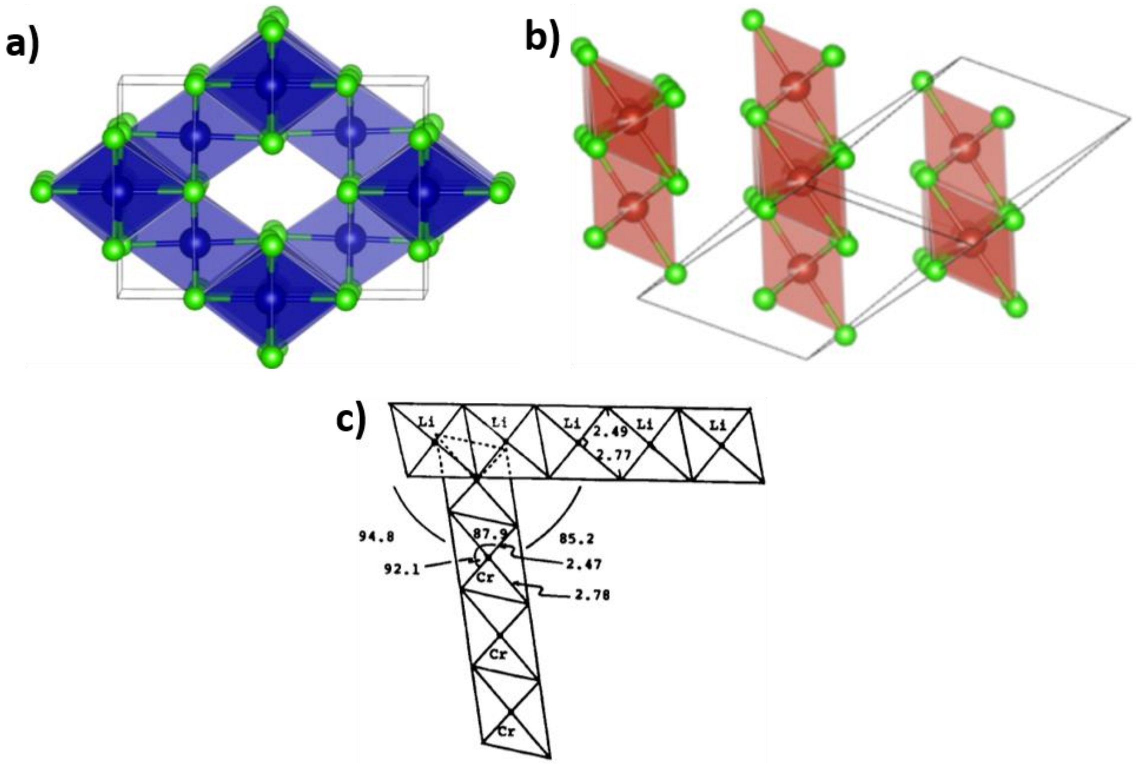

Figure 3-3. Orthorhombic (a) and monoclinic (b) structures of the cobalt and chromium containing materials, respectively. The blue and orange spheres represent the transition metals and the green ones the chloride. $[MCl_6]$ octahedra are shown. (c) Schematic illustrating the difference evolution from orthorhombic to monoclinic.[63]

The Jahn-Teller instability of the Cr^{2+} high spin configuration in the d^4 state present in Li_2CrCl_4 elongates the $CrCl_6$ octahedrals further distorting the structure to a monoclinic symmetry, seen in Figure 3-3b.[63] The difference between the Imma orthorhombic structure and the *C2/c* monoclinic one is the angle between the rows of M and the rows of Li. In the orthorhombic structure (M = Co), the octahedras of Co are at 90° angles to the octahedras of Li, while in the monoclinic one (M = Cr), the octahedras of Cr are at 85.2° angles to the octahedras of Li, as seen in Figure 3-3c, and said Cr octahedras are connected in such way that the elongated axis is in the same direction.[57]

The orthorhombic, as well as the monoclinic structures, have a phase transformation to the inverse spinel at higher temperatures, and eventually to a defect NaCl structure, as the inverse spinel compounds do.[57] A schematic summary of the relationship between the cubic inverse spinel structure, and its orthorhombic and monoclinic distortions, can be seen in Figure 3-4, which easily illustrates the structural evolution. Other compositions, such as the Ti containing one, have poor crystallinity at stoichiometric compositions, and the Ni and Cu have no intermediate compounds at the stoichiometric composition.

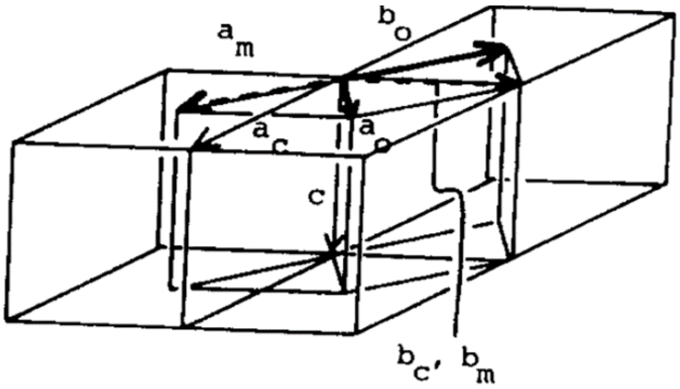

Figure 3-4. Relationship between the cubic inverse spinel lattice and the orthorhombic and monoclinic lattice distortions. The subscripts c, o, and m represent which lattice they belong to, respectively.[63]

3.1.3 *Ionic Conductivity Studies of the Li_2MCl_4 System*

As previously mentioned, the initial interest shown for these materials in the 70s and 80s was due to their high ionic conductivity; therefore, a lot of research has gone into studying the conductivity of said materials. As seen in Figure 3-5, the materials with the inverse spinel structure have the higher ionic conductivity values (M = Fe, Cd, Mg, Mn). This is because the inverse spinel structure provides Li ions with a three-dimensional (3D) framework structure for intercalation, aiding the lithium's movement in and out of the particles. The conduction path was determined to be along the [111] direction by Li ions going from 8a tetrahedra to 16c octahedra back to 8a tetrahedra.[57,67,68] Meanwhile, in the orthorhombic and olivine configurations, such as the one seen in M = Co and Zn respectively, the conduction path is 1D only, through the octahedral spaces along the a axis only, and a similar reason is speculated to be behind the monoclinic structure's low ionic conductivity.[57,63]

Furthermore, conductivity knees can be found in Figure 3-5. The ones below ~300 °C are ascribed to order-disorder type transformations. As temperature increases, an increase in the disorder on the octahedral sites gives rise to the appearance of inverse cubic spinel phases in the distorted structures.[57,58,62,63,65,66,68] The conductivity knees found above ~300 °C are related to phase transformations into a defect NaCl type structure. [50,51,53] Li_2FeCl_4 has two lines in Figure 3-6 due to the possibility of producing a distorted phase at lower temperatures;[62] the transition temperature from orthorhombic to inverse spinel is at about 130 °C,[62] and as expected, has an ionic conductivity lower than that of the spinel.

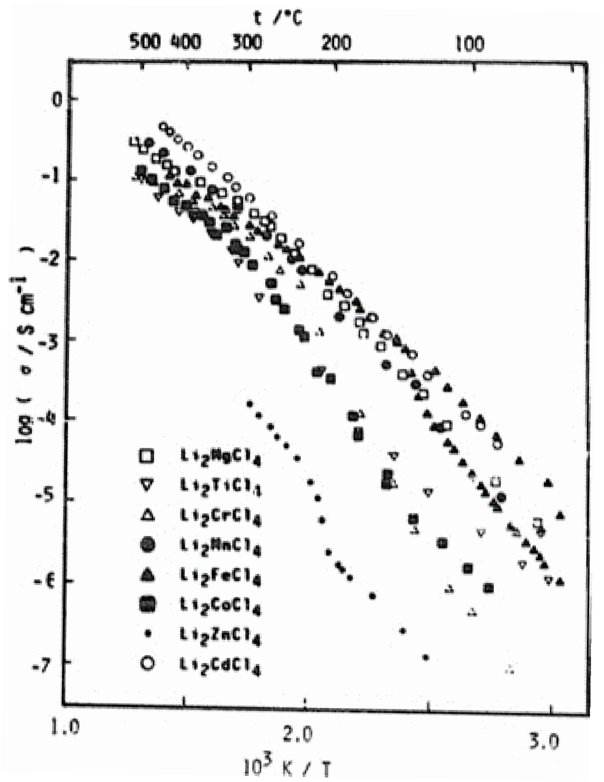

Figure 3-5. Ionic conductivity as a function of temperature of Li_2MCl_4 for M = Mg, Ti, Cr, Mn, Fe, Co, Zn, and Cd.[57]

Activation energies have been calculated for these materials, as seen in Figure 3-6. Given the previously mentioned order-disorder transformation, low and high temperature activation energy values are given. While no straightforward relationship between activation energy and lattice parameters exists, they are certainly dependent.[66] It can be seen that at lower temperatures, the effects of the distorted structure on the activation energy are much more accentuated. More to the point, the activation energy of the distorted Fe is higher than that of the cubic inverse spinel. At higher temperatures, the activation energies are much closer, due to the materials having a cubic spinel structure, as previously mentioned.

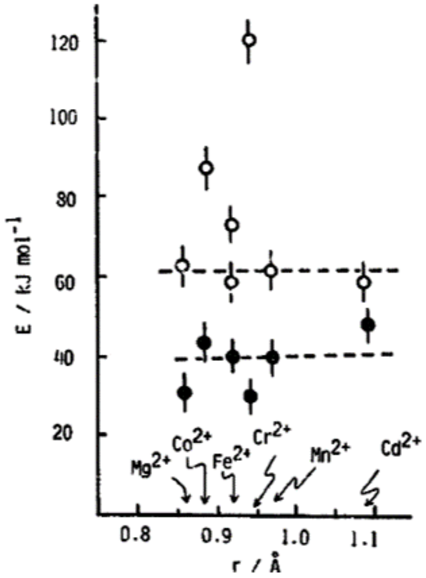

Figure 3-6. Activation energy of Li_2MCl_4 materials as a function of the ionic radii of the divalent metal ions. (○) Activation energy at low temperature (below ~300 °C). (●) Activation energy at high temperatures (above ~300 °C).[57]

Furthermore, since it was determined that vacancy hoping was the primary mechanism for ionic conduction in the spinel structure (V_{Li}’ is the charge carrier, not Li^+), cationic substitution of Li^+ for M^{2+} was done to increase the ionic conductivity.[58,67] Figure 3-7 shows the effect of cationic substitution on the activation energy. Each substitution of a M^{2+} creates V_{Li}’, lowering the activation energy up to a minimum at low temperatures. This proves that the ionic conductivity is dependent on V_{Li}’ rather than Li^+ concentration.

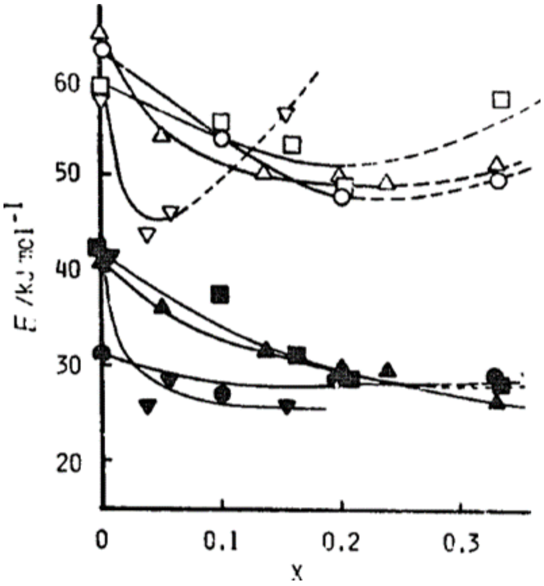

Figure 3-7. Composition dependence of the activation energy of $Li_{2-2x}Mg_{1+x}Cl_4$ (○,●), $Li_{2-2x}Mn_{1+x}Cl_4$ (△,▲), $Li_{2-2x}Fe_{1+x}Cl_4$ (□,■), $Li_{2-2x}Cd_{1+x}Cl_4$ (▽,▼). Open figures represent low temperature, while solid figures represent high temperature.[57]

3.1.4 *Electrolyte Studies for the Li_2MCl_4 System*

As previously mentioned, these materials exhibit high ionic conductivity, some of them, like Li_2FeCl_4 have moderate electrical conductivity due to the presence of Fe^{3+}.[65] Their structure has the aforementioned 3D channels, have high molar lithium content, and elements with low toxicity and high abundance and production, making them attractive as cathode materials from a possible power battery point of view.

The high ionicity of these materials makes them effectively a salt, and therefore very sensitive to moisture and highly soluble.[59,69] Given that an electrolyte is a solvent with a salt dissolved in it, electrochemical characterization of these materials with a liquid electrolyte might prove challenging. Therefore, the electrolyte used to characterize them as cathode materials must be carefully chosen. In order to find an appropriate electrolyte for this family of materials, dissolution experiments were carried out to find a suitable liquid electrolyte. Similarly, polymer based solid electrolytes were fabricated and tested. Lastly, we tied our previous solid electrolyte work to this one by testing LSPS as SE for these materials.

3.2 METHODOLOGY

3.2.1 *Li_2MCl_4 (M=V, Cr, Mn, Fe, and Co) synthesis*

The cathode materials Li_2MCl_4 (M=V (85%, Sigma-Aldrich, USA), Cr (99.99%, Sigma-Aldrich, USA), Mn (99%, ACROS Organics, USA), Fe (99.99%, Sigma-Aldrich,USA), and Co (97%, ACROS Organics, USA)) were prepared by thermal decomposition. The precursors, MCl_2 and LiCl, were mixed in the appropriate stoichiometric proportions using an agate mortar and pressed into a pellet under an argon atmosphere. The pellets were then sealed in evacuated quartz tubes and subsequently heated to 450 °C for a week. These pellets were then ground by hand in an agate mortar and stored in a glovebox for later use.

The samples were also made by mixing stoichiometric amounts of the precursors in a SS ball mill jar with one ½ inch and four ¼ inch stainless steel balls and placed in a high energy ball mill for 5 hours.

3.2.2 *Dissolution Experiments*

In order to find whether the cathode material would be chemically stable in certain solvents, 10 mg of Li_2FeCl_4 were dissolved in 5 mL of solvent. In parallel, solubility experiments were set up for the traditional Li-ion battery electrolyte salts LiBOB (Sigma-Aldrich, USA), $LiPF_6$ (99.99%, Sigma-Aldrich, USA), and $LiAsF_6$ (98%, Sigma-Aldrich, USA). 10 mg was dissolved in

5 mL of solvent. The mixtures were not stirred, and the solvents had been kept in a dry argon environment.

The solvents used were dimethyl carbonate (DMC, (99%, Alfa Aesar, USA)), ethyl methyl carbonate (EMC, (98%, Fisher Scientific, USA)), ethylene carbonate (EC, (99%, Alfa Aesar, USA)) in 1:1 solution with EMC (EC:EMC), propylene carbonate (PC, (99.7%, Sigma-Aldrich, USA)), fluoroethylene carbonate (FEC, (99%, Sigma-Aldrich, USA)), diethyl carbonate (DEC, (99%, Acros Organics, USA)), FEC in 1:1 solution by volume with DEC (FEC:DEC), dioxolane, diglyme, tetrahydrofuran, dichloroethane, acetonitrile, 1-Dichlorobenzene, and N-Methyl-2-pyrrolidone (NMP, (99.5%, Sigma-Aldrich, USA)).

Given that for liquid electrolyte salts, the ones with larger anion radii dissolve more readily due to their delocalized anions.[11] Li_2FeCl_4 was chosen as the material to test first due to its intermediate anion radii among our samples. Anion radii were estimated from the positions given in the Rietveld refinement using VESTA for all the materials, and they were between 0.236 nm and 0.278 nm, with the iron variant being approximately 0.254 nm. Similarly, lithium bis(oxalate)borate (LiBOB) was expected to be the most soluble traditional electrolyte salt due to having one of the largest anion radii, followed by $LiAsF_6$, and $LiPF_6$ having the smallest radii at 0.127 nm. [11]

3.2.3 *Polymer Electrolytes*

The polymer electrolyte materials, consisted of a mixture of polyethylene oxide (PEO, (Sigma-Aldrich, USA)), and various lithium salts in a 65 to 35 molar ratio as follows: 65PEO-35LiX (X = Cl, PF_6, BOB). They were prepared by the solution casting or hot pressing of the precursors. The polyethylene oxide had molecular weights of 1,000,000 or 100,000. For the solution casting process, weighted amounts of the precursors were dissolved in NMP and stirred overnight. They were subsequently cast on polytetrafluoroethylene plates and peeled off. The resulting thickness was of 60-80 µm. For solvent free processing of the polymer electrolytes, the films were cold or hot pressed. For hot pressing, the precursors were first ball milled and then hot pressed into films of 80-100 µm in thickness at 80 °C, like the one seen in Figure 3-8. A similar process was done for cold pressing, without the increase in temperature during the pressing step. The processes were carried out in an argon atmosphere.

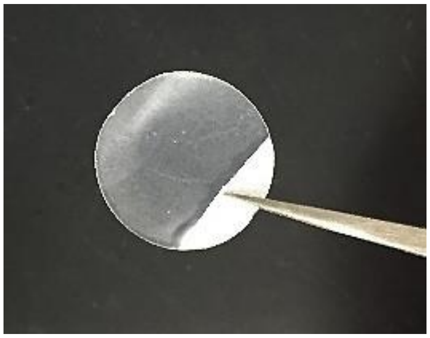

Figure 3-8. Photo of a polymer electrolyte film made by hot pressing after being punched to size.

3.2.4 *Thio-LISICON Electrolyte*

A commercial ceramic electrolyte was also used. $Li_{10}SnP_2S_{12}$ was purchased from NEI Corporation, stored in a glove box, and used as received. This solid electrolyte was chosen due to its compatibility with our intended processing (stable until 500 °C), its nonvolatile non explosive nature (and therefore safety) as well as its reported high lithium ionic conductivity and wide potential window, obtained in our previous work.

3.2.5 *Characterization*

The crystal structure of the materials was investigated through powder X-ray diffraction (XRD, Bruker D8 advance, Germany). The LSPS and LFC powders were first placed in a capillary tube and sealed with wax before exiting the glovebox. The tacky polymers mixtures were placed in a stainless-steel airtight container with either a beryllium or Kapton window, depending on the angles to be analyzed.

3.2.6 *Electrochemical Testing*

The electrochemical properties LFC/LSPS/Li-In ASSBs were investigated using the home-made all-solid-state cells shown in Figure 3-9. Electrode mixtures consisted of LFC powders, carbon black (Alfa Aesar, USA), and LSPS powders in a weight ratio of 66:1:33. They were prepared by hand grinding in a mortar for 30 min. Two-electrode ASSBs were fabricated using ~ 15.3 mg of electrode mixture as the cathode, 80 mg LYC as the separator, and Li-In foil as the anode. The electrode mixture and LSPS were placed in a stainless-steel die with a diameter of 10 mm and pressed together under 500 MPa for 20 min. The cathode/LSPS pellet was then disassembled from the die and placed into the PEEK die with Al foil as current collector on the cathode side. 60 mg of In foil (0.62 V vs. Li^+/Li[41], 99.99%, CMR-Direct, USA) and 10 mg of Li foil (99.9%, MTI Corporation, USA) were placed on the top of the SE and a pressure of 20 MPa was then applied. Li-In electrodes were used to bypass possible side reactions from known issues between the plating and stripping of lithium and solid electrolytes.[3,70] All cell preparation processes were carried in a glovebox. The cells under a 20 MPa pressure were then galvanostatically charged/discharged using a Neware cycler (Neware Battery Testing Instruments, China) in the voltage range of 2.0 to 3.5 V vs. Li-In at 25 °C at 0.1C, which corresponds to 15.3 $\mu A\ g^{-1}$., or 0.195 $mA\ cm^{-2}$.

AC EIS measurements were performed in a potentiostat (Versastat4, Ametek Scientific Instruments, USA). EIS of a PEO electrolyte films was performed at room temperature in a symmetrical cell using carbon foil as the electrodes in the frequency range of 1 - 10^6 Hz and with an amplitude of 5 mV. Cyclic voltammetry (CV) was carried out on LFC/LSPS/Li-In cells at a scanning rate of 10 mV s-1 from 1.0 to 5.0 V.

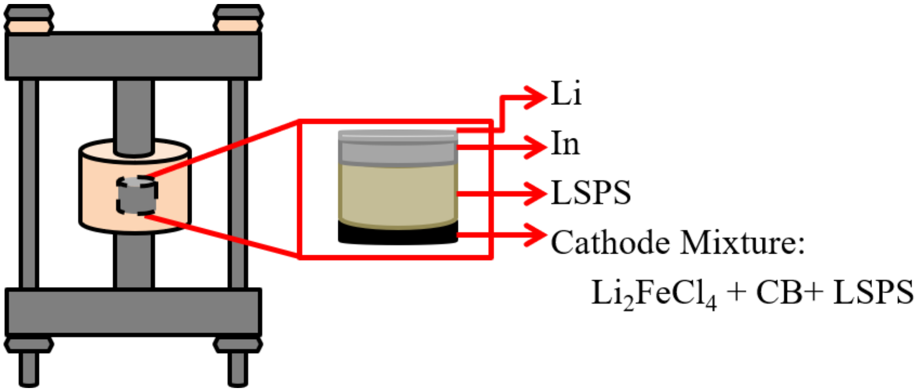

Figure 3-9. Schematic of the architecture of the LFC/LSPS cells tested in this chapter.

3.3 LIQUID ELECTROLYTE AND POLYMER SOLID ELECTROLYTE TESTING

All of the carbonates, the solvents commonly used for Li-ion battery electrolytes, readily dissolved the Li_2FeCl_4 and all of the electrolyte salts, as expected. We continued with the solvents in order of decreasing dielectric constant, but none of them selectively dissolved the traditional electrolyte salts while not dissolving the Li_2 $FeCl_4$.

Similarly, we performed AC electrochemical impedance spectroscopy on the obtained polymer films to determine their ionic conductivity. Unfortunately, regardless of the anion size, salt concentration, molecular weight of the PEO, or synthesis method, the ionic conductivity at room temperature was too small (in the order of 10^{-7} mS/cm), as seen in Figure 3-10.

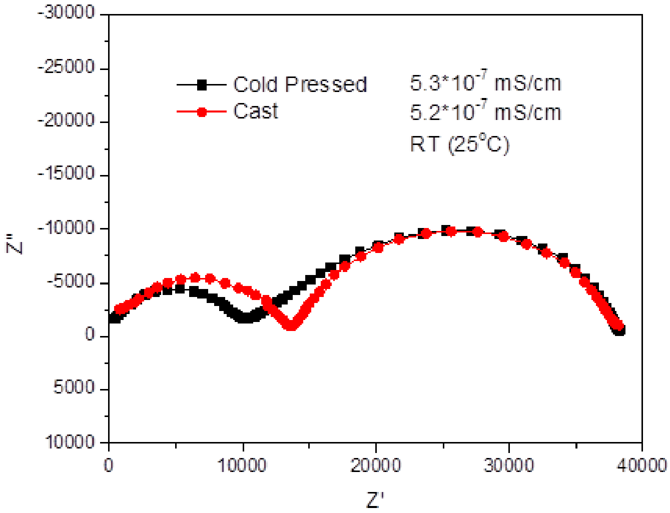

Figure 3-10. Representative Nyquist plot of cold pressed vs. cast polymer films at 25 °C with LiTFSI as salt and PEO with a molecular weight of 1,000,000.

Furthermore, the magnitude of the overall impedance of the half cells increased the polarization to levels outside the testing capabilities of the battery cycler. Additionally, at higher temperatures, the mechanical properties of the films were undesirable for our purposes. At temperatures high enough to have sufficient ionic conductivity, the film was too soft to function as a separator, allowing the cell to short circuit. Similarly, the process of making uniform films of cathode materials through the solvent free method induces changes in the cathode. This can be seen in Figure 3-11, where the XRD peaks corresponding to LFC change depending on which salt was used to make the polymer electrolyte. The red line corresponds to the pattern from PEO+LFC only. The star denotes LFC peaks and it can be seen that the intensity changes when the various salts are added.

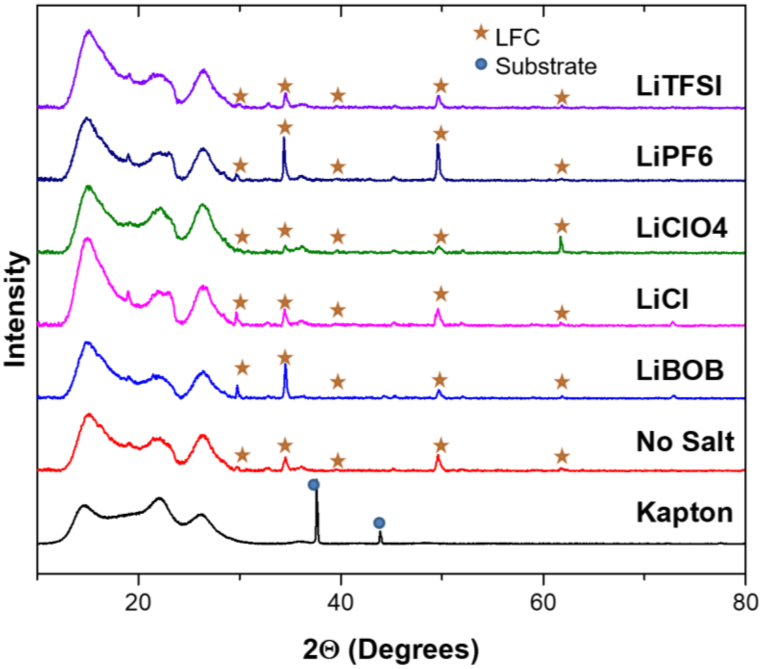

Figure 3-11. XRD of the PEO only through a Kapton window as baseline, PEO plus the LFC sans salts, and PEO with LFC and the various salts.

3.4 SULFUR BASED SOLID ELECTROLYTE TESTING

Having validated our set up and processing of ASSBs with LSPS solid electrolyte in our previous work, as well as bypass some interfacial issues, such as the one from the anode, the next step is to electrochemically characterize our cathode materials using the thio-LISICON SE. The materials were synthesized by solid state reaction and ball milling as detailed in the experimental section. Rietveld refinement was done using the parameters put forth by previous groups.[57,62,67,68] A representative plot for Li_2FeCl_4 is shown in Figure 3-12, where the calculated pattern is in close agreement with the observed pattern suggesting that the structural models match the synthesized materials. The structural characteristics of all samples are shown in Table 3-2, which, as stated before, indicates that our synthesis method produces the Fe, Mn and V containing samples of the spinel structure, and Co and Cr of orthorhombic and monoclinic structures, respectively.

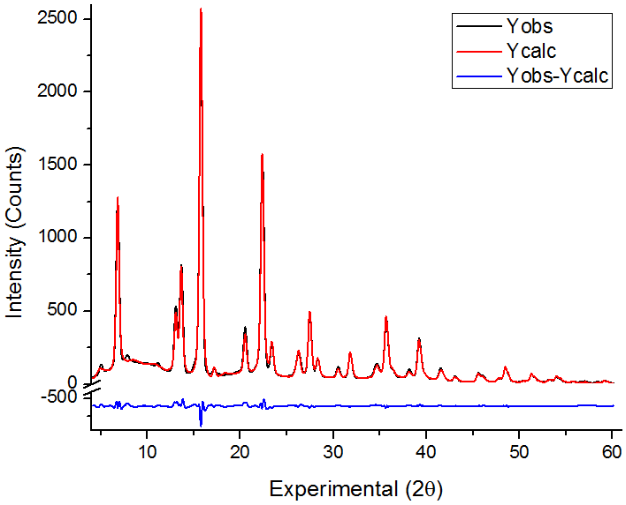

Figure 3-12. Rietveld refinement of the Li_2FeCl_4

Table 3-2. Summary of structure parameters of Li_2MCl_4.

Lithium Transition Metal Chloride	**Space Group**		**Lattice Constant (Å)**			**Cell Angle (^{0})**		
	Number	**Short Name**	**a**	**b**	**c**	**α**	**β**	**γ**
Li_2CoCl_4	74	Imma	7.18	7.24	10.28	90.0	90.0	90.0
Li_2CrCl_4	15	C2/c	10.13	10.19	7.41	90.0	131.9	90.0
Li_2FeCl_4	227	Fd-3m	10.37	10.37	10.37	90.0	90.0	90.0
Li_2MnCl_4	227	Fd-3m	10.49	10.49	10.49	90.0	90.0	90.0
Li_2VCl_4	227	Fd-3m	10.30	10.30	10.30	90.0	90.0	90.0

To verify that the materials could be synthesized by ball milling, XRD patterns were taken after varying intervals of ball milling time. Rietveld refinements on the XRD data showed the reaction was completed after 5 hours for all of the compositions, except for Li_2CrCl_4, which took 7 hours, and Li_2VCl_4. Li_2VCl_4 was the only one whose refinement's fit was not in complete agreement with the literature, in spite of the prolonged reaction time.[67] Inductively coupled plasma (ICP) spectroscopy was done to verify the composition of Li_2VCl_4, and it showed no abnormal amount of impurities and a stoichiometric ratio of 2:1:4. Similarly, the samples synthesized by solid state reaction were verified for completion of reaction at the end of the process; the collection of all XRD patterns is shown in Figure 3-13.

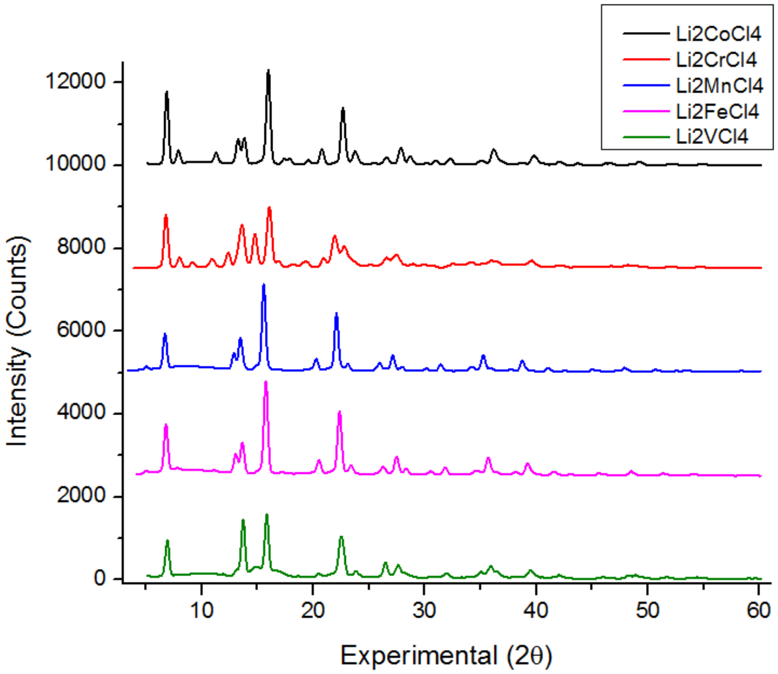

Figure 3-13. XRD patterns of all the synthesized compositions

ASSBs with LFC were fabricated and tested. Figure 3-14a shows the cycling stability. First, LFC shows a charge capacity of ~ 150 mAh/g at C/20 and 60 °C. More importantly, the initial discharge capacity is almost twice the charge capacity at almost 300 mAh/g, and quickly drops to values closer to 225 mAh/g. The first charge reaction is clearly different from the subsequent ones, as seen in Figure 3-14b, from the drop in the charge voltage. The capacity of cells that undergo room temperature aging have significantly lower capacities and undergo an increase and rapid decrease, as seen in Figure 3-15, suggesting the degradation mechanism might involve spontaneous degradation.

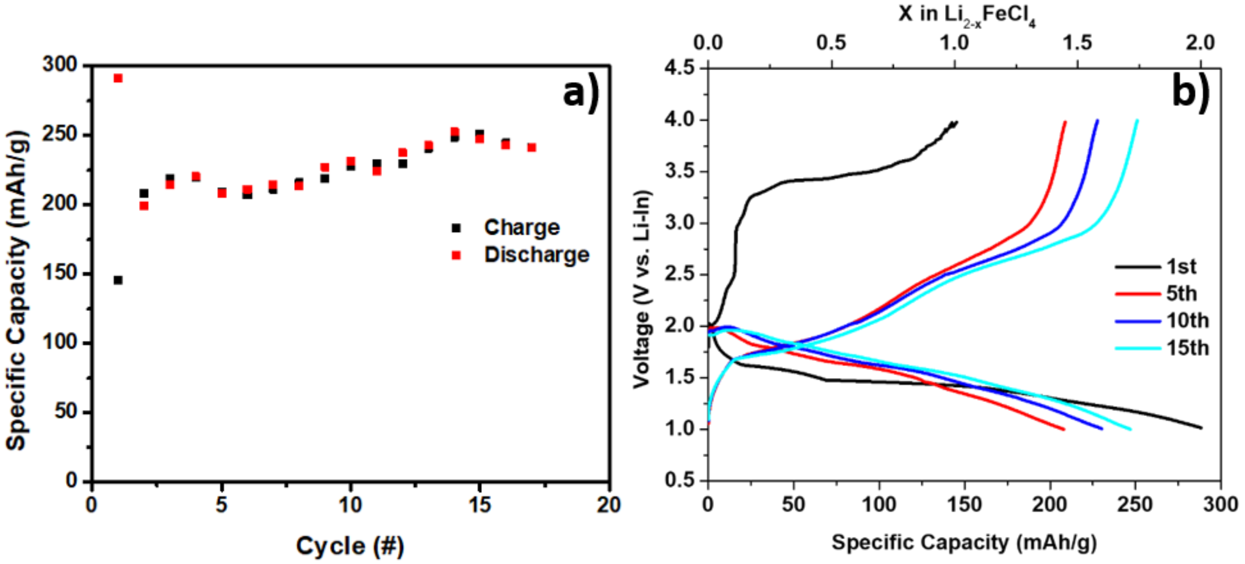

Figure 3-14. Cycling performance of LFC/LSPS/Li-In between 1.0 and 4.0 V vs. Li-In (1.62-4.62 V vs. Li^+/Li) at C/20 and 60 °C (a), and voltage profiles of LFC/LSPS/Li-In cycled between 1.0 and 4.0 V vs. Li-In (1.62-4.62 V vs. Li^+/Li) at C/20 and 60 °C.

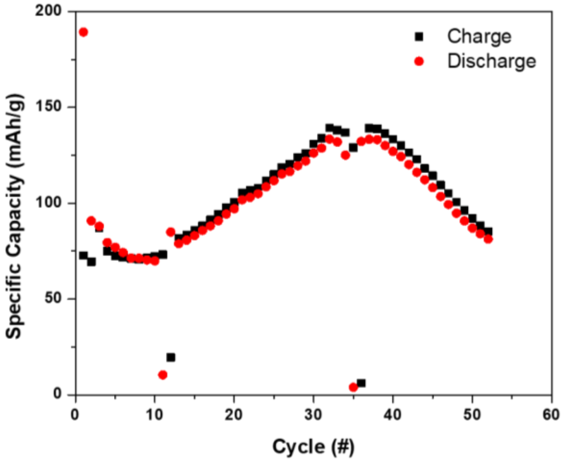

Figure 3-15. Cycling performance of LFC/LSPS/Li-In between 1.0 and 4.0 V vs. Li-In (1.62-4.62 V vs Li^+/Li) at C/20 and 60 °C after resting for a week at room temperature.

This much lower potential is suggestive of a conversion reaction type cathode.[71] To this extent, CV testing was performed. Figure 3-16 shows a rapid decrease in the high voltage cathodic peak and a gradual shift to lower voltages with cycling. A similar, but opposite trend is observed for the anodic peaks, further supporting the possibility of a conversion type reaction.

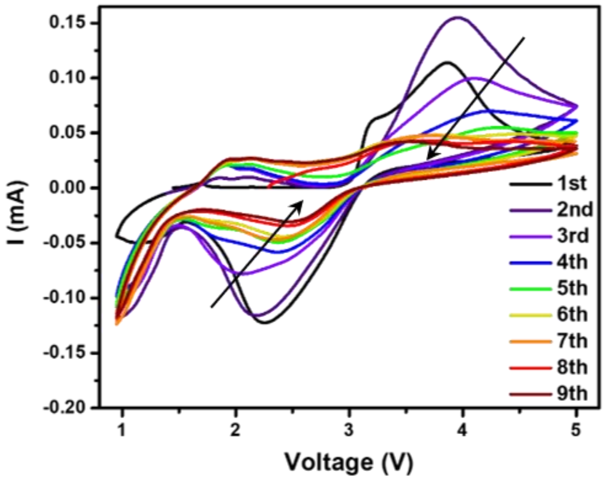

Figure 3-16. Cyclic voltammograms of the LFC/LSPS/Li-In between 0.5 and 5 V vs. Li^+/Li at room temperature.

In order to discern the reaction mechanism taking place, XRD scans were taken. Figure 3-17 shows the XRD scans for the charged and discharged LFC/LSPS/Li-In batteries. It shows that sulfur and iron peaks appear upon lithium extraction, and a new material, Li_2FeS_2 forms upon lithiation. Similarly, there is evidence of a FeS phase being formed.

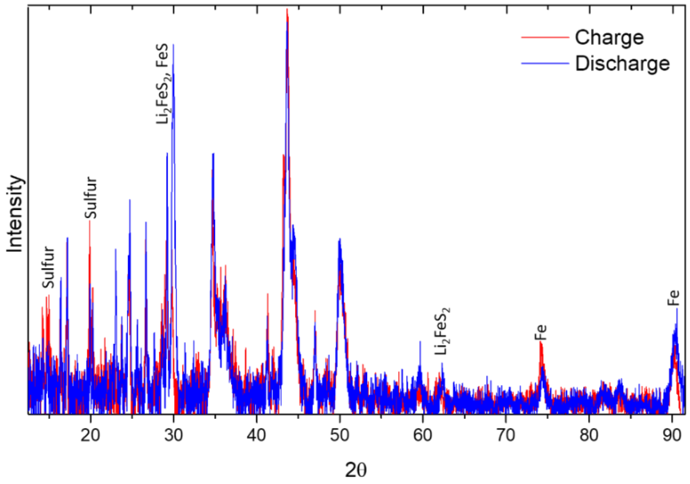

Figure 3-17. Composite data of the powder XRD of LFC/LSPS/Li-In cells after first charge (red) and discharge (blue). A beryllium window was used to obtain the low angle data (below ~30°) and a Kapton window was used to obtain the higher angle data (above ~30°).

The charge-discharge curves are consistent with those found in the literature for the cycling of Fe, FeS and Li_2FeS_2 cathode materials, with a two plateau charge-discharge curve.[69] The formation of Fe metal is traditionally irreversible, as it becomes electrochemically inactive. [69]

3.5 SUMMARY

These highly encouraging new cathode materials Li_2MCl_4 were successfully synthesized, not only by solid state reaction, but also by the cheaper, and easily scalable ball milling method. However, it is not trivial to find an appropriate electrolyte for conducting electrochemical testing of the new cathode materials. The highly ionic lithium metal chlorides, however, make the use of liquid electrolytes impossible due to their high solubility. Similarly, the poor electrochemical and mechanical properties of the tested polymer based solid electrolytes, as well as the cathode material's chemical instability through the processing of polymer-based membranes, makes the use of PEO based SEs impractical. Furthermore, the material adversely reacts with sulfur based solid electrolytes to produce a conversion reaction battery, whose cathode material is presumed to be Li_2FeS_2. In order to use these tested SEs, a coating material to prevent contact between the SE and the cathode must be used, such as the one used in our previous work, or a new, compatible solid electrolyte must be found. Finding a new suitable solid electrolyte would be another promising approach for the viability of these new cathode materials, which will be discussed in the next chapter.

Chapter 4. All Solid-State Batteries with Li_3YCl_6 Electrolyte and Li_2FeCl_4 Cathodes

4.1 INTRODUCTION

4.1.1 *Li_3YCl_6 as a SE*

As previously stated, in order to use SEs, the SE should have an ionic conductivity comparable to that of current liquid electrolytes, e.g., 10^{-3}-10^{-2} S/cm, larger electrochemical windows and compatibility with cathode materials and lithium metal anodes to offset the loss in energy density, larger thermal stability windows, single ion conduction, among others.[50,70,72]

Sulfide based solid electrolytes have so far been the most promising, largely due to their higher ionic conductivities and deformability. These soft mechanical properties bring some appealing qualities, such as intimate contact between grains and no need for heat treatment to create said intimate contact, facilitating their large-scale production.[70,72] However, sulfide based SEs are not compatible with our cathode materials, as discussed in our previous chapter. Halide based solid electrolytes had previously offered ionic conductivities too low to be of interest, but the recent rediscovery of Li_3YCl_6 (LYC), with an outstanding ionic conductivity of 0.5 mS/cm, comparable to that of other electrolytes, has made the use of chloride-based SEs an appealing option for all solid state batteries (ASSBs).[3]

The interest in these materials was renewed due to the high stability of YX_6^{3-} (X = Cl or Br) octahedrons, the fact that each trivalent Y leaves two empty cation sites, and because monovalent Cl ions have weaker interactions with Li^+ than divalent S or O ions do. The additional vacancies and weaker interactions presumably allow for higher ionic conductivities. Furthermore, the large anionic radii provide halide based electrolytes with long ionic bond lengths, high polarizabilities, and therefore high Li^+ mobility and deformability.[3] Therefore, LYC not only has a reasonably high ionic conductivity, it is electrochemically and chemically stable, soft and stable in dry air even at high temperatures.[3]

4.1.2 *Previous Electrochemical Studies on Li_2FeCl_4*

As previously mentioned, electrochemical studies of the Li_2MCl_4 system as cathode materials are greatly limited due to the high iconicity of the material; they readily dissolve into liquid electrolytes.[59,73] Kajiyama et al., and Takada et al. reported some electrochemical data of the Fe containing variation, but those limited studies were performed using quasi static techniques.[59,73] Particularly, Takada et al. only showed the oxidation process of LFC under quasi open circuit voltage corresponding to the extraction of 1.4 Li^+ ions, as shown in Figure 4-1. This extraction had a flat plateau around 3.6V vs. Li^+/Li. It had low active material loading at 49:49:2 and used $0.01Li_3PO_4$-$0.63Li_2S$-$0.36SiS_2$ as the solid electrolyte.

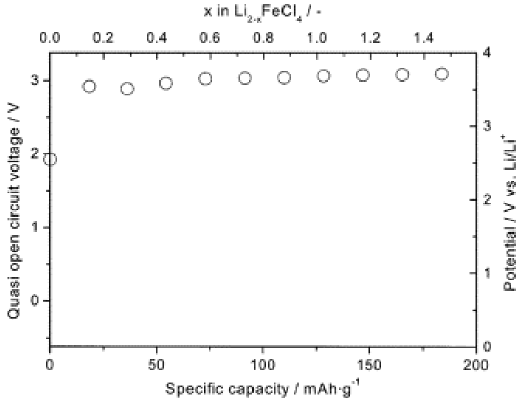

Figure 4-1. Quasi open circuit potential profile of Li_2FeCl_4 during oxidation using $0.01Li_3PO_4$-$0.63Li_2S$-$0.36SiS_2$ glass electrolyte.[69]

Similarly, Kajiyama et al. measured the quasi open circuit voltage of $Li_{1.9}Fe_{1.05}Cl_4$ for the deintercalation of 1.2 Li^+ ions and subsequent intercalation of 1.4 Li^+ ions. Using $0.01Li_3PO_4$-

$0.63Li_2S$-$0.36SiS_2$ glass electrolyte, they were only able to re-intercalate about 0.5 Li^+ at the same potential.[59] They speculated that the flatness of the potential plateau indicated a two phase reaction, rendering the structure unsuitable for reintercalation.[59]

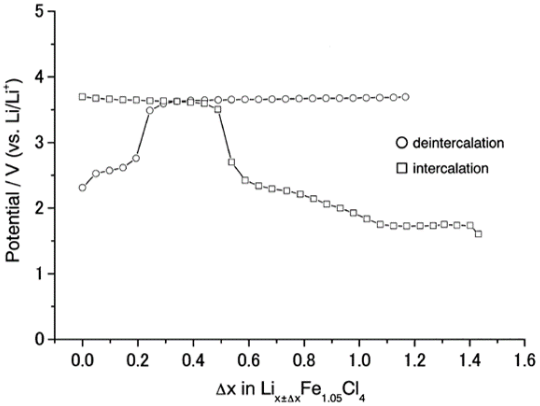

Figure 4-2. Quasi open circuit potential profile of Li_2FeCl_4 during first oxidation and reduction using $0.01Li_3PO_4$-$0.63Li_2S$-$0.36SiS_2$ glass electrolyte.[59]

Neither study shows cycling nor other electrochemical characterization of this family of materials. These materials are of interest, not only because the large amount of lithium per formula unit hints at the possibility of high specific capacities, but also because of their relatively high ionic conductivities. Their ionic conductivities, in the range of 0.01 mS/cm at room temperature, suggest their availability for power applications (vs. $LiCoO_2$ ~ 0.0005 mS/cm, NMC 333 ~ 0.003 mS/cm, NMC 811 ~ 6.3 mS/cm).[74] Similarly, as previously mentioned, its soft mechanical properties might offer an even more intimate contact between the cathode material and solid electrolyte when compared to oxide based cathode materials. Other advantages of the system that have been previously discussed are its cheap, relatively nontoxic components, which while highly hygroscopic like other liquid and sulfide based electrolytes, are not oxygen sensitive.[72] The appeal of pairing LYC and LFC lies in that they are both soft, halide based materials and most of their possible decomposition products are potentially either ionically (LiCl[75]) or electronically ($FeCl_2$[76])

conductive. This would be advantageous over other systems whose interfaces require extensive engineering, most commonly through interfacial modification/coating of the SE or cathode material, or oxide systems which experience cracking or other means of mechanical failure.[33-36,70,72]

4.1.3 *ASSBs with LYC SE and LFC Cathodes*

In order to evaluate the potential of LFC as a new cathode material, ASSBs with LYC SE were fabricated. First, characterization of the components through x-ray diffraction (XRD), AC electrochemical impedance spectroscopy (EIS), and scanning electron microscope (SEM) were performed. The electrochemical performance and interfacial characteristics of the ASSBs using LFC cathode materials and LYC SE were systematically explored by galvanostatic cycling, EIS, energy dispersive X-ray spectroscopy (EDS), among others. Similarly, computational studies to further provide insights into the experimentally obtained data were performed. The study shows that the previously unstudied LFC is a promising candidate as a cathode material, when combined with LYC SE.

4.2 METHODOLOGY

The solid electrolyte was synthesized form the starting materials LiCl (>99%, Alfa Aesar) and YCl_3 (>99.99%, Aldrich). To synthesize the crystalline electrolytes, the precursors were weighted in stoichiometric amounts, hand ground in a mortar, pelletized, sealed in an evacuated quartz tube fitted with a zirconia crucible, and annealed for 5 days at 450 °C. To obtain the hexagonal structure, the ampoule was quenched in an ice bath; to obtain the orthorhombic, the sample was kept at 350 °C for 24 hours prior to quenching in an ice bath. For the ball milled sample, the precursors were placed in a zirconia pot with zirconia balls and milled for 5 hours in 30 min intervals using a SPEX ball mill (SPEX Mixer/Mill 8000M, Spex Sample Prep, USA). The synthesis of the cathode materials was similar to that of the crystalline solid electrolyte; LiCl and $FeCl_2$ (>99.5% BeanTown Chemical) were weighted in stoichiometric amounts, pelletized, sealed into carbon coated quartz tubes, and annealed at 450 °C for 5 days. The cathode material was also synthesized by ball milling, following the same protocol used for the LYC. Given that these materials are highly hygroscopic, these procedures were carried out in an argon filled glovebox (Lab Star, Mbraun, Germany, H_2O < 0.5 ppm, O_2 < 0.5 ppm), and the zirconia pots were sealed in argon prior to being taken out.

The crystal structure of the materials was investigated by powder X-ray diffraction (XRD, Bruker D8 Discover, Germany). The Li_3YCl_6 and Li_2FeCl_4 pellets were firsthand ground in an agate mortar, and placed in a capillary tube sealed with wax before exiting the glovebox for X-ray measurements.

AC EIS measurements were performed in a potentiostat (BioLogic Science Instruments, SP-300, France). EIS of cold-pressed pellets (either LYC or LFC) was performed at various temperatures using an oven (Symphony 414004 – 580 VWR, USA) in a symmetrical cell using carbon foil as the electrodes in the frequency range of 0.1 - 10^6 Hz and with an amplitude of 5 mV.

The electrochemical properties LFC/LYC/Li-In ASSBs were investigated using the home-made all-solid-state cells shown in Figure 4-3. Electrode mixtures consisted of LFC powders, carbon black (Alfa Aesar), and LYC powders in a weight ratio of 66:1:33. They were prepared by hand grinding in a mortar for 30 min. Two-electrode all solid-state cells (ASSCs) were fabricated using ~ 15.3 mg of electrode mixture as the cathode, 80 mg LYC as the separator, and Li-In foil as the anode. The electrode mixture and LYC were placed in a stainless-steel die with a diameter of 10 mm and pressed together under 500 MPa for 20 min. The cathode/LYC pellet was then disassembled from the die and placed into the PEEK die with Al foil as current collector on the cathode side. 60 mg of In foil (0.62 V vs. Li^+/Li,[41] 99.99%, CMR-Direct, USA) and 10 mg of Li foil (99.9%, MTI Corporation, USA) were placed on the top of the SE and a pressure of 20 MPa was then applied. Li-In electrodes were used to bypass possible side reactions from known issues between the plating and stripping of lithium and solid electrolytes.[3,70] All cell preparation processes were carried in a glovebox. The cells under a 20 MPa pressure were then galvanostatically charged/discharged using a Neware cycler (Neware Battery Testing Instruments, China) in the voltage range of 2.0 to 3.5 V vs. Li-In at 25 °C at 0.1C, which corresponds to 15.3 $\mu A\ g^{-1}$., or 0.195 $mA\ cm^{-2}$. For the rate performance measurements all the charging cycles were at 0.1 C, and the discharging current was increased every 5 cycles as follows: 0.1 C → 0.2 C → 0.5 C → 1 C → 2C. Cyclic voltammetry (CV) was carried out at a scanning rate of 0.05 $mV\ s^{-1}$ from 2 to 3.4 V, or 2 to 3.6 V. Similarly, EIS tests of the cells were performed in the frequency range of 0.1-10^6 Hz and an amplitude of 10 mV at various cycling stages.

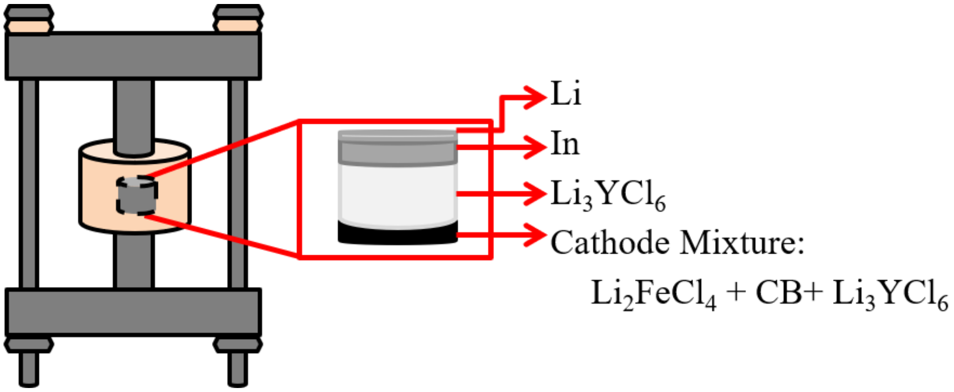

Figure 4-3. Schematic of the architecture of the cells tested in this chapter.

A field emission SEM (FESEM, FEI Sirion XL30, USA) equipped with an Oxford EDS was used to image the particle morphology and obtain elemental analysis and mapping.

All calculations in this work were performed within the generalized gradient approximation (GGA) with the Perdew, Burke and Ernzerhof (PBE) exchange–correlation functional.[77] A planewave basis set and the projector augmented wave (PAW) method[78,79] as implemented in the

Vienna Ab initio Simulation Package (VASP) were used,[80,81] based on the density functional theory (DFT). The Brillouin zone is sampled by using a 2×2×3 Monkhorst–Pack grid[82] for Li_3YCl_6 and a 4×2×4 one for Li_2FeCl_4. The cutoff energy for the plane waves was set to be 520 eV. The total energy was converged to within 10^{-5} eV. The lattice parameters and the ionic position were fully relaxed, and the final force on each atom was less than 0.01 eV/Å.

To study the phase stability and equilibrium charge-discharge curve, we constructed a Li–Y–Cl phase diagram and calculated its electrochemical window using pymatgen.[83] From the phase diagram, one may compute the energy above hull (E_{hull}) of Li_3YCl_6. The E_{hull} of a phase is defined as the normalized energy per atom for that phase above the linear combination of stable equilibrium phases at that composition in the phase diagram. A stable compound has an E_{hull} of 0, and the higher the E_{hull}, the more unstable the compound is likely to be. Apart from the compounds of Li_3YCl_6 and Li_2FeCl_4 in this work, the energies of existing equilibrium phases were extracted from Materials Project (MP) database[42] using the Materials Application Programming Interface (API).[84]

4.3 RESULTS AND DISCUSSION

4.3.1 *Characterization of the Solid Electrolyte and Cathode Materials*

Figure 4-4a shows the crystal structure of the hexagonal, orthorhombic, and ball milled LYC. The LYC sample quenched at 450 °C crystalizes in a hexagonal structure with a space group $P\bar{3}m1$, closely matching the PDF 04-009-8882,[85] with lattice parameters of a = 11.1976 Å and c = 6.0395 Å. The calculated pattern closely matches that of the experimental data, as well as the XRD data presented by Asano et al. as the high crystallinity sample.[3] The divergence between the calculated and experimental plots is attributable to the presence of the low temperature phase in the synthesized sample, as the high temperature phase is metastable at room temperature and will completely transform to the orthorhombic low temperature phase when annealed above 210 °C.[85] The LYC sample quenched at 350 °C crystalizes in an orthorhombic structure, space group Pnma, with lattice parameters of a = 12.9184 Å, b = 11.2129 Å, and c = 6.0388 Å. The calculated pattern closely matches that of PDF 04-009-8886.[85] As expected, the ball milled sample has much lower crystallinity, making fitting calculations less reliable, and therefore imprecise to ascribe to either phase. An amorphous hump is seen at lower angles, but it is otherwise clear that the material belongs to the same family of phases of the crystalline counterparts. It has been speculated that ball milling introduces disorder in the distribution of Y.[3]

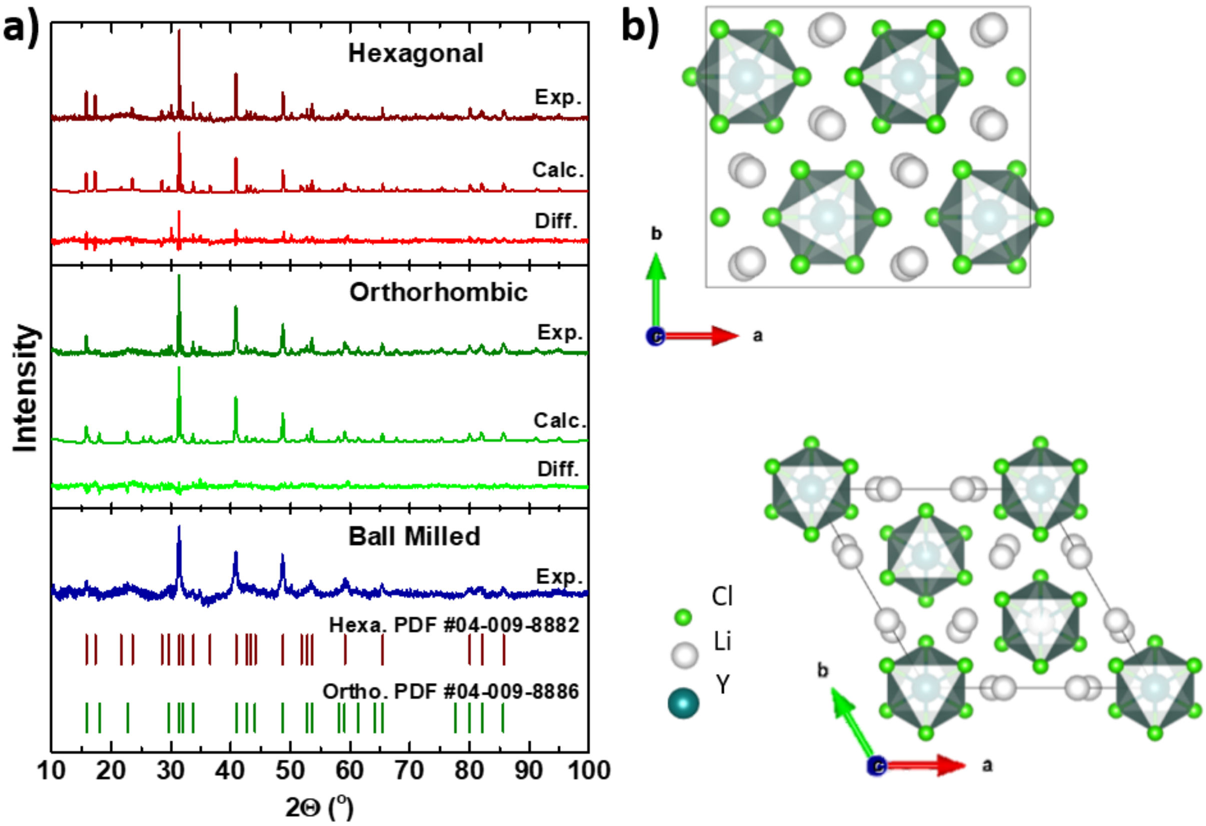

Figure 4-4. (a) Experimental and simulated powder X-ray diffraction (XRD) of the hexagonal (top), orthorhombic (middle), and ball milled (bottom) LYC powders at room

temperature. (b) Crystal structure of the hexagonal (bottom right) and orthorhombic (top right) LYC. [YCl_6] (turquoise) octahedra are shown.

The structures of both phases are related in that they are primarily composed of a hexagonal close packed arrangement of chloride ions with the cations partially occupying two thirds of the octahedral spaces,[3] as seen in Figure 4-4 b. Both structures feature a three-dimensional percolating arrangement of the lithium ions, ensuring pathways for high ionic conductivities through the octahedral sites via tetrahedral sites along the a-b plane and octahedral to octahedral along the c axis, as established by Asano et al. and Bohnsack et al.[3,85] The tetrahedral positions are partially blocked due to the repulsive Coulombic interactions between Y^{3+} and Li^{+}. Furthermore, one third of the cation sites are vacant, which is important, as the primary conduction mechanism is V_{Li}', and it is speculated that the relaxed crystallinity and increased disorder of the cations reduces the Coulombic blocking.[3]

The inset in Figure 4-5 shows a representative Nyquist plot of the EIS measurement at 25 °C. The samples were cold pressed powders, with no further heat treatment. The data was well fitted to the equivalent circuit shown in Figure 4-6. There is a high frequency semicircle, attributed to the grain boundary impedance, which is smaller on the orthorhombic phase, and not visible on the ball milled sample. The total ionic conductivities are summarized in Table 4-1. At 25 °C, the values of the hexagonal, orthorhombic and ball milled sample are of 0.05, 0.10, and 0.46 mS/cm respectively. Similarly, from the Arrhenius plot in Figure 4-5 it can be seen that the activation energies are of 0.43, 0.40, and 0.30 eV each. These values are similar to those reported by Asano et al. indicating our solid electrolyte is consistent with that reported in the literature.[3] The observed decrease in activation energy is consistent with the expansion of the lattice parameters.[85] The expansion of the lattice parameters allows for a less tightly packed unit cell, leading to broader diffusion pathways for Li$^+$ conduction.[86]

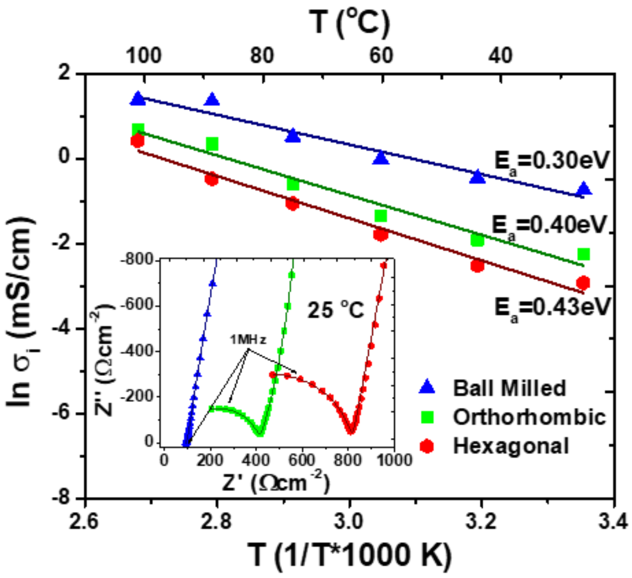

Figure 4-5. Arrhenius and Nyquist (inset) plot of the hexagonal (red hexagon), orthorhombic (green square), and ball milled (blue triangle) pellets of LYC in C/LSPS/C cells at various temperatures.

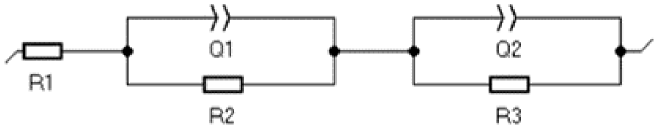

Figure 4-6. Equivalent circuit used to fit the LYC and LFC cold pressed pellets. R1 is the bulk resistance; R2 the grain boundary resistance, and R3 is the charge transfer resistance. Q1 and Q2 are the accompanying CPEs.

Table 4-1. Summary of the ionic conductivities of LYC as a function of temperature, including the high temperature hexagonal phase, low temperature orthorhombic phase and the ball milled sample.

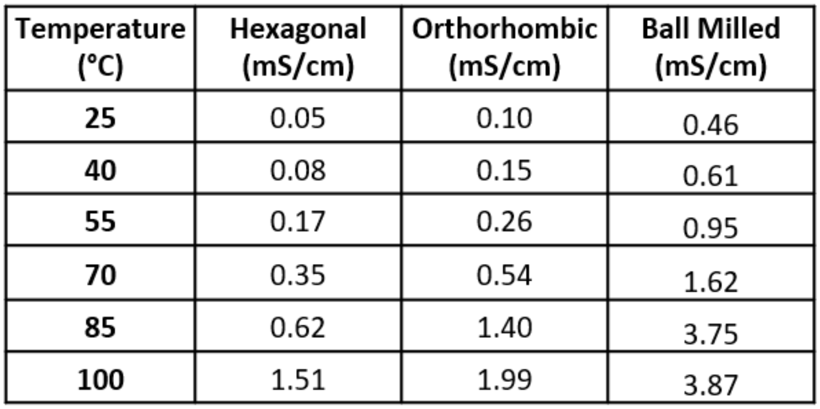

Temperature (°C)	Hexagonal (mS/cm)	Orthorhombic (mS/cm)	Ball Milled (mS/cm)
25	0.05	0.10	0.46
40	0.08	0.15	0.61
55	0.17	0.26	0.95
70	0.35	0.54	1.62
85	0.62	1.40	3.75
100	1.51	1.99	3.87

Ball milled LYC, having the cheapest processing conditions and exhibiting the highest ionic conductivity, was chosen as the best candidate for ASSBs. All the cell data shown were obtained using ball milled LYC as the solid electrolyte. SEM images were obtained in order to see the morphology of the material; as shown in Figure 4-7. The ball milled LYC exhibited an easily agglomerated granular shape, with a primary particle size distribution between 1-10 µm, and a secondary particle size below the micron range.

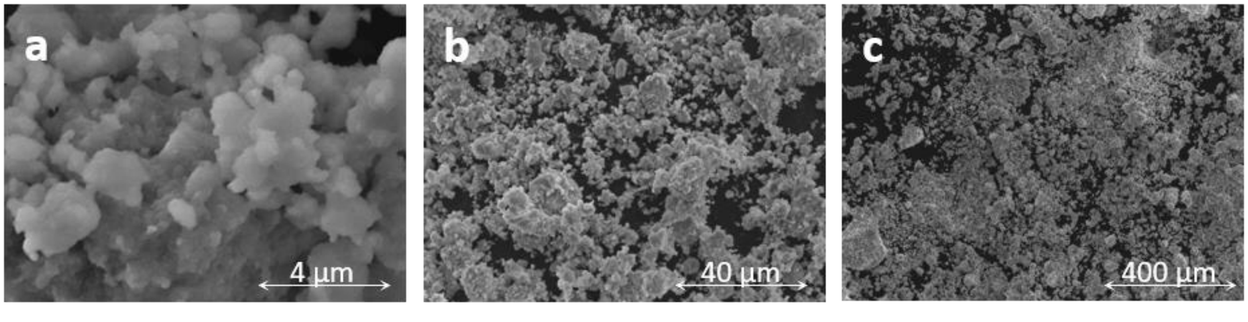

Figure 4-7. Scanning electron microscopy image of the ball milled LYC at (a) 10000, (b) 1000, and (c) 100 magnification.

Figure 4-8a shows the XRD pattern of the LFC cathode material. It closely matches PDF 00-036-1384.[58] When quenched, it crystallizes with a cubic structure, space group Fd$\bar{3}$m, with lattice parameters of a = 10.3973 Å, as suggested by Van Loon et al.[87] The structure has 3D channels that allow for the quick diffusion of lithium ions, as seen in Figure 4-8b. It is a face centered inverse spinel, where half of the lithium resides in the tetrahedral position, while the other half and the iron occupy octahedral positions.[57,58,62,65-67]

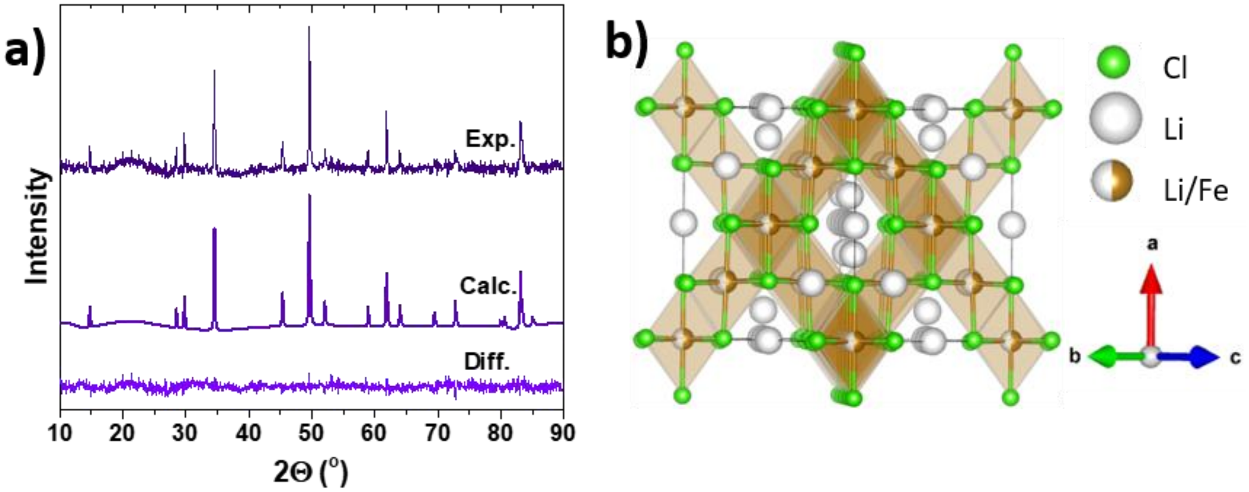

Figure 4-8. (a) Experimental and simulated powder X-ray diffraction (XRD) of the LFC powders. (b) Crystal structure of the cubic LFC. [$FeCl_6$] (orange) octahedra are shown.

Figure 4-9a shows Nyquist plots of the EIS measurement of LFC at various temperatures. The samples were cold pressed powders, with no heat treatment. As done with the LYC samples, the data was well fitted to the equivalent circuit previously shown. There is a high frequency semicircle, attributed to the grain boundary impedance which, as expected, is reduced with increasing temperature. The total ionic conductivities are summarized in Table 4-2. At 25 °C, the value of the ionic conductivity is of 0.01 mS/cm, consistent with those reported by the literature.[58,62,66] The frequency at which this semicircle occurs indicates that intergranular capacitance rather than intergranular impedance is the limiting factor. Similarly, previous work by Kanno et al. suggests that an increase in Li^+ vacancies increase the ionic conductivity.[66] From the Arrhenius plot in Figure 4-9b it can be seen that the activation energy is of 0.45 eV. SEM images were obtained in order to see the morphology of the material; they exhibited an easily agglomerated granular shape, with a primary particle size distribution between 1-10 µm, and a secondary particle size below the micron range, as seen in Figure 4-10 a - c.

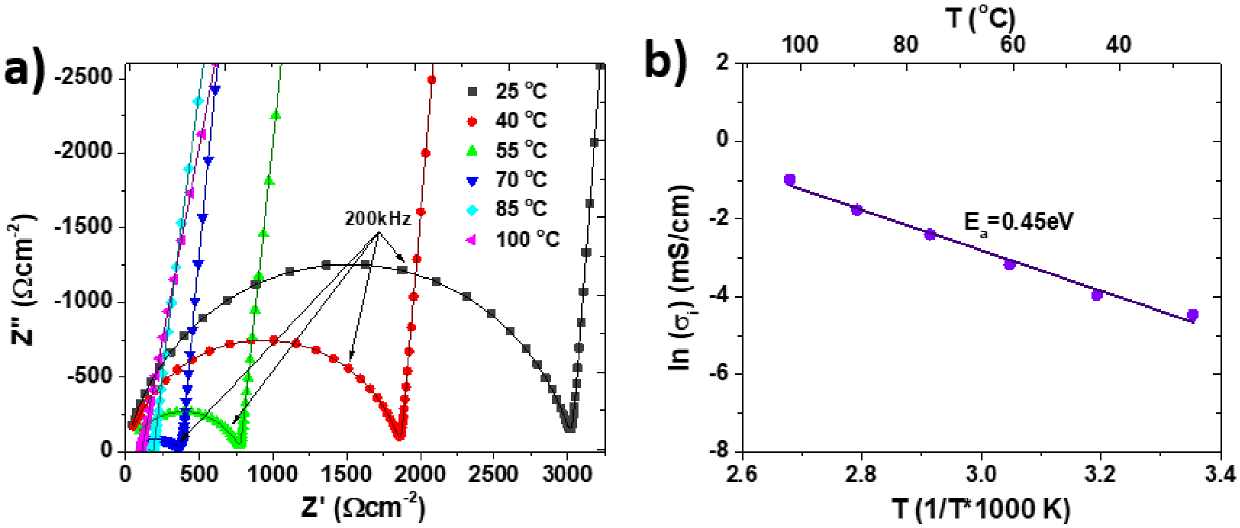

Figure 4-9. (a) Nyquist plot of LFC pellets in a C/LSPS/C cell at various temperatures. (b) Arrhenius plot of the ionic conductivity LFC.

Table 4-2. Summary of the ionic conductivities of LFC as a function of temperature.

T	σ_i
(°C)	**(mS/cm)**
25	0.012
40	0.020
55	0.044
70	0.094
85	0.180
100	0.376

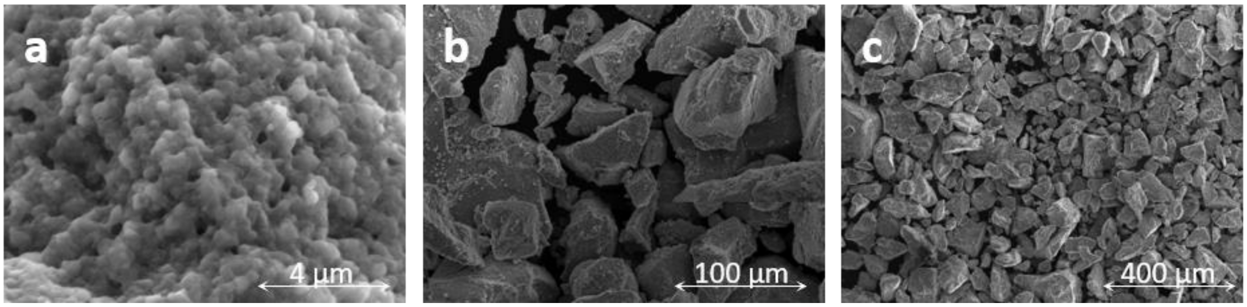

Figure 4-10. Scanning electron microscopy image of the LFC at (a) 10000, (b) 500, and (c) 100 magnification.

4.3.2 *Electrochemical Performance of the All-Solid-State Cells*

After characterizing the synthesized LYC electrolyte and LFC cathode powders, ASSBs were fabricated and tested in order to study the electrochemical performance of the cathode material and its compatibility with LYC. The upper voltage cut off was chosen based on the results of CV testing shown in Figure 4-11. Figure 4-11 shows that cycling below 3.4 V is highly reversible; however, opening the voltage window to 3.6 V, although it provides more capacity, it also seems to cause faster degradation in the cycling performance. For those reasons, the cycling was limited to the extraction of 1 Li^+, or 3.5 V, at a C/10 rate.

Figure 4-12 shows the cycling performance of the LFC at a C/10 rate, or 0.195 mA/cm^2. They indicate a first charge capacity of ~ 130 mAh/g at C/10 and 25 °C, a value similar to that reported by Takada et al. using quasi static open circuit voltage testing,[24] which corresponds with the extraction of a little more than 1 Li^+ and a discharge capacity of about 118 mAh/g, giving an initial Coulombic efficiency loss of 8.4%. While this initial Coulombic efficiency loss is significantly larger than that of cells with liquid electrolytes, it is comparable to that reported by Asano et al.,[3] and similar to that reported for some sulfur based solid electrolytes.[8] The capacity retention of this LFC/LYC/In-Li cell is considerable, as it didn't reach 80% of initial capacity until its 180th cycle.

More importantly, the overpotential of the cell was of 130 mV in the first cycle, which gradually decreased by about 13% by the fifth cycle, as seen and calculated in Figure 4-13. The overpotential then very slowly increases, not reaching its original value until around the 150th cycle. This is in contrast to most ASSB systems in which a coating layer is required on the cathode to mitigate the often dramatic and severely damaging increase of impedances as the cell cycles.[27,34,88]

EIS studies were performed to further look into the impedance of the cell, more on this in later sections. The reduction of overpotential, but the overall loss of capacity suggests that the primary failure mechanism in early cycles is loss of active material.[70,72] This loss of active material could be through loss of electrical contact, degradation of the cathode crystalline structure, among others.[70,72]

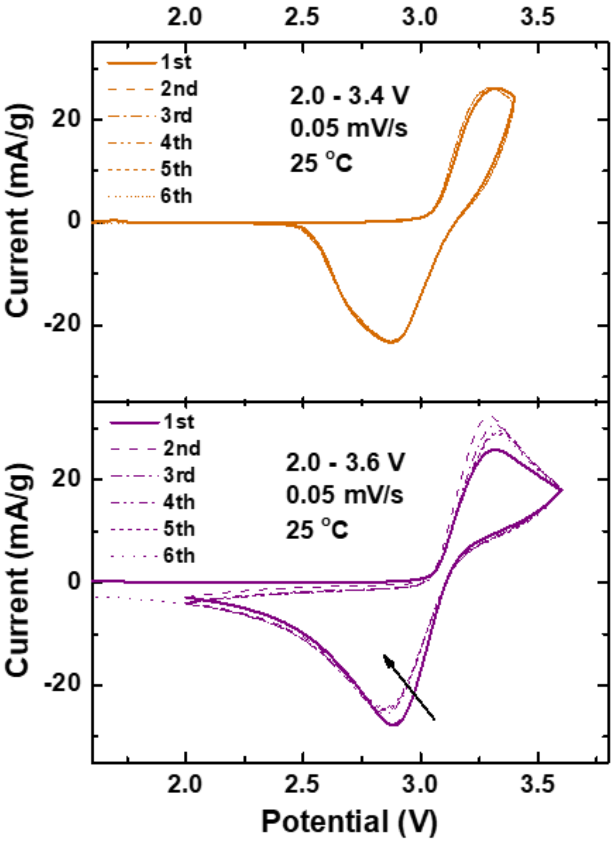

Figure 4-11. Cyclic voltammograms of the LFC/LYC/Li-In between (top) 2 to 3.4 V and (bottom) 2 to 3.6 V at 25 °C.

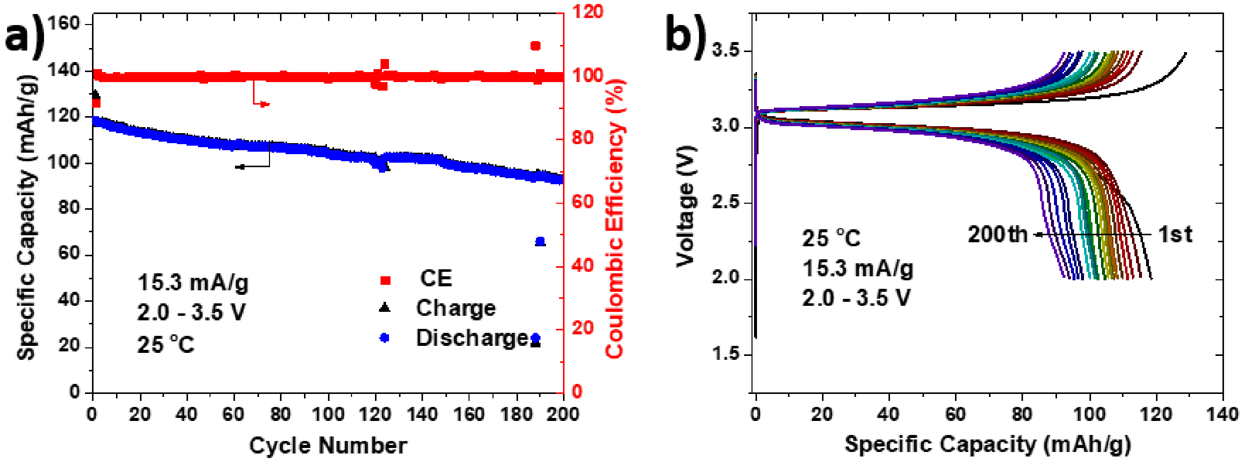

Figure 4-12. (a) Cycling performance and Coulombic efficiency of LFC/BM-LYC/Li-In between 2.0 and 3.5 V vs. Li-In (2.62-4.12 V vs. Li^+/Li) at C/10 (0.195 mA/cm^2) and 25 °C. (b) Voltage profiles of the LFC/BM-LYC/Li-In cell in (a); only every 10^{th} cycle is shown.

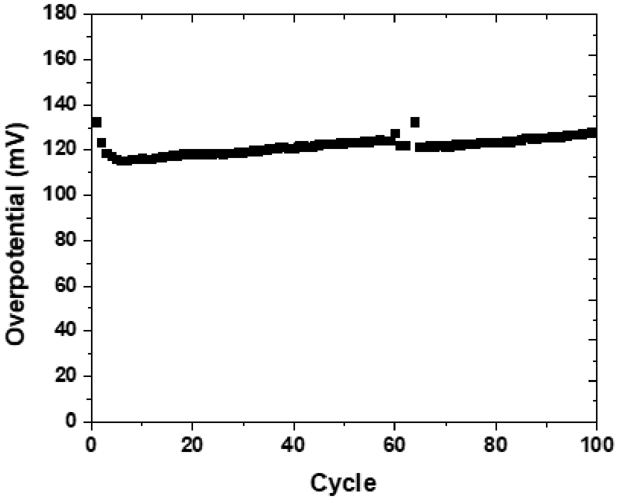

Figure 4-13. Overpotential as a function of cycle. The overpotential was calculated as the energy divided by the capacity.

Figure 4-14 shows the rate capability of the LFC at a constant charge rate of C/10, and various discharge rates. LFC is able to deliver 114 mAh/g on average for the 5 cycles, at a rate of C/10. At C/5, C/3, 1C, and 2C it is able to deliver on average 96, 91, 65, and 30% of the initial specific discharge capacity, respectively. There is little decay in the capacity at rates below C/3 indicating good compatibility between the SE and the cathode, while the discharge capacity sees considerable deterioration at higher rates. In addition, the LFC cell exhibits 100 mAh/g discharge capacity when cycled at C/10 again.

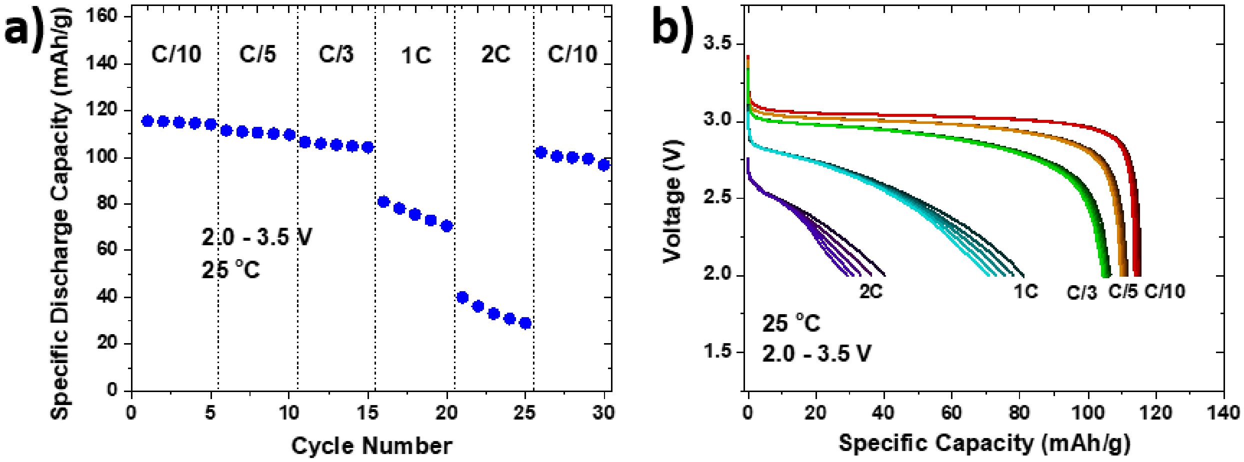

Figure 4-14. (a) Specific discharge capacity as a function of cycle of LFC/BM-LYC/Li-In between 2.0 and 3.5 V vs. Li-In (2.62 - 4.12 V vs. Li^+/Li) at 25 °C with a fixed charge rate of C/10 at various discharge rates. (b) Voltage profiles of the LFC/BM-LYC/Li-In cell in (a).

4.3.3 *Electrochemical Impedance Spectroscopy Study*

To shed more light into the overpotential, and to further characterize this new system, EIS studies were performed. Figure 4-15a depicts the Nyquist plots of the LFC cells after the first cycle. The Nyquist plots could be well fitted by the equivalent circuit shown in the inset of Figure 4a, which contains the serial combination of electrolyte resistance R_{SE} (high frequency intercept with real axis), resistance from the grain boundaries in the electrolyte R_{HF} (high frequency semicircle, ~1 MHz), resistance between the solid electrolyte and the cathode material R_{MF} (middle frequency semicircle, ~20 kHz), and resistance between the solid electrolyte and the anode material R_{LF} (low frequency semicircle, ~20 Hz), as well as the respective constant phase elements (CPE) associated with the resistances.[33-36] The fitting results are summarized in Figure 4-15b.

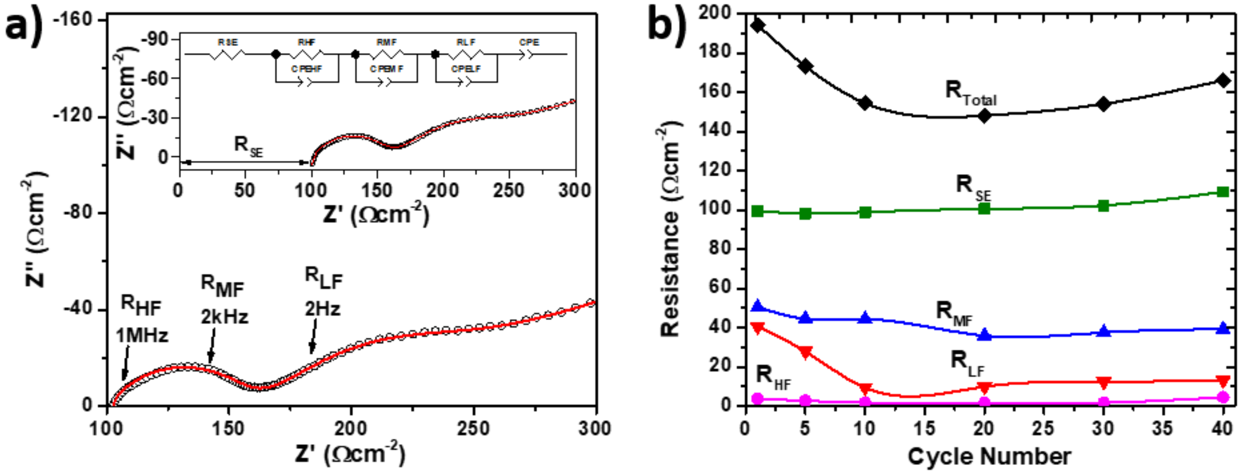

Figure 4-15. (a) Sample room temperature Nyquist plots of a LFC/BM-LYC/Li-In cell after the first cycle and the equivalent circuit used to fit the data (inset) (b) Summary of resistances as a function of cycle derived from the EIS fitting.

The electrolyte resistance, R_{SE} starts at 100 Ωcm^{-2}, consistent with the data obtained for the solid electrolyte presented in Figure 4-5, comprising most of the total resistance. The resistance from the solid electrolyte slowly increases by about 10% in the first 50 cycles, accounting for most of the increase in impedance. The grain boundary resistance, R_{HF}, is the smallest contribution to the total resistance, with an initial value of almost 4 Ωcm^{-2}. It initially decreases, but then gradually increases, regaining its original value after 50 cycles. The resistance between the solid electrolyte and the cathode, R_{MF}, originally at 50 Ωcm^{-2}, decreases by almost a third in the first 20 cycles. This is possibly due to the activation of cathode material particles, or the formation of a beneficial interphase layer.[34,36,48,49,52,88] Computational studies were carried out to further look into the interphase formation. The biggest drop in resistance comes from the solid electrolyte/anode component, R_{LF}. This resistance starts at 40 Ωcm^{-2}, and subsequently drops by three fourths of its original value within the first 10 cycles, suggesting an improvement in the interphase between the solid electrolyte and the Li-In, most likely an improvement in the contact through repeated cycling.[70] It has been shown that the exchange current density increases with cycling due to the increase of active lithium surface electrode area, as well as a stripping of the native SEI, which improves the charge transfer process at the anode.[89] Like all the other resistances, this one then slowly increases, contributing to the increase in total resistance of the cell.

4.3.4 *Computational Studies of LFC/LYC Interfaces*

To further corroborate the experimental data, computational studies were conducted. The hull energy of LYC is of only 0.007 and 0.010 eV/atom for the orthorhombic and hexagonal phases, respectively. This means that they are both technically metastable phases, but unlikely to decompose; by comparison, LLZO has a hull energy of 0.007 eV/atom, LLTO of 0.02 eV/atom, and LGPS of 0.03 eV/atom,[42] as seen in Figure 4-16 and summarized in Table 4-3. The electrochemical stability window of the LYC solid-state electrolyte was calculated, and the results are shown in Figure 4-17. The materials display a large voltage window of 3.59 V from 0.62 V to 4.21 V vs. Li^+/Li, closely matching the experimental results obtained by Asano et al.[3] Below the stability window, it presumably would decompose into Y_2Cl_3 and LiCl, and above it, into YCl_3, Cl_2. This thermodynamic voltage window is comparable to that of some oxide based electrolytes, such as LLZO , but significantly larger than most sulfide based solid electrolytes, such as LGPS, as seen in Figure 4-16.[30] Furthermore, the calculated thermodynamic oxidation potential seems to be higher than that of most electrolytes of interest,[30] making it preferable for high voltage cathode applications. The data of the thermodynamically calculated properties of the SEs used to compare has been summarized in Table 4-3.

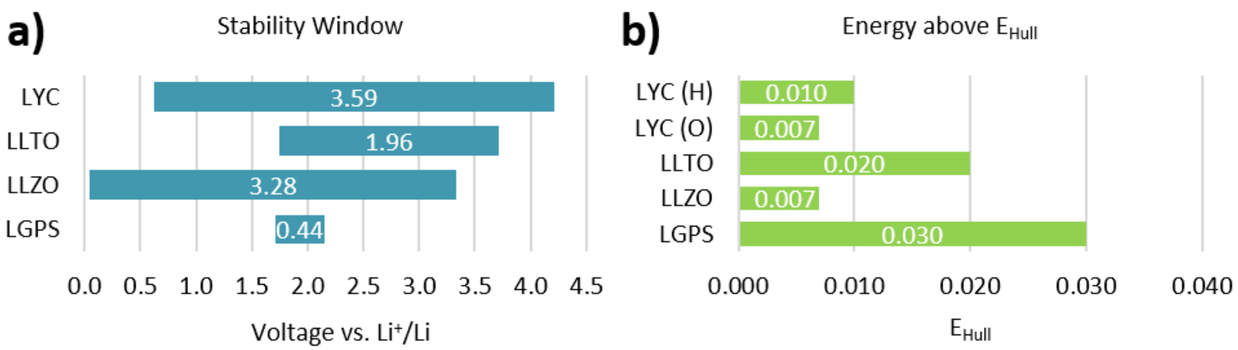

Figure 4-16. (a) Stability window and (b) Hull energy of various SEs.

Table 4-3. Summary of various calculated thermodynamic properties.

	E_{Hull}	**Reduction Potential**	**Oxidation Potential**	**Voltage Window**
	(eV/atom)	**(V vs Li^+/Li)**	**(V vs Li^+/Li)**	**(V)**
LGPS	0.030[42]	1.71[30]	2.15[30]	0.44
LLZO	0.007[42]	0.05[30]	3.33[30]	3.28
LLTO	0.020[42]	1.75[30]	3.71[30]	1.96
LYC	0.007 (O)	0.62	4.21	3.59
	0.010 (H)			

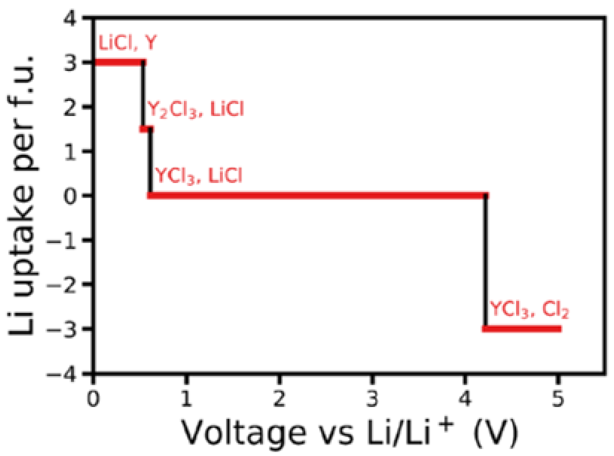

Figure 4-17. Calculated stability window of the LYC.

Finally, the stability of the LYC SE vs. the LFC cathode was calculated. A complete list of the predicted product reaction phases is provided in Table 4-4. The only thermodynamically favorable decomposition reaction gives $FeCl_2$, LiCl, and YCl_3 as the products, with a Gibbs free energy of -1.5 eV. The equation for the decomposition reaction is

$$Li_2FeCl_4 + Li_3YCl_6 \rightarrow FeCl_2 + YCl_3 + 5LiCl.$$

Given that the oxidation potential of the LYC electrolyte is outside of the testing window, and that the possible decomposition products are either highly electrically conductive ($FeCl_2$),[76] or ionically conductive (LiCl),[75] we speculate that if an interphase layer does form, it is not detrimental to the overall impedance of the cell, as indicated by the EIS data.

Table 4-4. All the possible calculated decomposition reactions at the LFC/LYC interface.

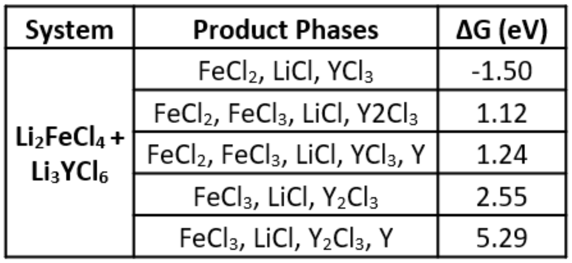

System	Product Phases	ΔG (eV)
Li_2FeCl_4 + Li_3YCl_6	$FeCl_2$, LiCl, YCl_3	-1.50
	$FeCl_2$, $FeCl_3$, LiCl, Y2Cl_3	1.12
	$FeCl_2$, $FeCl_3$, LiCl, YCl_3, Y	1.24
	$FeCl_3$, LiCl, Y_2Cl_3	2.55
	$FeCl_3$, LiCl, Y_2Cl_3, Y	5.29

4.4 SUMMARY

All solid-state batteries with Li_2FeCl_4 cathodes, Li_3YCl_6 solid electrolyte, and Li-In anodes were fabricated to evaluate the electrochemical performance of low-cost Li_2FeCl_4 cathodes and its interfacial behavior with Li_3YCl_6 solid electrolytes. Good cycling stability and rate capability can be observed for the cells, primarily due to the stability of the LFC/LYC interface. The electrochemical properties of LFC are finally studied obtaining discharge capacities close to the theoretical when cycled at a C/10 rate, or 0.195 mA/cm^2 at 25 °C. LFC maintained a discharge capacity of more than 80% its initial value until its 180th cycle. EIS studies showed that the most significant contributor to the overall impedance was the solid electrolyte layer, followed by the interphase between the cathode and the solid electrolyte. Computational studies were carried out to provide an insight into the possible composition of an interphase layer. It was determined that if an interphase layer does form, it is likely to be composed of either ionically (LiCl), or electrically conductive ($FeCl_2$) compounds, and therefore, not detrimental to the impedance of the cell.

In addition to this, the ionic conductivity of the LYC solid electrolyte was studied as it changes with crystal structure. Its ionic conductivity increases with an increase of the lattice parameters of the structure (ball milled > orthorhombic > hexagonal), as expected. The biggest challenge for the system in this particular set up corresponds to the thick layer of solid electrolyte. Future research should involve determining the effect of ball milling synthesis of the cathode material as far as particle size, ionic conductivity, and cycling are concerned. We speculate the reduced particle size will help mitigate the loss of cathode material, which was the largest contributor to capacity loss. Similarly, given the high ionic conductivity of the cathode material, an interesting direction would be exploring its use for thick cathode AASBs. In short, this cheap, relatively non-toxic and scalable system with highly ionic conductive halide-based materials is promising for ASSBs.

Chapter 5. CONCLUSION AND OUTLOOK

The most pertinent results from our all solid-state battery work, as they relate to interphase engineering and judicious SE selection, have been presented in this thesis. Given that a summary of the scientific findings has been presented at the end of each chapter, here we will summarize the most important aspects of the work.

5.1 SUMMARY BY CHAPTER

5.1.1 *Summary of Chapter 1 - Introduction*

In Chapter 1 the motivation and purpose of this work were discussed. A focus on the definitions of various battery properties, types and design parameters by applications, as well as advantages and challenges of all solid-state batteries was given.

5.1.2 *Summary of Chapter 2 - ASSBs with $Li_{10}SnP_2S_{12}$ Electrolyte and $LiCoO_2$ cathodes*

All solid-state batteries with a well-studied cathode material and an untested SE were assembled to:

(1) Authenticate the newly acquired ASSB testing capability of our lab. Like most battery labs our testing capabilities were limited to architectures and chemistries compatible with coin cell testing. Multiple devices and processes had to be designed and built, or adapted, in order to enable ASSB research in our facilities.

(2) Determine the feasibility of $Li_{10}SnP_2S_{12}$ as a solid electrolyte. While extensive computational and experimental research has been done on the properties of LSPS itself, no experimental data existed on it in cells, despite it being commercially available.

(3) The importance and effects of engineering the interphase were highlighted.

5.1.3 *Summary of Chapter 3 - Electrolyte Selection for Li_2MCl_4 Cathodes*

We have a strong belief in the importance of communicating negative results, in addition to successful results, as the most efficient and quick way to increase our knowledge base. Therefore, a chapter with “unsuccessful”, yet insightful attempts was included. It is our hope that this will reduce wasted efforts, and perhaps give clear directions, were someone to pursue these lines of research. To this end we included the following knowledge in this chapter:

(1) The cathode material, LFC, is highly soluble, so a suitable liquid electrolyte couldn’t be found. It might be impractical to look for a solvent that selectively dissolves lithium electrolyte salts, but not the cathode’s salts.

(2) The materials react with PEO based solid electrolytes under the attempted processing conditions. The conditions under which cells with PEO based solid electrolyte work are unfavorable for the architecture and conditions tested.

(3) The materials spontaneously react with sulfur based solid electrolytes.

5.1.4 *Summary of Chapter 4 - ASSBs with Li_3YCl_6 Electrolyte and Li_2FeCl_4 Cathodes*

In chapter 4 cells with LFC cathode materials and a relatively new SE, LYC, were assembled and tested. Some key highlights included:

(1) LYC is a new promising SE in the halide family. Its ionic conductivity increases with an increase in its lattice parameters.

(2) LFC was electrochemically characterized for the first time, and is not only a viable, but highly promising material as cathode for ASSBs. It can be synthesized through cheap, high volume, low energy methods and still have a high degree of crystallinity.

(3) It is imperative to judiciously match the SE to the cathode used to prevent having to engineer their interfaces.

5.2 OUTLOOK

While ASSBs could significantly improve the safety, energy density, and cycle life of lithium batteries, there are several hurdles this technology needs to clear before becoming prevalent. As far as outlooks for the topics of interest discussed in this work, some interesting directions of research would be:

(1) Developing computational models to:
  a. Determine which factors need to be considered when matching SEs to cathode materials.
  b. Determine which factors need to be considered when engineering interphases between cathodes and solid electrolytes with differing chemical potentials.
  c. Determine the best design parameters for ASSBs, given the materials chosen.

(2) Studying the electrochemical properties of the Li_2MCl_4 family of materials. A lot of electrochemical properties of the iron containing variant remain to be studied. While the reasons for beginning with the iron containing material were outlined in chapters 3 and 4, it is entirely possible that a different variant has more appealing electrochemical properties.

(3) Exploring the Li_3MCl_6 family of materials for more suitable SEs. While the variant with M = Y material has excellent electrochemical properties, other materials from the same family could surpass those properties. Li_3InCl_6, for example, is presumably more stable as it has lower E_{hull};[42] it also has higher ionic conductivity[90].

BIBLIOGRAPHY

[1] C. Wang, J. Hong, Electrochem. Solid-State Lett. 10 (2007) A69.

[2] M.S. Whittingham, Chem. Rev. 104 (2004) 4271-4302.

[3] T. Asano, A. Sakai, S. Ouchi, M. Sakaida, A. Miyazaki, S. Hasegawa, Advanced Materials. 30 (2018) n/a.

[4] J.B. Goodenough, Y. Kim, Chemistry of Materials. 22 (2010) 587-603.

[5] V. Etacheri, R. Marom, R. Elazari, G. Salitra, D. Aurbach, Energy Environ. Sci. 4 (2011) 3243-3262.

[6] Heriot-Watt University, Centre for Economics Energy Research and Policy. (2018).

[7] U.S. Energy Information Administration, Office of Energy Statistics. (2019).

[8] N. Kamaya, K. Homma, Y. Yamakawa, M. Hirayama, R. Kanno, M. Yonemura, T. Kamiyama, Y. Kato, S. Hama, K. Kawamoto, A. Mitsui, Nature materials. 10 (2011) 682.

[9] , High Energy Density Lithium Batteries: Materials, Engineering, Applications, WILEY-VCH Verlag GmbH & Co., 2011.

[10] , Lithium batteries : advanced technologies and applications, Wiley-Blackwell, Chichester, 2013.

[11] , Principles and Applications of Lithium Secondary Batteries
, Wiley-VCH, Hoboken, 2012.

[12] , Lithium Batteries and other Electrochemical Storage Systems, Wiley-ISTE, London, 2013.

[13] Bobby. What is Overpotential in Battery? 2014; Available at: https://www.upsbatterycenter.com/blog/overpotential-battery/. Accessed Apr 22, 2019.

[14] J. Vetter, P. Novak, M.R. Wagner, C. Veit, K. Möller, J. Besenhard, M. Winter, M. Wohlfahrt-Mehrens, C. Vogler, A. Hammouce, Journal of power sources. 147 (2005) 269-281.

[15] H. Wang, Y. Yang, Y. Liang, J.T. Robinson, Y. Li, A. Jackson, Y. Cui, H. Dai, Nano Lett. 11 (2011) 2644-2647.

[16] Y. Kato, S. Hori, T. Saito, K. Suzuki, M. Hirayama, A. Mitsui, M. Yonemura, H. Iba, R. Kanno, Nature Energy. 1 (2016) 16030.

[17] S.P. Ong, Y. Mo, W.D. Richards, L. Miara, H.S. Lee, G. Ceder, Energy Environ. Sci. 6 (2013) 148-156.

[18] P. Bron, S. Johansson, K. Zick, Schmedt auf der Günne, Jörn, S. Dehnen, B. Roling, Journal of the American Chemical Society. 135 (2013) 15694-15697.

[19] P. Bron, S. Dehnen, B. Roling, Journal of Power Sources. 329 (2016) 530-535.

[20] A. Kuhn, O. Gerbig, C. Zhu, F. Falkenberga, J. Maier, B.V. Lotsch, (2014).

[21] Tokyo Institute of Technology. Solid electrolytes open doors to solid-state batteries. 2016; Available at: https://phys.org/news/2016-03-solid-electrolytes-doors-solid-state-batteries.html. Accessed Mar 20, 2019.

[22] J.H. Woo, J. Trevey, A. Cavanagh, Y.S. Choi, S.C. Kim, S. George, K.H. Oh, S. Lee, Journal of the Electrochemical Society. 159 (2012) A1124.

[23] B. Wu, S. Wang, W.J. Evans IV, D.Z. Deng, J. Yang, J. Xiao, Journal of Materials Chemistry A. 4 (2016) 15266-1528.

[24] K. Takada, Acta Materialia. 61 (2013) 759-770.

[25] H. Yamada, Y. Oga, I. Saruwatari, I. Moriguchi, Journal of The Electrochemical Society. 159 (2012) A385.

[26] N. Ohta, K. Takada, L. Zhang, R. Ma, M. Osada, T. Sasaki, Advanced Materials. 18 (2006) 2226-2229.

[27] A. Sakuda, A. Hayashi, M. Tatsumisago, Chemistry of Materials. 22 (2010) 599.

[28] A. Sakuda, H. Kitaura, Hayashi, Akitoshi, K. Tadanaga, M. Tatsumisago, Journal of the Electrochemical Society. 156 (2009) A32.

[29] K. Takada, N. Ohta, L. Zhang, K. Fukuda, I. Sakaguchi, R. Ma, M. Osada, T. Sasaki, Solid State Ionics. 179 (2008) 1333-1337.

[30] Y. Zhu, X. He, Y. Mo, Journal of materials chemistry. A, Materials for energy and sustainability. 4 (2016) 3253-3266.

[31] J. Haruyama, K. Sodeyama, L. Han, K. Takada, Y. Tateyama, Chemistry of Materials. 26 (2014) 4248-4255.

[32] Z. Chen, Y. Qin, K. Amine, Y.-. Sun, Journal of Materials Chemistry. 20 (2010) 7606.

[33] Y. Iriyama, H. Kurita, I. Yamada, T. Abe, Z. Ogumi, Journal of Power Sources. 137 (2004) 111-116.

[34] Y. Huang, J. Chen, J. Ni, H. Zhou, X. Zhang, Journal of Power Sources. 188 (2009) 538-545.

[35] Y. Huang, J. Chen, F. Cheng, W. Wan, W. Liu, H. Zhou, X. Zhang, Journal of Power Sources. 195 (2010) 8267-8274.

[36] J. Shim, K. Lee, A. Missyul, J. Lee, B. Linn, E.C. Lee, S. Lee, Chemistry of Materials. 27 (2015) 3273-3279.

[37] S. Chen, D. Xie, G. Liu, J.P. Mwizerwa, Q. Zhang, Y. Zhao, X. Xu, X. Yao, Energy Storage Materials. 14 (2018) 58-74.

[38] N. Ohta, K. Takada, I. Sakaguchi, L. Zhang, R. Ma, K. Fukuda, M. Osada, T. Sasaki, Electrochemistry Communications. 9 (2007) 1486-1490.

[39] B. Ahmed, C. Xia, H.N. Alshareef, Nano Today. 11 (2016) 250-271.

[40] Gaines JR. Kurt J. Lesker Company | Challenges for Non-Ideal Atomic Layer Deposition Processes & Systems — Blog | Vacuum Science Is Our Business. 2016; Available at: https://www.lesker.com/newweb/blog/post.cfm/challenges-for-non-ideal-atomic-layer-deposition-processes-systems.

[41] K. Takada, N. Aotani, K. Iwamoto, S. Kondo, Solid State Ionics. 86 (1996) 877-882.

[42] A. Jain, S.P. Ong, G. Hautier, W. Chen, W.D. Richards, S. Dacek, S. Cholia, D. Gunter, D. Skinner, G. Ceder, K.A. Persson, APL Materials. 1 (2013) 11.

[43] A. Kuhn, O. Gerbig, C. Zhu, F. Falkenberg, J. Maier, B.V. Lotsch, Phys. Chem. Chem. Phys. 16 (2014) 14669-14674.

[44] W.C. West, J.F. Whitacre, J.R. Lim, Journal of Power Sources. 126 (2004) 134-138.

[45] I. Tarhouchi, V. Viallet, P. Vinatier, M. Menetrier, Solid State Ionics. 296 (2016) 18.

[46] S. Hori, K. Suzuki, M. Hirayama, Y. Kato, T. Saito, M. Yonemura, R. Kanno, Faraday discussions. 176 (2015) 83-94.

[47] S. Kang, W. Yoon, K. Nam, X. Yang, D. Abraham, J Mater Sci. 43 (2008) 4701-4706.

[48] A. Sakuda, H. Kitaura, A. Hayashi, K. Tadanaga, M. Tatsumisago, Journal of Power Sources. 189 (2009) 527-530.

[49] A. Sakuda, A. Hayashi, M. Tatsumisago, Journal of Power Sources. 195 (2010) 599-603.

[50] A. Sakuda, A. Hayashi, T. Ohtomo, S. Hama, M. Tatsumisago, Journal of Power Sources. 196 (2011) 6735-6741.

[51] A. Sakuda, N. Nakamoto, H. Kitaura, A. Hayashi, K. Tadanaga, M. Tatsumisago, Journal of Materials Chemistry. 22 (2012) 15247.

[52] X. Chen, B. Chen, S. Chen, Z. Huang, Y. Zhao, Q. Xu, X. Xu, P. Long, Electrochimica Acta. 210 (2016) 905-914.

[53] Jing Li, Laura E. Downie, Lin Ma, Wenda Qiu, J. R. Dahn, ECS. 162 (2015) A1408.

[54] S. Ogawa, T. Teranishi, Physics Letters A. 36 (1971) 407-408.

[55] S.S. Hegde, A.G. Kunjomana, K.A. Chandrasekharan, K. Ramesh, M. Prashantha, Physica B: Physics of Condensed Matter. 406 (2011) 1143-1148.

[56] S. Liu, X. Chen, J. Zhao, J. Su, C. Zhang, T. Huang, J. Wu, A. Yu, Journal of Power Sources. 374 (2018) 149-157.

[57] R. Kanno, Y. Takeda, O. Yamamoto, Solid State Ionics. 28 (1988) 1276-1281.

[58] R. Kanno, Y. Takeda, K. Takada, O. Yamamoto, Solid State Ionics. 9 (1983) 153-156.

[59] A. Kajiyama, K. Takada, T. Inada, M. Kouguchi, S. Kondo, M. Watanabe, M. Tabuchi, Solid State Ionics. 152 (2002) 295-302.

[60] A. Jaiswal, C.R. Horne, O. Chang, W. Zhang, W. Kong, E. Wang, T. Chern, M.M. Doeff, Journal of the Electrochemical Society. 156 (2009).

[61] P.N. Kumta, D. Gallet, A. Waghray, G.E. Blomgren, M.P. Setter, Journal of Power Sources. 72 (1998) 91-98.

[62] R. Kanno, Y. Takeda, A. Takahashi, O. Yamamoto, R. Suyama, S. Kume, Journal of Solid State Chemistry. 72 (1988) 363-375.

[63] R. Kanno, Y. Takeda, A. Matsumoto, O. Yamamoto, R. Suyama, S. Kume, Journal of Solid State Chemistry. 75 (1988) 41-51.

[64] U.S. Department of the Interior, U.S. Geological Survey. USGS Minerals Information: Commodity Statistics and Information
. 2019; .

[65] H.D. Lutz, W. Schmidt, H. Haeuseler, Journal of Physics and Chemistry of Solids. 42 (1981) 287-289.

[66] R. Kanno, Y. Takeda, O. Yamamoto, Materials Research Bulletin. 16 (1981) 999-1005.

[67] J.L. Soubeyroux, C. Cros, W. Gang, R. Kanno, M. Pouchard, Solid State Ionics. 15 (1985) 293-300.

[68] R. Kanno, Y. Takeda, A. Takahashi, O. Yamamoto, R. Suyama, S. Kume, Journal of Solid State Chemistry. 71 (1987) 196-204.

[69] K. Takada, T. Inada, A. Kajiyama, M. Kouguchi, S. Kondo, M. Watanabe, Journal of Power Sources. 97 (2001) 762-764.

[70] J. Janek, W.G. Zeier, Nature Energy. 1 (2016).

[71] N. Nitta, F. Wu, J.T. Lee, G. Yushin, Materials Today. 18 (2015) 252-264.

[72] K. Kerman, A. Luntz, V. Viswanathan, Y. Chiang, Z. Chen, Journal of The Electrochemical Society. 164 (2017) A1744.

[73] K. Takada, T. Inada, A. Kajiyama, M. Kouguchi, S. Kondo, M. Watanabe, Journal of Power Sources. 97 (2001) 762-764.

[74] S. Wang, M. Yan, Y. Li, C. Vinado, J. Yang, Journal of Power Sources. 393 (2018) 75-82.

[75] Y. Haven, Recueil des Travaux Chimiques des Pays-Bas. 69 (1950) 1471-1489.

[76] E. Torun, H. Sahin, S.K. Singh, F.M. Peeters, Applied Physics Letters. 106 (2015) 192404.

[77] J.P. Perdew, K. Burke, M. Ernzerhof, Phys. Rev. Lett. 77 (1996) 3865-3868.

[78] G. Kresse, D. Joubert, Phys. Rev. B. 59 (1999) 1758-1775.

[79] P.E. Blöchl, Phys. Rev. B. 50 (1994) 17953-17979.

[80] G. Kresse, J. Hafner, Phys. Rev. B. 47 (1993) 558-561.

[81] G. Kresse, J. Furthmüller, Phys. Rev. B. 54 (1996) 11169-11186.

[82] H.J. Monkhorst, J.D. Pack, Phys. Rev. B. 13 (1976) 5188-5192.

[83] S.P. Ong, W.D. Richards, A. Jain, G. Hautier, M. Kocher, S. Cholia, D. Gunter, V.L. Chevrier, K.A. Persson, G. Ceder, Computational Materials Science. 68 (2013) 314-319.

[84] S.P. Ong, S. Cholia, A. Jain, M. Brafman, D. Gunter, G. Ceder, K.A. Persson, Computational Materials Science. 97 (2014) 209-215.

[85] A. Bohnsack, F. Stenzel, A. Zajonc, G. Balzer, M. Wickleder, G. Meyer, 623 (1997) 1067-1073.

[86] W.G. Zeier, S. Zhou, B. Lopez-Bermudez, K. Page, B.C. Melot, ACS Applied Materials & Interfaces. 6 (2014) 10900-10907.

[87] C.J. van Loon, J. de Jong, Acta Crystallographica. B31 (1975) 2549.

[88] J.H. Woo, J.E. Trevey, A.S. Cavanagh, Y.S. Choi, S.C. Kim, S.M. George, K.H. Oh, S. Lee, Journal of The Electrochemical Society. 159 (2012) A1124.

[89] T. Yamada, S. Ito, R. Omoda, T. Watanabe, Y. Aihara, M. Agostini, U. Ulissi, J. Hassoun, B. Scrosati, Journal of The Electrochemical Society. 162 (2015) A651.

[90] H.-. Steiner, H.D. Lutz, Zeitschrift für anorganische und allgemeine Chemie. 613 (1992) 26-30.

VITA

Carolina Vinado got her bachelor's degree in 2012, from the University of North Texas in Materials Science and Engineering with honors. She secured an offer of joining Dr. Yang's research group prior to graduation. She mainly worked on several aspects of lithium ion batteries while pursuing her PhD from the University of Washington. She volunteered in outreach efforts to spark the curiosity of children in various aspects of materials science, as well as in events to empower women, and encourage girls to pursue interests in science and technology.